CHEMICAL REVIEWS

pubs.acs.org/CR

Review

# Patterning Wettability for Open-Surface Fluidic Manipulation: Fundamentals and Applications

Pallab Sinha Mahapatra, Ranjan Ganguly, Aritra Ghosh, Souvick Chatterjee, Sam Lowrey, Andrew D. Sommers, and Constantine M. Megaridis*

Cite This: *Chem. Rev.* 2022, 122, 16752−16801

Read Online

ACCESS | Metrics & More | Article Recommendations

**ABSTRACT:** Effective manipulation of liquids on open surfaces without external energy input is indispensable for the advancement of point-of-care diagnostic devices. Open-surface microfluidics has the potential to benefit health care, especially in the developing world. This review highlights the prospects for harnessing capillary forces on surface-microfluidic platforms, chiefly by inducing smooth gradients or sharp steps of wettability on substrates, to elicit passive liquid transport and higher-order fluidic manipulations without off-the-chip energy sources. A broad spectrum of the recent progress in the emerging field of passive surface microfluidics is highlighted, and its promise for developing facile, low-cost, easy-to-operate microfluidic devices is discussed in light of recent applications, not only in the domain of biomedical microfluidics but also in the general areas of energy and water conservation.

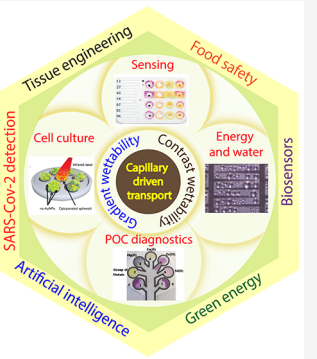


## CONTENTS



**Received:** January 14, 2022
**Published:** October 4, 2022







https://doi.org/10.1021/acs.chemrev.2c00045
*Chem. Rev.* 2022, 122, 16752−16801

## 1. INTRODUCTION

The field of microfluidics has advanced by leaps and bounds since the early 1990s, when Manz et al. first developed a miniaturized version of the total analytical system (TAS) with flow-through microfluidic channels.[1] Owing to their inherent high surface-to-volume ratio, such systems enable working with small quantities of fluid samples and reagents with high spatiotemporal resolution and short processing times at reduced footprint and improved cost. Such features make these systems highly suited for many biological, chemical, and medical applications.[2] Ensuring the appropriate flow of sample fluids and transport of reagents and analytes through these devices is a vital task that has traditionally been achieved by invoking several driving mechanisms,[3] such as capillarity, pressure gradient, electrokinetic means, centrifugal force,[4] acoustic mechanism,[5] or magnetic force.[6] Whitesides, in a seminal article about the future of microfluidics,[2] concluded that much of the world's technology requires the manipulation of fluids, and extending those manipulations to small volumes, with precise dynamic control over concentrations, while discovering and exploiting new phenomena occurring in fluids at the microscale level, must, ultimately, be very important. Since then,[7] a tremendous amount of research has been performed on engineering novel microfluidic and liquid-manipulation technologies. Despite these efforts, major pain points of conventional flow-through microfluidic platforms still exist, e.g., channel clogging by bubbles,[8] fouling by solid debris,[9] unwanted interaction of biological samples with channel walls, and nonspecific surface adsorption, that all need to be mitigated. Also, 3-D configurations of these devices require expensive and elaborate fabrication processes (lithography,[10] deep reactive-ion etching or DRIE,[11] micromachining,[12] etc.), which are both time-consuming and costly. Most conventional microfluidic systems are based on embedded or closed-channel configurations, where microchannels are fabricated in a rigid substrate (e.g., silicon, glass, PMMA, etc.)[13] or soft elastomers, like poly-(dimethylsiloxane), a.k.a. PDMS.[14] In most of these cases, liquids flow at low Reynolds numbers, eliciting purely diffusion-driven mixing, which is often inadequate for many biochemical protocols. Besides, there are operational difficulties because of reliance on several off-chip components required for liquid transport (i.e., pumps, actuators, energy source for pumps, etc.); such dependencies inhibit the possibility of using these devices at points of care with unskilled operators and at affordable cost. To fill this need, *surface microfluidics* has emerged as a promising liquid-handling platform and subgenre of microfluidics. Unlike conventional flow-through microfluidic devices, their open-surface counterparts are meant for transporting and manipulating liquid microvolumes on open substrates and not in a closed-channel configuration.

One important attribute of surface microfluidics is the wettability of the surface (the substrate), which implies the affinity of the surface toward a particular liquid (and the other way around). Interaction between the substrate and the liquid arises from polar and dispersive forces.[15,16] Depending on the surface energy and the roughness of the substrate as well as the surface tension of the liquid, the substrate may display affinity (hydrophilicity) or repellency (hydrophobicity) to the liquid. Surfaces may exhibit extreme wettability behaviors: complete spreading of the liquid occurs on superhydrophilic surfaces that have high surface energy and roughness features, whereas superhydrophobic surfaces exhibit extremely low adhesion and easy roll-off of liquid droplets dispensed on them.[17] Tuning of the surface wettability may be achieved through different surface modifications, including etching, deposition, coating, chemical functionalization, etc.[18]

Surface forces are predominant at small length scales, especially when solids interact with aqueous liquids (water has relatively high surface tension). Therefore, wettability plays an important role in microscale flows. This engenders a strong interrelationship between wettability and microfluidics (see Figure 1). Microfluidics and wettability are correlative and mutually reinforcing fields. Several attributes of open-surface and flow-through microfluidic flows can be harnessed for developing functionalized surfaces of desired wettability. For example, microfluidic maneuvering of droplets and bubbles can generate microenvironments for synthesis of composite micro- and nanoparticles of desired surface properties[19] and produce emulsions in a microfluidic environment,[20] which upon subsequent curing, can create porous materials and foams of tunable bulk and surface structures.[21] Microfluidic flows also lend to the development of novel materials with distinct surface properties, e.g., spinning of microfibers and nonwoven materials,[22,23] or leveraging microscale spray and film spreading to develop slippery liquid-infused porous (SLIP) surfaces.[24] Often, microfluidic approaches are employed to make interfacial-property measurements[25−27] and wettability tuning is adopted to gain insight into microfluidic-flow behavior.[28,29] For a comprehensive review on the role of microfluidics on the synthesis of functional surfaces and characterizing surface properties, the reader is referred to two excellent articles[30,31] and a book.[32] The present review article highlights the complementary attributes of the interrelationship between microfluidics and wettability, focusing on the origin of wettability induced flows on open-surface microfluidic platforms.

Manipulating small volumes of liquids on open surfaces offers several advantages over closed-channel systems; most of the common problems cited above for embedded microfluidic systems are dispelled by using surface microfluidic platforms, where the liquid is handled on a rigid or flexible,[33] porous,[34,35] or impervious substrate, or even on an immiscible liquid film.[36] Surface microfluidic flow takes place at a length scale comparable to or below the capillary length $\lambda_c = \sqrt{\gamma_{lg}/\rho g}$ of the liquid. At these scales, the surface tension of the liquid ($\gamma_{lg}$) can be harnessed as a dominating force for actuating passively (i.e., without any external energy input) liquid microvolumes. Recent material and process advancements across the academic community and industry on surface coatings[37] have facilitated control over liquid/surface interactions. Facile microfabrication techniques have been developed for surface microfluidic platforms, bringing down the time and cost requirements for developing rapid prototypes. A typical PDMS-based microfluidic device takes a minimum of one day[13] for fabrication, provided all the steps (designing mask, fabrication of mask template, curing PDMS) are performed in-house, which is not the norm in the majority of academic laboratories or points of need. On the contrary, a surface microfluidic device can be prototyped in less than 2 h, from design to final product.[33] This has stimulated renewed research interest in the microfluidics community toward exploring innovative and better lab-on-chip technologies, particularly for affordable healthcare solutions.[38]

To date, the most widely used technique of complex liquid manipulation on surfaces for lab-on-chip applications is


https://doi.org/10.1021/acs.chemrev.2c00045
Chem. Rev. 2022, 122, 16752−16801

electrowetting on dielectric (EWOD). EWOD is not a passive mode of transport, as it relies on off-chip components and external electric power. In an open-surface configuration, electrodes are patterned on primarily silicon wafers and covered with a dielectric and hydrophobic layer. Voltage (AC/DC) is applied to the electrodes from an off-chip source; this locally creates a surface tension gradient, thus generating a net unbalanced force responsible for manipulating aqueous droplets. A detailed account of EWOD is provided by Nelson and Kim.[39] EWOD, as well as other active modes of liquid manipulation on open surfaces, like opto-electrowetting (OEW),[40] magnetic[41,42] and acoustic[5] actuation, are beyond the scope of this review.

Surface tension-driven flow is a viable alternative of the aforementioned active transport strategies.[43] Generating liquid transport and controlled manipulation on surface microfluidic platforms without a pump or other on/off chip dependencies, has been a critical challenge for a host of point-of-care (POC) devices. The salient factors in this regard are (i) controlling the direction of liquid in quanta of moving droplets, and (ii) attaining the desired transport volume and speed (or volumetric flow rate) along the required transport distance. For achieving droplet directional transport, a surface with anisotropic wettability may be preferred. Attaining the desired fluid speed and distance warrants the generation of appropriate wettability contrast, with proper extent and gradient on the substrate. The droplet velocity is also affected by the fluid's viscosity, as well as any surface defects and acting gravity forces. To help balance these factors and to increase the overall droplet travel speed, appropriate strategies of capillary-driven transport must be explored. *Wettability patterning*, i.e., generating spatially varying surface wettability (in the form of discrete domains or in a continuous gradient), and/or creating spatial anisotropy in the liquid, either through thermal or chemical anisotropy, may be leveraged to create a net unbalanced capillary force, which can be used to actuate spontaneous droplet motion on a horizontal surface or even short distances uphill against gravity. The concept is based on altering the local surface energy at different parts of the surface, so that a net unbalanced surface-tension force ensues on any small liquid volume placed on the substrate. This net surface-tension force can be directed to move the droplet to a desired location on the surface for further processing or analysis. Additionally, one needs to pay attention to the repeatability in the fluid motion and durability of the surface. Does the droplet consistently travel to its target destination, and does it continue to do so reliably over time? This attribute is critical for lab-on-a-chip and sensor applications.

To influence the liquid/solid interactions and achieve controlled and passive liquid transport, several methods have been deployed, as discussed in the next section. A rapidly emerging and effective means of achieving this goal harnesses spatial domains of different wettabilities laid on a given solid surface. Engineering patterns of wettable and nonwettable regions on open surfaces, a process known as wettability patterning, offers promise in designing passive surface microfluidic devices, capable of not just transporting liquids without active power input, but also achieving complex fluidic tasks. Such surfaces comprise of juxtaposed regions of (super)-hydrophilic and (super)hydrophobic domains that are separated by wettability contrast lines. Liquids up to a critical volume, dispensed on the wettable domains, can be kept confined by the wettability transition lines; the liquid storage capacity of such wettability confined tracks depends on the track area, and the surface energy of the surrounding hydrophobic region.[44] By changing the shape (e.g., rectangular, triangular) of the hydrophilic domain, one can fabricate surface tension confined (STC) tracks[45] to transport liquid or even self-propel droplets,[33] thereby achieving passive transport, a phenomenon elaborated later in this review. Wettability gradients, texture gradients, as well as track-shape gradients are used in the literature to transport liquid passively on surfaces.

While the study and application of capillary-driven transport on surfaces featuring spatial wettability gradients is relatively new, most published studies have involved ideal surfaces, such as silicon, and most have been chemistry-based. A few papers have documented the application of spatially heterogeneous surface wettability, either in the form of smooth gradient or as sharp step contrast on metallic substrates.[46−48] Moreover, very few researchers have focused on the use of topographical modification alone (without the aid of chemical coatings) to create a surface-tension gradient capable of controlling droplet movement. It is important to note that chemical coatings tend to break down over time due to thermal cycling, abrasion, and environmental fouling.[49−53] Thus, the creation of microfluidic circuits based either in part or solely on topographical variation of the surface microscale roughness has significant appeal. Moreover, considering that capillary-driven surface microfluidics without active pumping requirement occupies a significantly lower chip footprint, this approach can be effectively deployed to build low-cost, disposable microfluidic devices. For such applications, the chemical attributes of surface-wettability tuning have to be durable enough only to survive their shelf life and deployment; for example, for single-use applications, long-term durability against sustained fluid transport is not a point of concern. This widens the opportunity of chemical functionalization as an additional tool for creating the desired wettability patterns.[54,55] Many different types of wettability engineering exist, including surface texturing through etching, deposition, or microfabrication, and chemical functionalization for attaining the desired degree of water affinity, liquid mobility, and specific bioanalytical attributes. Each wettability engineering strategy to achieve passive transport of liquid (primarily water) is discussed here in brief; however, the most common and arguably the easiest two types, viz., wedge-shaped wettability confined tracks and wettability gradients, are elaborated because of their sparse prior coverage in the literature.

This review is intended to draw attention from the wider microfluidics community to this aforementioned passive, liquid manipulation technique on solid surfaces. It summarizes the salient features of wettability patterning to achieve surface-tension-driven transport of liquid droplets and their complex manipulations (e.g., metering, merging, splitting, mixing, or even complex 3-D transport) on surface microfluidic platforms, without any elaborate off-chip integration. The purpose of this review is not to highlight problems associated with the existing microfluidic liquid-actuation techniques but to advocate the promises and evaluate the opportunities of harnessing capillary-driven passive liquid transport and manipulation for next-generation microfluidic devices that could benefit from this approach. The review is structured into four major sections: (1) capillarity and surface microfluidics, highlighting the major concepts and fundamentals, (2) passive liquid-transport mechanisms on open surfaces, (3) applications for lab-on-chip and beyond (e.g., energy and water conservation), and finally (4) challenges and future directions, identifying existing barriers


https://doi.org/10.1021/acs.chemrev.2c00045
Chem. Rev. 2022, 122, 16752−16801

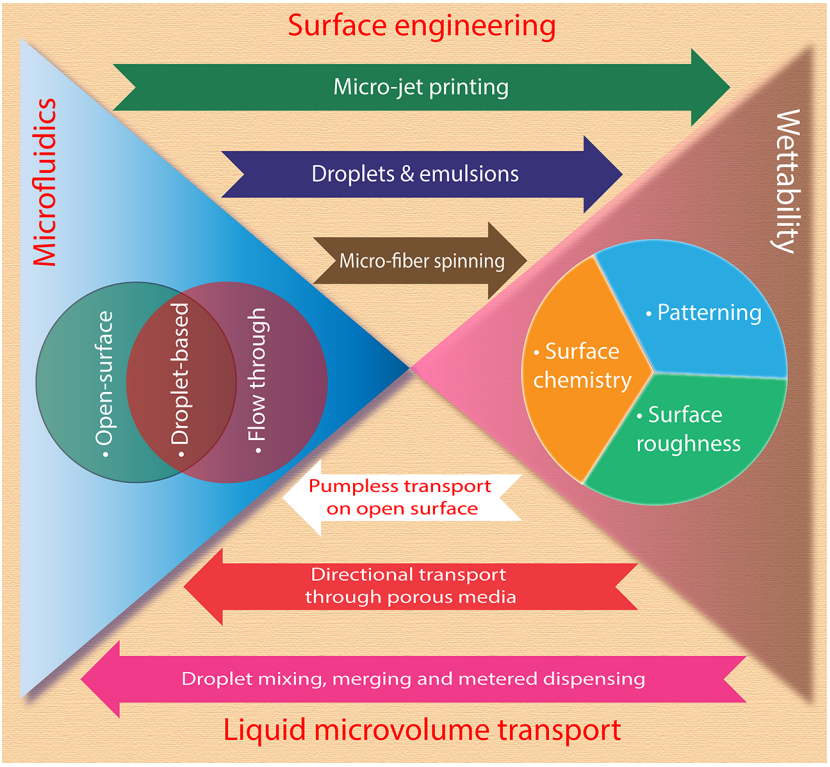


**Figure 1.** Mutual relationship between microfluidics (left quadrant) and wettability (right quadrant). For attributes of microfluidic flows offering a number of enabling technologies for surface engineering, see upper quadrant. The lower quadrant elucidates different modes of liquid microvolume transport realized by leveraging wettability engineering. The current review focuses primarily on the latter aspect.

and providing a possible roadmap to overcome the unresolved issues as well as exemplifying novel applications in this emerging field. The goal is to integrate such facile platforms to produce multifunctional microfluidic tools performing biological and chemical tasks toward the next-generation POC diagnostic devices and applications beyond lab-on-chip.

As such, this review focuses on flat surfaces or simple three-dimensional substrates that are modified topographically, or modified both topographically and chemically, to create surface tension gradients or discrete domains of contrast wettability to move liquids in miniscule quanta (in the range of nano- to microliter volumes) and flow rate (~microliters per second).

Figure 2 illustrates the salient domains of applications of capillary-driven liquid transport on surface-microfluidic platforms, which are reviewed in this article.

More specifically, in this review, we consider research articles where

- A droplet *is not* subjected to any external energy input, e.g., vibration, electrowetting, electrostatic or magnetic means, or even when such forces exist, they are not driving fluid transport. Papers describing dynamic control using external energy input are not reviewed.
- A droplet is deposited onto a surface at low momentum, implying a low Weber number ($We = \frac{\rho U^2 L}{\gamma} \ll 1$, where $U$ denotes droplet initial velocity, $L$ the characteristic dimension, and $\rho$ and $\gamma$ the liquid density and surface tension, respectively).
- The system is isothermal (except if indicated otherwise), and the majority of the work is concerned with water droplets deposited onto the patterned surface.

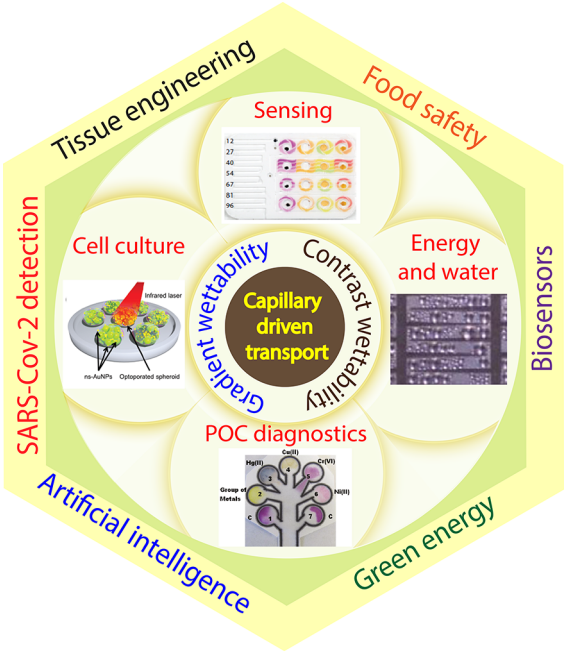


**Figure 2.** A few salient domains of open-surface microfluidic applications on wettability engineered surfaces.

- Only spontaneous motion is demonstrated; gravity-assisted flows are excluded unless they provide a novel insight into droplet kinematics on a surface featuring gradient or contrast wettability.



https://doi.org/10.1021/acs.chemrev.2c00045
Chem. Rev. 2022, 122, 16752−16801

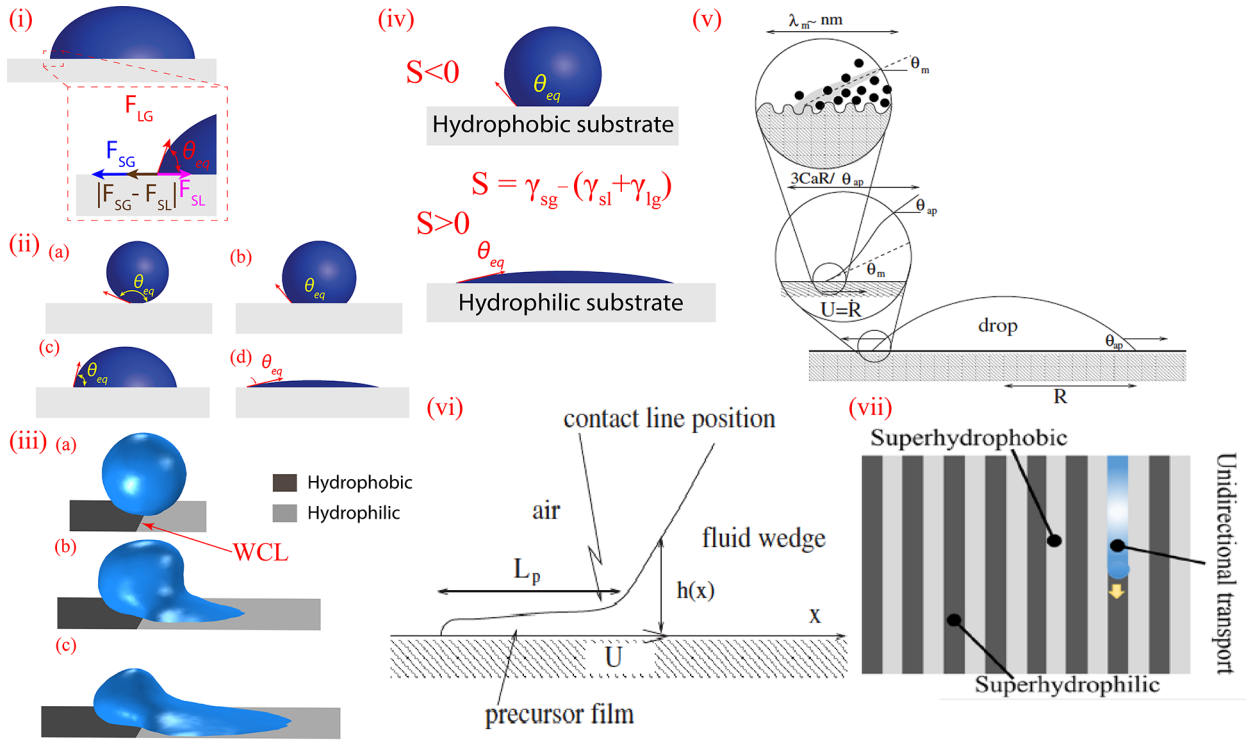


**Figure 3.** Basic concepts of wettability. (i) Contact angle and the origin of the Young−Laplace equation. (ii) Shape of liquid droplets on surfaces with different degrees of wettability: (a) superhydrophobic, (b) hydrophobic, (c) hydrophilic, and (d) superhydrophilic. (iii) Capillary-driven reshaping of a water droplet deposited at the wettability contrast line (WCL) between the hydrophobic and hydrophilic regions on a flat substrate. Representative simulation results are shown, where a droplet is deposited on a flat surface featuring a sharp wettability contrast line. (iv) Spreading criterion parameter $S$ for a liquid on a solid surface. (v) Depiction of the microscopic and macroscopic contact angles during liquid spreading; the microscopic contact angle $\theta_m$ ensues from surface-energy criteria, and accounting for local fluctuations, relates with $\theta_{eq}$; the apparent dynamic contact angle $\theta_{ap}$, also known as the advancing contact angle $\theta_A$ from macroscopic measurements, differs from $\theta_m$ because of the warping of the liquid meniscus from the competition between the surface tension and viscous forces. Adapted with permission from ref 57. Copyright 2009 American Physical Society. (vi) Schematic representation of the precursor film at the advancing liquid front. Adapted with permission from ref 57. Copyright 2009 American Physical Society. (vii) Directional transport of liquid (in blue) along 2-D superhydrophilic straight tracks surrounded on either side by superhydrophobic strips, which prevent the fluid from lateral spreading. The entire surface is placed horizontally, thus gravity is not a factor.

- Passive liquid transport is demonstrated experimentally; papers reporting exclusively theoretical or numerical modeling studies are excluded.

## 2. ORIGIN OF CAPILLARY-DRIVEN LIQUID TRANSPORT

As already pointed out, surfaces may have intrinsic or artificially imposed positive or negative affinity to the fluid based on the energetic interaction between the solid with the liquid. It is common practice to represent this interaction in terms of the equilibrium contact angle $\theta_{eq}$ of a sessile droplet deposited on a flat surface. The contact angle is measured between the tangent drawn along the liquid−air interface at the triple contact line (the intersection of solid, liquid, and gas phases) and the substrate toward the liquid phase (see Figure 3i). At equilibrium, the interfacial tension forces ($\gamma_{lg}$, $\gamma_{sl}$, and $\gamma_{sg}$, where $\gamma_{lg}$ is the surface tension of the liquid, and $\gamma_{sg}$ and $\gamma_{sl}$ are the solid/gas and solid/liquid interfacial energies) balance each other at the triple line to dictate the shape of the drop and, in turn, the equilibrium contact angle $\theta_{eq}$, which appears in Young's equation $\cos\theta_{eq} = (\gamma_{sg} - \gamma_{sl})/\gamma_{lg}$. Depending upon the affinity of the surface to water, the surface may be broadly classified as superhydrophobic ($\theta_{eq} > 150°$), hydrophobic ($90° < \theta_{eq} < 150°$), hydrophilic ($10° < \theta_{eq} < 90°$), and superhydrophilic ($\theta_{eq} < 10°$); see Figure 3ii.

While the equilibrium contact angle is representative of the wettability of a surface, it also provides valuable insight about the transport behavior of the droplet on this surface. A droplet on a surface of homogeneous wettability spreads (or resists spreading, if the material is not wettable) equally in all directions on the surface. On the contrary, on a surface that has spatially nonuniform wettability, directional preference may be observed for droplet transport. For example, a droplet deposited on a wettability contrast line (WCL: a line separating two semi-infinite domains with sharp wettability contrast) would experience a net unbalanced capillary force in the direction of the more wettable domain, thus undergoing directional transport; see Figure 3iii.

The simplest mechanism of capillary transport of a liquid on a solid surface is spreading. After a liquid droplet is placed on a surface, the condition for spreading (or not) is predicated by the spreading parameter $S = \gamma_{sg} - (\gamma_{sl} + \gamma_{lg})$.[56] The liquid spreads on the surface when $S$ is positive, while the fluid resists wetting the surface for negative $S$. The tendency of the liquid to wet or bead on a surface is attributed to the minimization of the system's surface energy. Figure 3iv shows a schematic of nonwetting (top, $S < 0$) and complete wetting (bottom, $S > 0$) of a droplet on a solid surface in gaseous surroundings. For homogeneous surfaces with $S > 0$, unrestrained spreading exhibits radial symmetry about the point of liquid deposition.

When a liquid droplet of radius $R_o$ and volume $\Omega$ is deposited on a smooth solid surface, where $S > 0$ (implying a high surface energy), the droplet spreads on the surface. Although simple in


https://doi.org/10.1021/acs.chemrev.2c00045
Chem. Rev. 2022, 122, 16752−16801

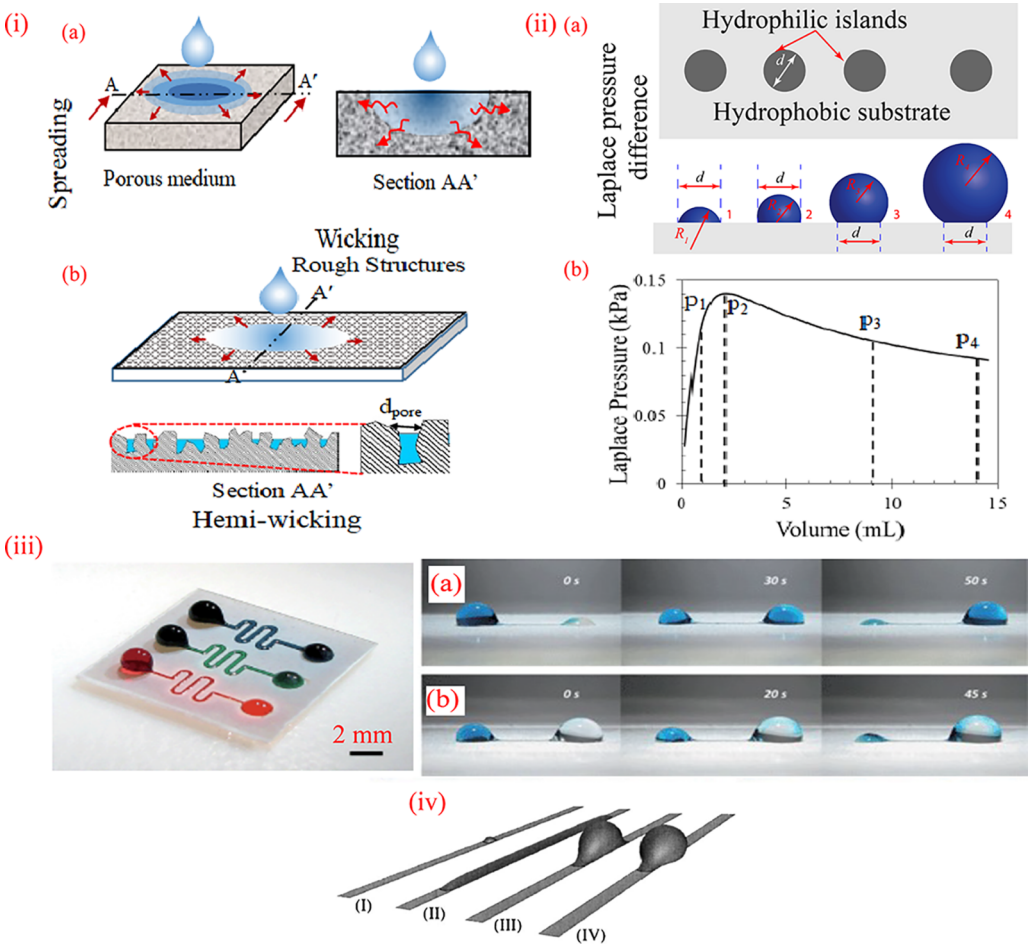


**Figure 4.** Liquid spreading and Laplace pressure basics: (i) Schematic showing spreading of a liquid droplet on a porous substrate (a, classical wicking) and a solid impermeable substrate with shallow micronano roughness structures (b, hemiwicking). For both cases, spreading distance varies with time as $x \sim t^{0.5}$. (ii) Tuning the curvature of a liquid droplet to vary its Laplace pressure. (a) Circular hydrophilic patches of diameter $d$, surrounded by a hydrophobic background confining liquid droplets of different volumes. The radius of curvature for each case is different, although the hydrophilic patch area is the same. This causes a variable Laplace pressure, which scales with the curvature of the droplet. (b) Representative plot showing how Laplace pressure changes with liquid volume placed on a hydrophilic disk of constant diameter, as depicted in (a). (iii) Young−Laplace pumping (from left to right) between wettability confined droplet pairs of different curvatures, which are connected by an open-surface wettable track, leading to liquid transport from the larger (volumewise) droplet to the smaller one (a), and from the smaller droplet to the larger (b). Adapted with permission from ref 68. Copyright 2011 The Royal Society of Chemistry. (iv) Liquid morphology on wettability confined straight rectangular tracks; for subcritical liquid volume per unit length of the track, semicylindrical liquid morphology is observed (I and II); local bulges appear (III and IV) when the liquid volume exceeds a critical value. Adapted with permission from ref 71. Copyright 2002 American Institute of Physics.

appearance, the phenomenon of spreading involves remarkable complexity. For droplet sizes below the capillary length $\lambda_c$ of the liquid, spreading of the droplet is influenced by the hydrodynamics of the liquid under a curved meniscus as well as the molecular interactions of the liquid with the solid. Therefore, the underlying theory should adequately describe the macro-, micro-, and nanoscale phenomena at play to predict the wetting behaviors relevant to microfluidic applications. Throughout the literature, the liquid/solid contact line equilibrium has been described in terms of Young's equation, but the multiscale feature of contact angle as described by Bonn et al.[57] is worth noting in this context; Figure 3v. Theoretically, the microscopic contact angle is determined purely by the surface energy balance at equilibrium. For a spreading droplet, the shape of the spreading edge of the liquid is represented by the advancing contact angle $\theta_A$. The interface near the advancing liquid front, where the driving surface tension and the opposing viscous forces contend, is highly curved and $\theta_A$ is larger than the equilibrium contact angle $\theta_{eq}$. A closer look at the spreading reveals that a thin precursor film of thickness of the order of a single molecular layer to several nanometers wets the solid ahead of the liquid bulk around the droplet footprint, which is followed by a radial spreading front of the liquid meniscus; see Figure 3vi. Intuitively, the spreading of the liquid precursor film is governed by the minimization of the total surface energy (of the solid−liquid system), and hence, is dependent on the value of $S$. On the other hand, the subsequent spreading of the droplet meniscus takes place primarily due to the Laplace pressure (arising out of the curvature of the droplet/gas interface) and gravity (for droplets larger than the capillary length $\lambda_c$ of the liquid, the finite height of the droplet lends a driving force aiding the spreading). This latter mode of spreading, therefore, does not depend on surface wettability, but rather on the hydrodynamic parameters (e.g., fluid viscosity, surface tension, and droplet volume). For a droplet dispensed gently on a flat surface, the liquid meniscus spreads radially at a pace that can be deduced through a balance between the available surface and gravitational potential energy and the viscous dissipation occurring near the contact line and


https://doi.org/10.1021/acs.chemrev.2c00045
Chem. Rev. 2022, 122, 16752−16801

the droplet bulk. For a simple Newtonian liquid of dynamic viscosity $\mu$, the temporal spread of the meniscus $R(t)$ and the spreading rate $\dot{R}(t)$ classically follow the relations deduced by Tanner[58] for small droplets (typically, for $R_o < \lambda_c$) and Lopez et al.[59] for large droplets (typically, for $R_o \geq \lambda_c$), as given by

$$R(t) = \Omega^{3/10}\left(\frac{\gamma_{lg} t}{\eta}\right)^{1/10} \; ; \; \dot{R}(t) \sim t^{-9/10}, \text{ for } R_o < \lambda_c, \tag{1}$$

and

$$R(t) = \Omega^{3/8}\left(\frac{\rho g t}{\eta}\right)^{1/8} \; ; \; \dot{R}(t) \sim t^{-7/8}, \text{ for } R_o \geq \lambda_c \tag{2}$$

Equation 1 is known as the Hoffman−de Gennes law. Brochard-Wyart et al.[60] and Redon et al.[61] showed that for the intermediate regime of droplet sizes (i.e., $\lambda_c \leq R_o < 10\ \lambda_c$) both capillary forces and gravity compete to drive the spreading, and the temporal spreading behavior deviates from the simple power law, yielding

$$R(t) = A(t - t_0)^{1/7.85}; \; \dot{R}(t) \sim t^{-6.85/7.85}, \quad \text{for } \lambda_c \leq R_o < 10\lambda_c \tag{3}$$

All expressions in eqs 1 −3 are predicated on the droplet spreading on a thin precursor film (already formed ahead of the spreading meniscus) on a *smooth* surface. Spreading on rough surfaces is found to differ, as reported first by Cazabat and Stuart;[62] for surface roughness features significantly smaller than the droplet diameter, the temporal variation of the spreading radius differs from eq 1−3 during a significant part of the spreading (except for the early and late phases) and follows a power law relation $R(t) \sim t^n$, with $n$ varying between 0.25 and 0.4. Microfluidic applications often involve flow of biological samples, which are mostly non-Newtonian in nature. Intuitively, the hydrodynamics of spreading of such fluids should differ from the classical Hoffman−de Gennes law. However, Rafaï et al.[63] reported that spreading behavior of a liquid having shear-dependent viscosity did not deviate strongly from Tanner's law (i.e., $n = 0.1$). For more details on spreading, the reader is referred to Bonn et al.[57] Fluid spreading may also be steered in a particular direction by guiding the liquid along a wettable (e.g., hydrophilic or superhydrophilic) track confined by nonwettable (e.g., hydrophobic or superhydrophobic) domains, as shown in Figure 3vii.

Capillary forces arise as the liquid/solid system attempts to attain minimum energy configuration. Such forces induce passive flow of the liquid and can be broadly classified as *wicking* or *hemiwicking* or *Laplace-pressure driven*. Wicking is observed in a porous substance made up of a hydrophilic material. Liquid imbibes through the pores of the substrate during wicking, thus minimizing the total surface energy of the system (Figure 4i(a)). When a textured wettable surface is exposed to a wetting liquid, a film propagates through the crevices of the surface features without fully immersing them (Figure 4i(b)). This phenomenon is known as *hemiwicking* and differs from classical wicking (where the liquid flows through capillary pores and not on the surface).[64] The propagating liquid front in both wicking and hemiwicking situations follows a $x \sim t^{0.5}$ power law, which ensues by a balance between the surface tension and the resisting viscous forces. Such spreading is more commonly known as Washburn spreading because it is governed by Washburn's law[65]

$$x(t) = \sqrt{\frac{\gamma_{lg} r_{pore} t \cos\theta_{eq}}{2\mu}} \tag{4}$$

where $x$ denotes the position of the liquid-spreading front, $t$ the duration of spreading from the onset, $r_{pore}$ the hydraulic radius of the pores, and $\mu$ the liquid viscosity. This model assumes uniform cylindrical pores, negligible gravitational effects, chemical homogeneity of the solid surface, and an unlimited reservoir volume (that supplies the spreading liquid).[66] It can be easily deduced from eq 4 that the velocity of a hemiwicking front declines with time ($\sim t^{-0.5}$). Several other spreading models have been proposed in the literature, taking into account the inertial, gravity, viscous and surface tension forces;[57] nevertheless, the fundamental trend of decreasing spreading velocity with time persists for all these models.

It is well-known that the curvature of a droplet imposes a pressure discontinuity across the curved interface; this pressure jump is more commonly known as the Laplace pressure and scales with the liquid surface tension $\gamma$ as well as the local interface curvature. For an implicitly defined surface $F(x,y,z)$ of a liquid, the curvature is related to the droplet surface geometry by $\kappa = \frac{\nabla F \mathrm{Hess}(F) \nabla F^T - |\nabla F|^2 \mathrm{Trace}(\mathrm{Hess}(F))}{2|\nabla F|^3}$, where $\mathrm{Hess}(F)$ represents the Hessian of the surface $F$.[67] For a spherical cap shape of the sessile droplet, the Laplace pressure difference $\Delta p$ across the curved surface is $\sim\gamma\kappa \sim 2\gamma_{lg}/R$. Figure 4ii(a) shows a schematic of various liquid volumes placed on hydrophilic patches of diameter $d$ and surrounded by a hydrophobic background. Such a wettable area surrounded by a nonwettable region on the surface is also referred to as a surface-energy trap (SET) as it confines liquid deposited on it by virtue of the surface energy difference between the wettable and nonwettable regions. The wettability confined droplets conform to different radii of curvature ($R_{1,2,3,4}$), depending upon the liquid volumes and the patch diameter. The plot in Figure 4ii(b) shows how the Laplace pressure inside these drops varies with the droplet volume, considering zero gravity, $d = 2$ mm and $\gamma_{lg} = 72$ mN/m (water). Clearly, the highest Laplace pressure corresponds to the case where the droplet radius of curvature $R$ is minimum (case 2, half sphere). Implementing this principle, when two liquid volumes of unequal curvature are connected by a wettable track on a substrate (Figure 4iii), liquid from the volume with the smaller radius (not necessarily the smaller volume) gets transported to the volume with larger radius by virtue of the Laplace pressure differential.[68,69] Typical volume flow rates attained with this Young−Laplace pumping mechanism is of ∼O(0.1 mL/h) and the time scales of transport are of ∼O(10 s).[68,70]

It is clear from the above discussion that capillary forces on wettability confined liquids can arise out of the curvature of the liquid. The shape of the liquid meniscus on a wettability confined region (e.g., a wettable area surrounded by a nonwetting background) of a substrate depends on the shape of the geometric wettability confinement and the wettability contrast between the two regions. In the simplest configuration of wettability confinement created on a rectangular, narrow strip of wettable region surrounded by a nonwettable background, the confined liquid takes a semicylindrical shape (Figure 4iv) as long as the dispensed liquid volume is small. However, the cylindrical shape gets disturbed and local bulges develop in the liquid strip[44,71] if the liquid volume $\Omega$ per unit length of the wettable track of width $\delta$ exceeds a critical value $\Omega/\delta^3$ (Figure 4iv). This critical value has been found to depend on the wettability contrast between the wettable track and the nonwetted


https://doi.org/10.1021/acs.chemrev.2c00045
Chem. Rev. 2022, 122, 16752−16801

background,[71] and the liquid bulge plays a pivotal role in generating Laplace pressure-driven flow on tapered wettable tracks of monotonically varying $\delta$ along the tracks.[33,72,73]

Laplace-pressure driven flow can also occur by artificially creating spatial nonhomogeneity of local surface energy of the sessile liquid, or the underlying solid substrate. Broadly classifying, there are two major techniques of tuning the Laplace pressure affecting the drop: (1) by inducing surface tension gradient in the liquid (Figure 5i), and (2) by inducing surface

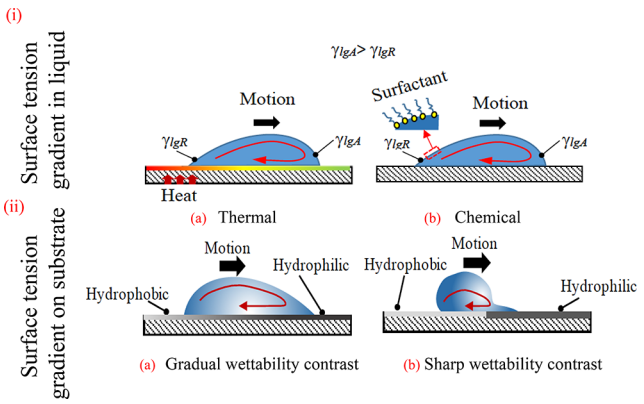


**Figure 5.** Passive liquid-transport mechanisms driven by surface-energy differentials: (i) Thermal (a) and chemical (b) surface tension gradients in the liquid promote fluid actuation. In (a), a temperature gradient on the substrate changes the local surface tension at the advancing (right) and receding (left) edge of the liquid volume. (b) Surfactants can alter local surface tension chemically, hence mobilizing the droplet by the differential capillary force between the advancing (right) and receding (left) front. $\gamma_{lgR}$ and $\gamma_{lgA}$ denote the liquid surface tension at the receding and advancing front, respectively. (ii) Droplet actuation by patterning the wettability of the substrate. (a) Substrate with spatially gradual wettability changes. The droplet moves from the hydrophobic (left) to the hydrophilic region (right). (b) Droplet actuation by a sharp wettability contrast line on the underlying solid. The property of the substrate suddenly shifts from hydrophobic to hydrophilic at the wettability contrast line. Note the distorted shape of the droplet at the onset of transport.

energy gradient on the substrate itself (Figure 5ii). In the former case, the liquid/gas surface tension is tuned by creating a chemical[74] or thermal[75] gradient along the interface, thus inducing Marangoni stresses. For the latter case, the local surface energy of the substrate is altered by creating a gradient of surface composition[76,77] or fabricating contrast wettability patterned tracks[33,45,78] of varied geometry.

One important factor toward realizing capillary-driven liquid transport on open surfaces is the feasibility and ease of rendering the desired wettability on the target regions of the substrate. The intrinsic wettability of a surface can be modified by altering the surface energy of the substrate, whether by applying different coatings or by treating with appropriate chemicals to modify the terminal groups present on the surface. Imparting micro- and nanoscale roughness features can also alter the surface wettability from its intrinsic value. Often, a practical means of wettability engineering leverages both these strategies in tandem to create extreme wettability contrasts or gradients. Details of surface fabrication strategies have already been extensively discussed in several excellent review articles,[79−82] and are therefore, kept out of the scope of the current review. Nonetheless, two broad surface modification techniques, viz., via chemical route and physical route, are discussed below for the sake of completeness.

As already pointed out, the wettability of a substrate depends on the chemical composition of the material. The terminal groups present on the substrate determine its surface energy, which in turn controls the surface wettability through the altered polar and dispersive components of its interaction with a liquid dispensed on it.[15,16] Functional groups on the surface can render the surface hydrophilic (e.g., hydroxyl, carbonate, per-oxy, etc.[82]), or hydrophobic (e.g., alkyl or per-fluoroalkyl silanes, etc.[81]). Wettability patterning is also possible by selectively modifying the surface functional groups. A brief (and nonexhaustive) account of salient chemical modification techniques is presented in Table 1.

Surfaces can also be engineered to have a specific wettability bias through physical modification, e.g., through altering surface roughness and microstructuring. These modifications lead to different wetting states—the Cassie−Baxter and Wenzel states[81] − of liquids when they come in contact with the surface. Patterned-wettability surfaces are realized through heterogeneous physical modification of the surface. A few standard fabrication techniques are summarized in Table 2.

In summary, significant progress has been made in the area of wettability engineering over the past 30 years. One of the largest advances has been in the area of nanofabrication and micromanufacturing, as well as in surface characterization, which has spurred even greater possibilities in terms of developing sharp contrasts and gradients of surface wettability on a large variety of surfaces (see Table 3). While the costs of developing these surfaces and durability in different microfluidic environments (e.g., in the presence of analytes, surfactants, contaminants and ions in the liquid sample) remain unclear, the methods outlined in Table 3 have opened up the possibility for tailoring the wettability gradient to specific droplet sizes and in many cases, faster droplet travel speeds (>60 mm/s) and long overall migration distances (> ∼10 mm). Table 4 summarizes the outcome of wettability engineering in terms of liquid transport features, like droplet speed and travel distance.

The subsequent sections elaborate on how such approaches can be deployed to achieve passive transport of liquids on open-surface microfluidic platforms.

## 3. PASSIVE LIQUID-TRANSPORT MECHANISMS

This section highlights some major mechanisms of passive liquid-transport strategies devised and reported by various research groups. It first unravels the mechanisms of capillary-driven passive liquid transport on different surfaces. An account of recent advancements in passive liquid transport techniques on various types of surfaces is provided in the next subsection, with the subsequent two subsections discussing the attributes of complex liquid manipulation tasks achieved through passive surface microfluidics. Alongside, a brief outline of the salient surface fabrication strategies to realize each type of transport is provided. Each transport type is also put in the context of the respective state-of-art by highlighting the current limitations in terms of characterization and the future research opportunities it creates.

### 3.1. Modes of Passive Liquid Transport

**3.1.1. Wicking.** The earliest elements of passive surface microfluidics were demonstrated by the Whitesides group and relied on the wicking properties of paper. Although wicking in paper and fibrous assemblies (e.g., fabrics) has been explored for


https://doi.org/10.1021/acs.chemrev.2c00045
Chem. Rev. 2022, 122, 16752−16801

**Table 1. Chemical Modification Approaches for Altering Solid-Surface Wettability**

| summary | advantages/limitations |
|---|---|
| **UV Irradiation** | |
| • requires photocatalyst-functionalized surface (e.g., $TiO_2$, ZnO)[34] | • high-resolution (~1 $\mu$m) patterned wettability achievable using collimated UV light[83] |
| • can enhance the hydrophilicity of the surface[84] | • scalable fabrication |
| • wettability patterning can be achieved through selective irradiation using photomasks[34] | • wettability change may often be reversed in the dark or high temperature[85] or prolonged storage in air[86] |
| **Plasma Treatment** | |
| • surface gets oxidized and becomes (super)hydrophilic[87] | • method is scalable and can be used on a wide range of surfaces |
| | • durability of the wettability modified surfaces is an issue[88] |
| | • challenging to create patterned wettable surfaces, as the mask requires openings for the plasma to penetrate[81] |
| **Molecular Grafting** | |
| • imparts functional groups onto the surface[89] | • surface can be easily functionalized when it contains carboxyl (−COOH) or hydroxyl (−OH) groups; otherwise, pretreatments are required |
| • specific functional groups can be grafted on a surface to alter the wettability | |
| • chemical vapor deposition, liquid deposition, and microcontact printing are example methods of molecular grafting | • patterned wettability by using a mask or laser ablation[33] |
| **Printing** | |
| • various materials can be printed on the substrate, for example, ink, polymers, wax, etc.[90] | • process is scalable |
| | • resolution is usually down to the microscale |
| | • printing on hydrophobic materials is challenging |
| | • precise wettability patterning is challenging |
| **Spray Coating** | |
| • spraying hydrophobic materials is a facile and scalable technique for creating hydrophobic surfaces; for example, spray-coating of anatase−polymer nanocomposite on paper, glass, metal of fibrous surface[33,34] | • process is scalable |
| | • patterned wettability can be achieved by spraying materials that can be functionalized; for example, anatase $TiO_2$-coated superhydrophobic surface can be patterned using UV radiation and photomasking[34] |

**Table 2. Physical Modification Approaches for Altering Solid-Surface Wettability**

| Summary | Advantages/Limitations |
|---|---|
| **Chemical Etching** | |
| • possible to create roughness on the surface by using strong acid or base[33] | • process is scalable |
| • transforms the hydrophilic surface (like metals) into superhydrophilic surface[78] | • prepared roughness features are hierarchical |
| • may be followed up by surface-grafting of hydrophobizing chemicals (e.g., silanes) to render the surface superhydrophobic[91] | • wettability patterning is possible using protective masks[33] |
| **3D Printing** | |
| • creates 3D structures on different materials by solidifying polymers[90] or metals | • surface finish is an issue |
| • predefined structures can be achieved | • resolution is generally ~O(20 $\mu$m),[90] however, with dielectrophoresis-assisted (DEP) printing, finer resolution can be achieved[92] |
| • wettability can be controlled by properly choosing the printing materials | • wettability patterning can be achieved |
| **Reactive Ion Beam Etching** | |
| • creates structure on surfaces (say silicon wafer) covered with a photoresist[93] | • sophisticated and costly equipment is required, not scalable |
| • used for high-resolution design | • not versatile for any surface |
| | • wettability patterning can be achieved |
| **Laser Ablation** | |
| • High-power laser beam can ablate different materials to alter wettability | • process is scalable |
| • High-resolution design can be engraved by using femto- or picosecond lasers[95] | • method can be used for most materials, for example, on spin-coated graphene ink films on flexible polyethylene terephthalate[94] |
| • single-step, maskless laser etching on graphene-based surface to tune electrical conductivity, surface morphology, and surface wettability[96] | • by controlling the scanning speed and rate, wettability patterning can be achieved |
| | • heat affected zone (HAZ) is a known issue |
| **Electrodeposition** | |
| • electrophoretic deposition of nanoparticles leads to formation of hierarchical roughness structure, leading to altered wettability[97] | • low-temperature deposition possible |
| | • easy controllability of surface structure and wettability |
| • deposition on metallic[98] as well as nonmetallic substrates, like PET and fibers,[97] is possible | |
| **Electrospinning** | |
| • electric-field-induced generation and laying of continuous polymeric ultrafine fibers on target surface[99,100] | • large range of materials, including polymers, composites, carbon, metals, and their oxides can be electrospun |
| • desired wettability is achieved by leveraging the intrinsic wettability of the fibers and the roughness features of the fiber mat | • enhancing wettability tuning possible with postspinning treatment |

centuries, its application in surface microfluidics was not reported until 2007, when Martinez et al.[130] demonstrated the capability of wicking tracks on paper to transport liquids specifically for microfluidic applications. They reported the fabrication and operation of a paper-based microfluidic device that was capable of performing several lab-on-chip tasks. The treated paper unidirectionally wicked the liquid from a pseudoinfinite reservoir. The basic principle was to confine the liquid on paper (which is intrinsically hydrophilic) by selectively depositing hydrophobic wax on the surrounding areas


https://doi.org/10.1021/acs.chemrev.2c00045
Chem. Rev. 2022, 122, 16752−16801

## Table 3. Salient Fabrication Processes for Creating Surface Gradient Wettability

| ref | gradient type | substrate | fabrication process | coating |
|---|---|---|---|---|
| 101 | wedge array using electrowetting (EWOD), linear gradient | silicon | (A) fluoropolymer undercoat (Cytop) on silicon; (B) resist and photolithography; (C) sputtered $SiO_2$; (D) strip leaving wedge array | N/A |
| 102 | linear micropillars and coating | silicon (N-type) | (A) photolithography and DRIE for micropillars, the etch depth created pillars of height 40 $\mu$m; (B) overcoated with adhesion-promoting silane and then Teflon | silane and Teflon |
| 103 | patterned microgroove gradients with gradually varied roughness regions (linear and radial) | silicon | photolithography: ICP RIE etching and then overcoat | Teflon, Parylene C, or PPFC ($C_4F_8$) |
| 104 | radially converging | silicon | photolithography: dual SAMs and single SAM systems prepared | trichloro(1*H*,*H*,2*H*,2*H*-perfluorooctyl)silane |
| 105 | linear microgroove gradient; linear micropillar gradient; converging radial gradients; linear stripe gradients | silicon | (A) laser-etching method employed to fabricate gradient structures; (B) after laser-etching, silanization | fluoroalkylsilane |
| 106 | patterned microgroove gradients with gradually varied roughness regions (linear); coating on top | silicon | (A) photolithography; (B) inductively coupled plasma to partially etch silicon substrate without the protection of the photo resist; (C) after terminating the etching and removing residual PR, covered the textured surface with microstructures; (D) to enhance the hydrophobic wettability, either Teflon or PPFC was coated on the textured surface; (E) Teflon overcoat spin coated onto substrates followed by baking at 200 °C; PPFC polymer ($C_4F_8$) deposited using plasma-enhanced CVD | Teflon or PPFC |
| 107 | micropillars/continuous; fluoropolymer overcoat | silicon | (A) photolithography and etching; (B) fluoropolymer overcoat applied | N/A |
| 72 | biphilic wedge gradient | glass | (A) triangle alignment mark patterned with aluminum metal; (B) nanotextured surfaces prepared by phase separation of methyltrichlorosilane $CH_3SiCl_3$ (MTS); (C) nanotextures synthesized by immersing the glass substrate in anhydrous toluene with MTS solution under controlled environmental conditions | yes |
| 108 | microgroove stripe structure; SAM overcoat for a double gradient | silicon | (A) photolithography; (B) plasma etching; (C) vapor diffusion of DTS SAM; silane chosen as less stringent than other commonly used hydrophobic silanes with regards to water content in the solvent and ambient | decyltrichlorosilane (DTS) |
| 109 | hole-to-pillar density gradients; SAM overcoat | PDMS (or epoxy) | (A) a pixel mask was used to produce a gradient pattern on silicon; (B) pattern was transferred to PDMS (or epoxy); (C) silane overcoat | silane |
| 110 | induced wrinkled structure; aluminum overcoat | thick elastomer film | (A) thick films of a flowable silicone elastomer; (B) stretched elastomer test pieces to desired prestrain; (C) thermally evaporated aluminum | N/A |
| 111 | linear gradient (with folded pillars all pointing in one direction) | silicon | (A) thermally grown, 200 nm thermal oxide layer; (B) projection lithography used to generate a photomask and the system subsequently exposed to plasma RIE pattern transfer; (C) residual photoresist removed using oxygen plasma where thermal oxide acted as a protective layer to etching; (D) nanopillars produced using DRIE; (E) gold film applied to one side of the pillars by e-beam evaporation with substrate at certain angles; (F) cooling process of the gold-coated silicon pillars led to thermal bimetallic effect causing a deflection of the nanopillars; Deflection angles could be controlled from 2°−52° by adjusting the gold film thickness | N/A |
| 112 | striped gradient plus SAM coating | silicon | (A) photolithography; (B) silanization with PFDTS process; (C) remaining resist then removed leaving stripe gradient | 1*H*,1*H*,2*H*,2*H*-perfluorodecyltrichloro silane |
| 48 | linear microgrooves | copper | (A) laser-etching | N/A |
| 113 | microgrooves plus surface energy gradient parallel to grooves | silicon | (A) photolithography; (B) RIE etching; (C) CVD of octamethylcyclotetrasiloxane; (D) chemical gradient was produced by photodegradation of the hydrophobic layer using deep-UV irradiation | N/A |
| 73 | wedge-shaped biphilic gradient | aluminum | (A) aluminum foil used as photomask; (B) thermal deposition of 100 nm copper layer; (C) oxygen plasma etching made aluminum (and copper) more hydrophilic; (D) HDFT immersion for a SAM layer modified copper (not aluminum), making it more hydrophobic | heptadecafluoro-1-decanethiol |
| 114 | converging radial gradient; shape gradient with wedges pointed inward | silicon | (A) mask (of $SiO_2$) photolithography; (B) DRIE; (C) final fluoropolymer layer grown by PECVD | fluoropolymer |
| 115 | linear gradient | copper | electrodeposition of copper onto copper; found that nanoparticles and nanodendritic structures were created | 1-dodecanethiol |
| 116 | converging topographic radial gradient | silicon | (A) photolithography; (B) DRIE; (C) spin-coated polybutadiene (micropattern facilitated droplet transition from Wenzel to Cassie state during condensation) | plasma fluorinated polybutadiene film |



https://doi.org/10.1021/acs.chemrev.2c00045
Chem. Rev. 2022, 122, 16752−16801

**Table 3. continued**

| ref | gradient type | substrate | fabrication process | coating |
|---|---|---|---|---|
| 93 | pillar density gradient (non-uniform texture); linear gradient | silicon | fabricated on silicon wafer by photolithography and DRIE | N/A |
| 117 | micro mesh | stainless steel | (A) stainless steel mesh consecutively rinsed in ethanol and deionized water under ultrasonication for 5 min each to remove impurities; (B) the treated mesh was inserted into an aqueous solution of electrolyte ($CuNO_3{\cdot}6H_2O$, 0.05 M) and treated with cathodic electrodeposition by using a narrow-strip Cu foil as an anode, distance between cathode and anode was 0.5 cm; (C) due to different resistances between different areas on the mesh and the anode, a current gradient was formed during the electrodeposition process | N/A |
| 118 | microgrooves plus nanoroughness; linear, curved, and spiral gradients | silicon | (A) 2 $\mu$m thick $SiO_2$ film made on silicon; (B) photolithography to selectively cover photoresist on $SiO_2$ film; (C) RIE to etch the $SiO_2$ not protected by photoresist; (D) DRIE further etched the substrate, forming silicon nanopillars; (E) photoresist removed | N/A |
| 119 | linear gradient; circular gradient; spiral gradient | silicon | (A) photolithography followed by DRIE used to transfer side channels; (B) further thermal oxidation, photolithographic processing, and RIE to fabricate re-entrant structures | N/A |
| 120 | micro/nano hierarchical structure | AISI 304 stainless steel | (A) laser-etching with constant and variable speeds; (B) to reduce the surface energy, the samples were subsequently silanized using $C_{14}H_{19}F_{13}O_3Si$ with a concentration of 1% for 1 h, followed by washing with ethanol and drying in oven at 90 °C for 1 h | silane |
| 121 | microgrooves; radial (converging); coating | copper | (A) laser-etching; (B) sample was made hydrophobic by immersing the plate in a 0.1 M heptadecafluoro-1-decanethiol (HDFT) solution for 6 min followed by immersion in dichloromethane for 20 s, process resulted in a SAM on the copper, rendering it hydrophobic (even superhydrophobic) | heptadecafluoro-1-decanethiol |
| 122 | structure plus copper coating; micropillars; linear; pillars decrease in size | surface 1, silicon; surface 2, PDMS; surface 3, PDMS | surface was fabricated with microholed gradient structures; photolithography and inductively coupled plasma (ICP) etching technology used to create microhole gradient on a silicon wafer; the substrate was covered with a nanoscale copper film by sputtering technology | copper coating (applied to surface 1) |
| 123 | double-gradient of nanopillars and chemical gradient | silicon | (A) double-gradient wrinkled structure by spin-coating PDMS film on commercial silicon template with gradient hole arrays; (B) pattern transferred to prestretched VHB taped surface, then prestretched VHB tapes released; (C) surface treated with space-limited oxygen plasma | N/A |
| 124 | converging radial gradient | silicon | (A) mask preparation; (B) photolithography; (C) postbake for hardening to enhance the residual photoresist; (D) DRIE | N/A |
| 125 | microstructured dimples | $Si_3N_4$ ceramic | femtosecond laser used to make dimpled structures | N/A |
| 126 | radial micropillar structure; converging and diverging gradients made | silicon | photolithography: two micropillar surfaces and reference smooth surface of SU8 photoresist polymer fabricated on the same silicon wafer | N/A |
| 127 | microgrooves with hydrophobic tops and hydrophilic channels | silicon | (A) $SiO_2$ fabricated on silicon wafer via oxidation as hydrophilic surface; (B) hydrophobic coating applied using Cytop (Asahi Glass); (C) mask photolithography, pattern transfer; (D) dry-etching and photoresist removed | N/A |
| 128 | nanopillars with height gradient, inspired by pine-needles and cactus spines | | (A) 3D-printing method; (B) samples dipped in crystal seed solution 3× and dried at room temperature; (C) sample and mother liquor (etchant solution) placed into agitated reactors in an oven at 90 °C for 10 h; (D) surfaces treated with FAS-17 to decrease their surface energy | FAS-17 (applied to surface) |
| 129 | microlines (or microgrooves) | aluminum | (A) laser-etching; (B) nanoroughness from local boiling giving hierarchical structure | N/A |



https://doi.org/10.1021/acs.chemrev.2c00045
Chem. Rev. 2022, 122, 16752−16801

**Table 4. Summary of Gradient−Surface Outcomes**

| ref | travel distance | droplet speed |
|---|---|---|
| 101 | droplet moved ∼15 mm on the gradient; entire gradient length was traveled | on 10 mm-long gradient, velocity varied between ∼50 mm/s and ∼70 mm/s<br>For 15 mm gradient, speed was 20 mm/s to ∼160 mm/s. |
| 103 | 2.5 mm | 62.5 mm/s |
| 104 | approximately 0.9−2.0 mm | front edge, 72.5 mm/s |
| 106 | 2.5 mm in one case | mean velocity 62.5 mm/s obtained from photographs (at distance $\Delta x$ = 2.5 mm and interval $\Delta t$ = 0.04 s) |
| 107 | | with applied vibration, mean droplet velocity was 2.2 ± 0.2 cm/s |
| 72 | ∼9 mm | wide range of droplet volumes was transported, and droplet velocity as high as 0.5 m/s on wedge-shape gradient |
| 108 | travel distance ∼9 mm for 10 μL droplet | max velocity around 70 mm/s |
| 109 | no motion | no motion |
| 110 | | as droplet was vibrated, it moved rapidly down the wetting gradient<br>droplets (10 μL) moved with speeds in excess of 200 μm/s. |
| 111 | spreading of advancing edge ∼3.8 mm | speed of advancing edge ∼0.015 mm/s |
| 112 | in one case, the droplet center moved ∼3 mm | maximum velocity ∼14.6 mm/s |
| 48 | between 0.5 and 1.5 mm | |
| 113 | droplet traveled ∼8 mm | ∼7 mm/s |
| 73 | spreading mode, travel greater than 20 mm | |
| 114 | converging radial gradient<br>5 μL droplet traveled 2.5 mm toward center<br>effect of droplet size on self-mobility studied at different locations within the gradient region | (a) 1.5 μL droplet, dispensed within 1.5 mm of the center, average speed of 3.0 cm/s;<br>(b) 3.0 μL droplet, dispensed within 2.0 mm of the center, average speed of 4.0 cm/s;<br>(c) 4.0 μL droplet, dispensed within 2.5 mm of the center, average speed of 2.5 cm/s;<br>(d) 5.0 μL droplet, dispensed within 2.5 mm of the center, average speed of 2.5 cm/s. |
| 115 | 8 μL droplet traveled ∼11−12 mm | ∼18 mm/s for 8 μL droplet |
| 116 | around 6 mm travel for a 3 μL droplet | 22.5 mm/s |
| 93 | droplet impact only | no net lateral transport |
| 117 | 2.1 mm travel (receding edge) | travel velocity ∼2.1 mm/s (estimate). |
| 118 | maximum travel displacement: ∼37.5 mm; curved pathways demonstrated | Mean velocity of 75 mm/s for 5.2 mm displacement |
| 119 | greater than ∼20 mm; curved pathways demonstrated | as high as ∼80 mm/s |
| 120 | data not provided | droplet movement observed on 10° tilted samples |
| 121 | travel distances as large as 3.5−4.0 mm | typically ∼3−12 cm/s (calculated); instantaneous peak speeds greater than 10 cm/s calculated |
| 122 | no motion | no motion |
| 123 | spreading length of ∼5 mm observed. Increased to 10.7 mm for double-gradient wrinkled surface. | not found |
| 124 | travel of ∼3.85 mm | 4.8 cm/s in one case |
| 125 | spreading ∼9.6 mm | initial peak speed: ∼17.5 μm/ms (or 17.5 mm/s) for spreading length of 9.6 mm |
| 127 | receding edge estimated to travel 11.4 mm | not found |
| 128 | ∼1.2 mm in one case (estimate) | ∼10 cm/s |
| 129 | 1.75 ± 0.25 mm | not provided |

either by photolithographic technique or using a desk-jet printer. Their device conformed to the World Health Organization's ASSURED (Affordable, Sensitive, Specific, User-Friendly, Rapid and Robust, Equipment-Free, and Deliverable to end user) standard for diagnostic devices intended for developing countries. Paper-based microfluidic devices relying on wicking for transport can perform several low-cost biological and chemical diagnostics. The liquid transport is laminar and can be approximated by 1-D Washburn flow. The wicking mechanism, however, has a major limitation in terms of transport speeds. A simple scaling analysis using eq 4 indicates that, on a rough surface with average $r_{pore}$ ∼ 0.1−1 μm, a liquid droplet (e.g., water, μ ∼0.001 Pa s, $\gamma_{lg}$ = 72 mN/m) would take O(∼10−100s) to traverse a distance of O(∼1 cm) by hemiwicking. In most paper-based microfluidic devices, contrast wettability patterning has been used to confine the liquid and transport it by wicking in a specific direction. Besides paper, wicking-based passive transport was recently explored on woven fabrics as well.[131] On fabric-based wicking devices, threads of different wettability are interwoven to directionally transport the liquid. Wicking-based transport in paper has been the focus of several seminal reviews;[38,66,132] thus, the reader is referred to those for further details.

In the classical Lucas−Washburn (L−W) expression (eq 4), the liquid spreading (liquid rise or capillary rise for vertical spreading) is proportional to the square root of time. However, during experiments, it has been found that the height of the capillary rise decreases with time due to external factors like evaporation, swelling of the fibers, and gravity. Liu et al.[133] used an evaporation model proposed by Fries et al.[134] to estimate the capillary rise height as

$$h_{ev} = \frac{m_e}{\rho \epsilon_0 \delta W} = \sqrt{\frac{4\gamma_{lg}\cos(\theta)K_0 t}{\mu \epsilon_0 R_c}} - \frac{2m^*_{ev}}{\rho \epsilon_0 \delta}\int_0^t h_{ev}\, dt \quad (5)$$

where $\rho$, $\gamma_{lg}$, and $\mu$ are the liquid density, surface tension, and viscosity, respectively. Whereas, $\epsilon_0$, $K_0$, $R_c$, $\delta$, and $W$ are the initial porosity, permeability, capillary radius, thickness, and width of the paper strip, respectively. The static contact angle is $\theta$, and $t$ is time. The evaporation rate is calculated as

$$m^*_{ev} = (1 - \varphi)p_w \frac{0.089 + 0.0782V_a}{L_v} \quad (6)$$



https://doi.org/10.1021/acs.chemrev.2c00045
Chem. Rev. 2022, 122, 16752−16801

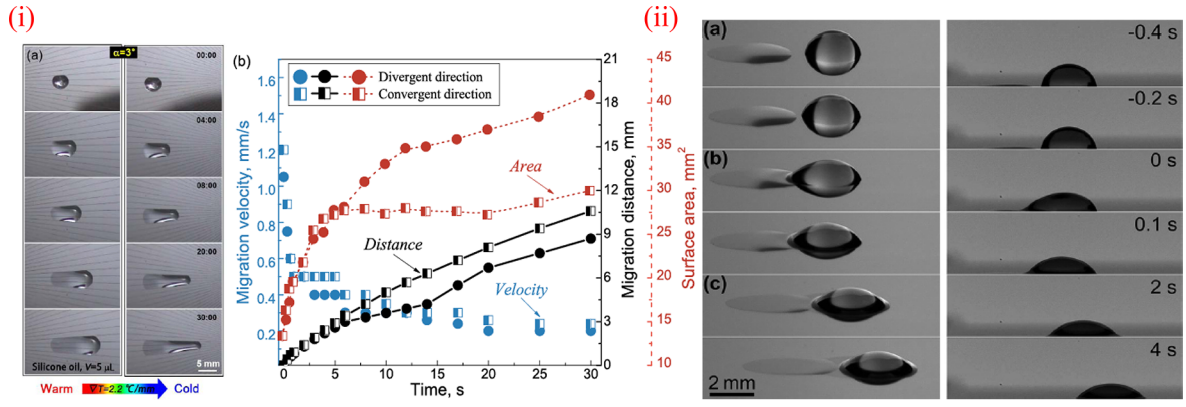


**Figure 6.** Passive droplet transport driven by liquid surface-tension gradients. (i) (a) Transport of silicon oil droplet by thermocapillary mechanisms. (b) Respective migration velocity, distance, and surface area of the droplet with time. Adapted with permission from ref 143. Copyright 2019 American Chemical Society. (ii) Droplet motion driven by combined thermocapillary and composition-induced Marangoni stresses. The left and right columns are from two independent experiments at viewing angles of 20° and 3°, respectively. Adapted with permission from ref 144. Copyright 2011 American Institute of Physics.

where $\varphi$, $p_w$, $V_a$, and $L_v$ are the relative humidity (RH), liquid saturation pressure, ambient flow velocity, and latent heat of vaporization, respectively. The solution of this equation was described in detail by Patari and Mahapatra[135] who also considered the effect of gravity during the capillary rise. During the wicking process, the fibers absorb the liquid and the fibers swell. Thus, the swelling process modifies the capillary radius, permeability, and porosity. Schuchardt and Berg[136] modified the classical L−W equation to incorporate the swelling effect. The modified expression for the capillary rise is given as

$$h_{sr} = \sqrt{\frac{\gamma_{lg} R_0 \cos(\theta)}{2\mu}\left(t - \frac{a}{R_0}t^2 + \frac{a^2}{3R_0^2}t^3\right)} \tag{7}$$

where $R_0$ denotes the preswell capillary radius and $a$ the swelling rate.

While the aforementioned theories of wicking have been used extensively in different applications, one should keep in mind their limitations. The classical Lucas−Washburn expression was developed for liquid flow through capillary tubes. Later, the capillary rise formulation was modified by incorporating the effects of evaporation (from the surface) and swelling (of the fibers).[137] However, all modifications were based on the basic assumptions for a capillary tube, with the fiber orientations in a porous substrate, e.g., fabric or paper, not being considered. Models capable of addressing time-dependent variation of porosity, permeability, and dynamic contact angle are lacking in the literature. Detailed fluid-flow analysis, considering nonwoven thin materials, is required for overcoming the design challenges of paper-based microfluidic devices.

**3.1.2. Transport Driven by Spatial Variation of Surface Energy.** As mentioned in the previous subsection, this transport mechanism relies on tuning the local surface energy gradient in the liquid (Figure 5i) or the substrate underneath the liquid (Figure 5ii); the latter may be achieved by varying the local wettability of the substrate, either gradually (gradient wettability) or sharply (step contrast wettability).

*3.1.2.1. Transport Due to Liquid Surface-Tension Gradient.* As described in Figure 5i, surface tension gradient in a sessile droplet can induce directional transport toward the higher local surface tension in the liquid. For a sessile droplet, the driving capillary forces arise due to the difference in the contact angles at the front ($\theta_f$) and the rear ($\theta_r$) ends of the droplet. The two angles differ because the difference in the surface tension of the liquid (due to thermal or chemical gradient on the liquid surface) induces a difference in the solid/gas ($\gamma_{sg}$) and the solid/liquid ($\gamma_{sl}$) interfacial tensions between the front and the rear of the droplet. For a circular or near-circular droplet footprint of radius $R$ on the surface, the driving capillary force may be expressed as[138]

$$\begin{aligned} F_{driving} &= 2R\int_0^{\pi/2} [(\gamma_{sg} - \gamma_{sl})_f - (\gamma_{sg} - \gamma_{sl})_r] \cos\varphi d\varphi \\ &= 2R\gamma_{lg}\int_0^{\pi/2} [\cos\theta_f - \cos\theta_r] \cos\varphi d\varphi \end{aligned} \tag{8}$$

where $\varphi$ denotes the polar angle measured on the droplet footprint from its center. The spatial gradient of surface tension on the liquid/gas interface can either arise due to local heterogeneity of chemical composition or temperature.[139] Cira et al.[74] observed that evaporation from a two-component, miscible, liquid mixture created spatial heterogeneity in liquid surface tension, thus leading to spontaneous liquid transport. When such droplets were deposited on glass, evaporation from one droplet altered the liquid-to-gas surface tension in the vicinity, thus affecting the mobility of a neighboring droplet. Diguet et al. demonstrated a novel chromocapillary effect, whereby selectively illuminating spots with light of different wavelengths, they moved 3 $\mu$L droplets floating on a water film with speed up to 300 $\mu$m/s.[140] The aqueous solution contained a surfactant that exhibited wavelength-dependent polarity upon illumination; by shining localized, bicolor concentric illumination, a chromocapillary trap developed, which moved the droplet as the illumination spot moved. Xiao et al.[141] demonstrated Marangoni flow driven by light-induced isothermal changes in interfacial tension to realize droplet transport at speeds up to 10.5 mm/s. They also demonstrated complex forms of transport of solvent droplets, like merging, using guided illumination. Akin to the chemical surface gradients, temperature gradients locally alter the surface tension from the leading to the trailing edges of the droplet, thus creating an unbalanced capillary force. For example, surface tension of water at 20 °C is ~72 mN/m, whereas at 90 °C it is ~60 mN/m. This property was explored by Darhuber et al.,[76] who fabricated a thermocapillary microfluidic droplet actuator, which relied on integrated microheater arrays to control the substrate temper-


https://doi.org/10.1021/acs.chemrev.2c00045
Chem. Rev. 2022, 122, 16752−16801

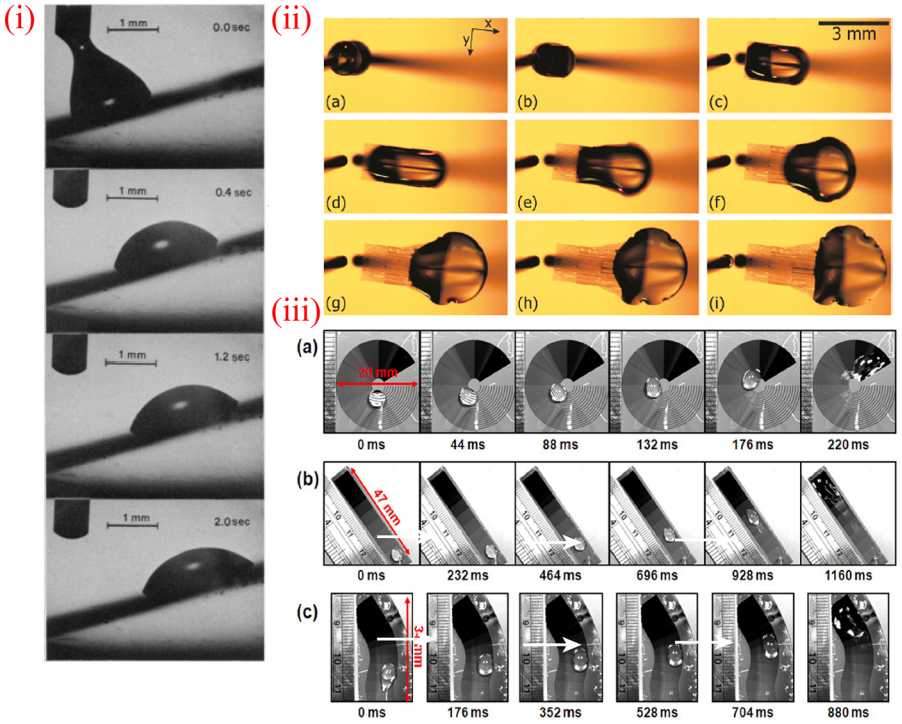


**Figure 7.** Liquid transport driven by underlying surface wettability gradient. (i) Uphill motion of a 1 $\mu$L drop dispensed on a surface-tension gradient surface inclined by 15° to the horizontal. Reproduced with permission from ref 77. Copyright 1992 American Association for the Advancement of Science. (ii) Motion of a 2 $\mu$L glycerol/water droplet on a surface pattern with varying fraction of hydrophilic-to-total area of the plate. Radius of dispensed droplet is 0.78 mm. Reproduced with permission from ref 112. Copyright 2011 American Chemical Society. (iii) For long-range and large-volume droplet transport, three types of gradient surfaces were created. (a) Droplet self-propulsion on annular path. (b) Droplet self-propulsion on straight path, (c) Droplet self-propulsion on "S" shape path. Reproduced with permission from ref 118. Copyright 2017 Springer Nature.

ature with high spatial resolution. They also used a similar concept of thermocapillary actuation to split a droplet from a film.[142] Dai et al.[143] showed the silicon oil motion due to the thermocapillary action on a horizontal substrate (see Figure 6i). Chakraborty et al.[75] exposed a chemical wettability gradient surface to elevated temperatures and reported that the droplet movement intensity increased with temperature differences on the substrate.

The combined effect of chemically induced Marangoni stresses with thermocapillarity was shown to propel droplets with velocities as high as ∼40 mm/s, which is significantly higher than the transport speed (∼1 mm/s) from thermocapillary action alone.[144] An example of droplet motion is shown in Figure 6ii. Chakraborty et al.[75] used significantly lower thermal gradients (0.08−0.20 °C/mm), which lowered the input energy requirement. Although this mechanism requires an active component (external energy supply), the ability to operate at low voltages makes this technique a convenient alternative for manipulating droplets. A combination of bicomponent droplet and thermocapillary actuation was explored by Zhao et al.,[144] who concluded that by encapsulating an aqueous droplet with a long-chain alcohol (heptanol in this case), one could thermally mobilize the droplet on a hydrophobic surface. By applying a thermal gradient to this two-component system, the alcohol evaporated at different rates at the front and the back of the droplet, creating a thermocapillary force, which eventually mobilized the droplet. Transport velocities were of ∼O(0.1 mm/s) for the binary droplet and transport distances were limited to ∼1 mm. Linke et al.[145] harnessed the Leidenfrost effect[146] on a heated rachet surface to self-propel droplets. This self-propelling effect was further studied by Lagubeau et al.,[147] who explained that the vapor escaping below the levitating Leidenfrost droplet provided a thrust due to the presence of asymmetric rachet-like structures. Droplet velocities of ∼O(10 cm/s) were reported. Although the above transport mechanism is passive, the capillary force is not dominant for this particular case. The viscous force exerted by the vapor flow between the droplet and the underlying rachet substrate induces the droplet movement.[145] A detailed discussion on thermocapillary migration and the Leidenfrost effects is beyond the scope of this review.

*3.1.2.2. Transport Due to Surface Wettability Gradient.* As depicted in Figure 5ii, a gradient in surface wettability develops a net unbalanced force on a sessile droplet, which causes the liquid to move toward the region of higher wettability.[138,148−150] Gradient wettability on the surface can be created either by inducing a smooth transition from nonwettable to wettable property or by deploying wettability steps of gradually varying extents well below the capillary length, thus creating a stepwise wettability variation for directional transport of droplets.

In a seminal study, Chaudhury and Whitesides[77] demonstrated how harnessing surface energy gradient (by inducing spatially varying wettability on a silicon wafer through unequal deposition of a hydrophobizing silane vapor) could be leveraged to propel liquid droplets passively on a surface (Figure 7i). They were able to induce upward motion of small water droplets (1−2 $\mu$L). On a gradient-wettability surface, a droplet is actuated by imbalanced surface-tension forces acting on opposite sides of the droplet edge given by $dF_Y = \gamma_{lg}(\cos\theta_A - \cos\theta_R)\,dx$, where $\theta_A$ and $\theta_R$ denote the advancing and receding contact angles, respectively. The resulting Young's force ($F_Y$) acting on the droplet is obtained by integrating this expression over the entire


https://doi.org/10.1021/acs.chemrev.2c00045
Chem. Rev. 2022, 122, 16752−16801

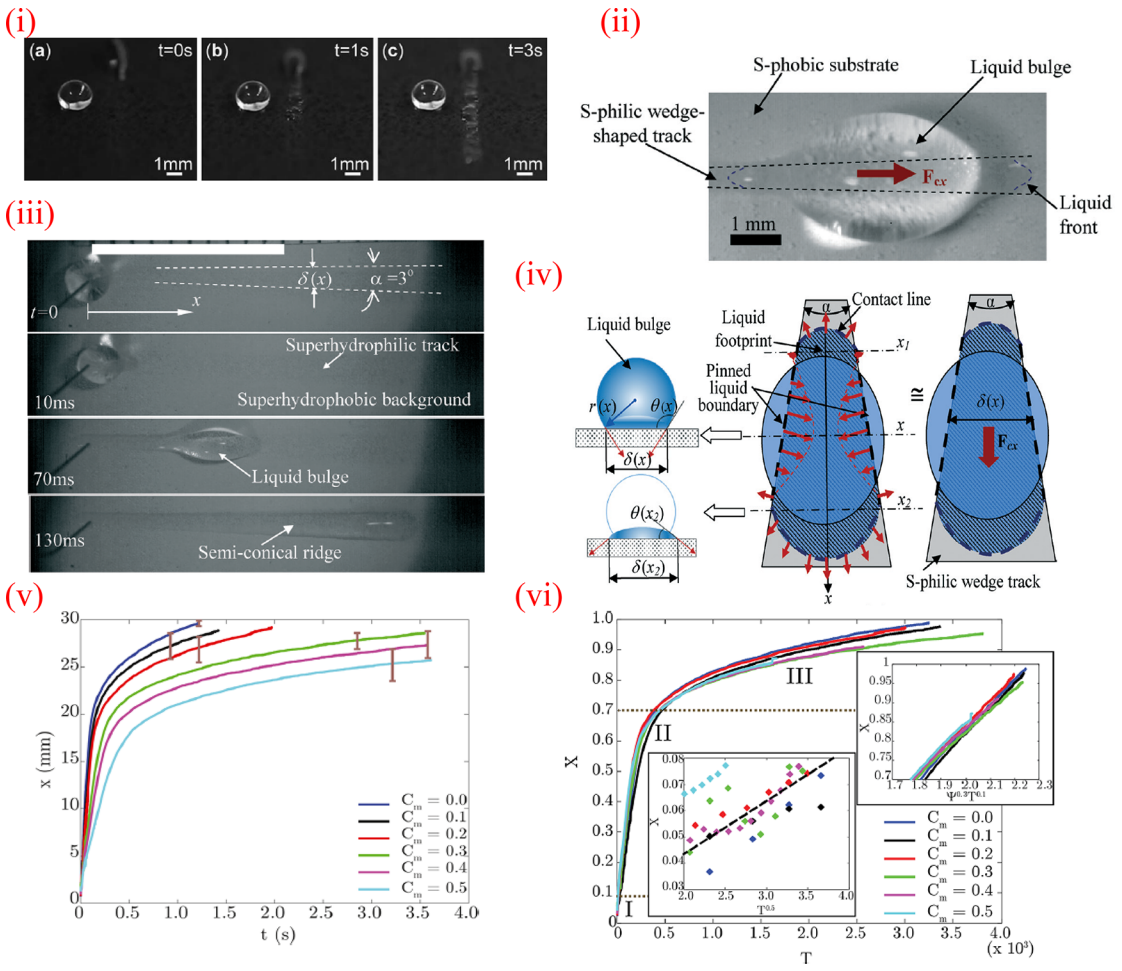


**Figure 8.** Capillary-driven directional transport of liquid on wettability confined flat tracks: (i) surface tension confined (STC) tracks created with printed wax on a superoleophobic fluoroacrylic/carbon nanofiber composite coating. Hexadecane droplets self-propelled along the straight horizontally placed track via capillary action. The stationary beaded droplet reveals the repellent nature of the surface outside the strip. Reproduced with permission from ref 45. Copyright 2012 Royal Society of Chemistry. (ii) Top-view morphology of the liquid bulge, approximated as an ellipsoid of finite footprint on the wedge-shaped superhydrophilic track, moving along the horizontal track that is surrounded by superhydrophobic area. (iii) Time-lapsed images (top view) of water transport along a wedge-shaped superhydrophilic track on a horizontal metal substrate. The white bar at the top denotes 10 mm. (iv) Origin of the driving capillary force on the liquid bulge moving along a wedge track. Reproduced with permission from ref 33. Copyright 2014 Royal Society of Chemistry. (v) Liquid-front location ($x$) at different time instants ($t$) shows influence of viscosity on the transport rate. Transport of a 50% glycerol−water mixture (viscosity ~5.6 times that of pure water) shows similar, but sluggish transport; $C_m$ indicates the mass fraction of glycerol in the water solution. (vi) Dimensionless front location ($X$), for the dimensional data shown in (v), plotted against dimensionless time ($T$), showing a universal nature of spreading under different values of liquid viscosity and surface tension. Spreading regimes I, II, and III indicate typical spreading behaviors of $X \sim T^{0.5}$, $X \sim T$, and $X \sim T^{0.1}$, respectively. Reproduced with permission from ref 162. Copyright 2018 American Chemical Society.

droplet width. If $\theta_A < \theta_R$, the droplet will move from the receding to the advancing end. For a gradient surface with contact angle changing from 97° to 25° over 1 cm, droplet motion was observed on both a horizontal and a tilted surface (15° to the horizontal), with the hydrophobic (HPB) end lower than the hydrophilic (HPL) end.[77] The same group further demonstrated that the capillary-driven transport on the gradient wettability surface can also be combined with other active modes (vibration in one case) to create ratcheting motion.[151] Ito et al. reported tunable gradient surfaces, where the magnitude of the wettability gradient was tuned by altering the photodegradation via controlled UV exposure to generate different extents of droplet motion.[152]

Bliznyuk et al.[112] took an interesting approach in fabricating a stripe-patterned gradient surface to transport liquid droplets, as shown in Figure 7ii. They fabricated substrates with alternate hydrophilic and hydrophobic stripes and varied their relative widths in such a way that the effective fraction of hydrophilic-to-total area increased along the plate. Figure 7ii shows a glycerol droplet moving on a striped silicon wafer (hydrophilic) patterned with 1*H*,1*H*,2*H*,2*H*-perfluoro-decyltrichlorosilane/PFDTS (hydrophobic). In all such cases, viscosity opposes the capillary force. Besides, surfaces exhibit contact angle hysteresis, providing an additional energy barrier for droplet motion.[77,151,153] By summarizing existing descriptions for droplet motion on gradient wettability surfaces, droplet velocity is generally determined by the balance of the driving capillary and opposing viscous forces.[77,138,151] A first-order approximation of droplet velocity by accounting for the gradient driving force and the opposing viscous force, but neglecting hysteresis, is given by


https://doi.org/10.1021/acs.chemrev.2c00045
Chem. Rev. 2022, 122, 16752−16801

$$V = \frac{\gamma_{lg} R \sin\theta}{3\eta \ln(x_{max}/x_{min})} \frac{d\cos\theta}{dx} \quad (9)$$

where the term d cos $\theta$/d$x$ denotes the spatial gradient (smoothed over the length-scale of the stripes) of wettability. Bliznyuk et al.[112] made some other useful observations about the methodology used in testing droplet kinematics on gradient surfaces. For example, they noted that the droplet deposition protocol on a gradient surface is important. Movement of both advancing and receding contact lines is induced after a droplet's connection with the dispensing needle and the surface is ruptured. The velocity enhancement can be qualitatively explained by considering the neck, which connects the droplet volume to the liquid reservoir in the supplying needle as a constrained spring. Once the neck breaks, the spring potential energy is released[154] and gets converted into kinetic energy, leading to rapid droplet elongation. They found that once the velocity peak had passed, droplet motion was controlled by the balance of three forces, inertial, viscous, and capillary, resulting in an overall decline in the measured velocities to a few mm/s, in agreement with other publications.[77,155] This highlights the care required for producing experimental droplet kinematic data that can be compared against previous works. Other aspects that require care include whether the front or rear contact line is used to determine the droplet kinematics. Liu et al.[118] furthered the development of the stripe-based gradient on silicon by introducing a nanograss with no additional coatings and noted that a HPB coating provides an inherent barrier in wettability gradient design by constraining the range from HPB to SHPB, or approximately CAs in the range 100−150°,[118] dramatically limiting the droplet transport distance. They noted that to enlarge the gradient length, an intrinsically superhydrophilic (SHPL) surface is more appropriate. Their wetting gradient had CAs ranging from 15.5° to 166° (a range >150°), and the area fraction was varied between 0 and 1 along the gradient length. These surfaces induced spontaneous droplet motion (slip mode), where in one case, a droplet traveled ∼37.5 mm;[118] this is one of the longest travel distances reported to date for gradient surfaces (see Figure 7iii). To further investigate droplet self-propulsion, Liu et al. derived a force balance consisting of the gradient driving force, resistive hysteresis and viscous drag. They used this model to determine the maximum droplet travel distance for different silica stripe lengths. Because their gradient was discrete, the forces acting on dynamic droplets were defined at points that interfaced adjacent wetting regions. Their model predicted maximum travel distances of ∼8.5 mm when the stripe length was 1.5 mm and the gradient wetting range corresponded to CAs from 39.4° to 166°. For a stripe-length-to-droplet-radius ratio of 0.83, a mean velocity of 75 mm/s was observed with maximum travel distance of 5.2 mm.

Dos Santos and Ondarçuhu[156] demonstrated that by depositing droplets of *n*-alkanes containing chlorosilane on glass (hydrophilic), the trailing end of the droplet released a thin chlorosilane film, which subsequently rendered the glass substrate hydrophobic. This created an unbalanced capillary force giving rise to, as the authors described, free-running droplets moving with velocities of ∼O(1 cm/s). Zorba et al. used a femtosecond laser-based technique to alter wettability (contact angles in the range 66−107°) of silicon by physical texturing only, without using any chemical functionalization of the surface.[157] Several other research groups used variants of the above techniques of chemical patterning and physical texturing of substrates to achieve passive liquid transport. The interested reader may find some related articles elsewhere.[48,73,106,158]

*3.1.2.3. Transport Due to Wettability Contrast in Discrete Domains.* Contrast wettability patterned substrates have also been used to induce rapid passive transport; see the simple example in Figure 5ii(b). The major difference between the transport mechanisms on surfaces with gradient wettability and those of contrast wettability is that, in the former, there is a spatially gradual change of the surface energy of the substrate, whereas in the latter, there is a step change of surface energy from one domain to the other forming well-defined wettability contrast lines. Such wettability contrast lines may be appropriately used to confine the liquid strategically. Confining the liquid is important because confinement restricts the intrinsic tendency of the liquid to spread radially and instead imparts a directionality to the flow. Dahruber et al.[159] patterned the substrate with alternate lyophobic (liquid repelling) and lyophilic (liquid loving) tracks to confine the liquid on the latter. Liquid transport demonstrated by researchers on wettability patterned surfaces has harnessed both hemiwicking and Laplace pressure-driven flow. The latter depends on the characteristic length scale of the wettable patches on the surface and the local liquid volume (section 2). Schutzius et al.[45] fabricated anisotropic wetting patterns on a superoleophobic surface (fluoroacrylic copolymer + carbon nanofibers-CNF) using wettable paraffin wax. The liquid meniscus exhibited Washburn-type transport, recording velocities up to 3.1 cm/s. Their facile and top-down patterning approach provided promise for passive handling of low surface-tension liquids. Figure 8i shows the behavior of two identical hexadecane droplets (27.5 mN/m) placed one outside the wax-coated area (beaded, left) and the other (top middle) on the wax line at three different instances; the liquid advancement along the STC track is clearly seen.

Ghosh et al.[33] reported a facile technique of developing a versatile surface-microfluidic platform, comprising a wedge-shaped superhydrophilic track laid on a superhydrophobic background on glass, metal, polymer film, or paper substrates (Figure 8ii). The approach harnessed Laplace-pressure gradients to induce rapid liquid flow along the track. When a $\mu$ volume liquid droplet was deposited at the narrow end of the track (Figure 8iii), it traversed toward the wider end on its own. Liquid deposited on the track formed an asymmetric liquid bulge that displayed progressively decreasing net curvature ($\kappa$) toward the wide end of the track. This created a Laplace pressure gradient within the changing liquid volume, achieving rapid passive transport. Velocities of ∼O(10 cm/s) and flow rates as high as ∼O(100 $\mu$L/s) were achieved with this system. These liquid transport speeds were by an order of magnitude higher compared to wicking or hemiwicking-based techniques.[45] Ghosh et al.[33] also made a scaling argument for the pressure gradient, expressed as

$$\frac{dP}{dx} \sim \frac{2\gamma_{lg} \sin\theta_{avg}\alpha}{\delta(x)^2} \quad (10)$$

where $\frac{dP}{dx}$ denotes the Laplace pressure gradient in the direction of transport $x$, $\theta_{avg}$ the average apparent contact angle formed by the bulk liquid on the wettability contrast line, $\delta(x)$ the local hydrophilic track width at the location of the droplet, and $\alpha$ the included angle of the diverging track (Figure 8iv). For more details, see Ghosh et al.[33] This transport mechanism is versatile and substrate-independent, as long as one can fabricate the contrast wettability, i.e., (super)hydrophilic−(super)-


https://doi.org/10.1021/acs.chemrev.2c00045
Chem. Rev. 2022, 122, 16752−16801

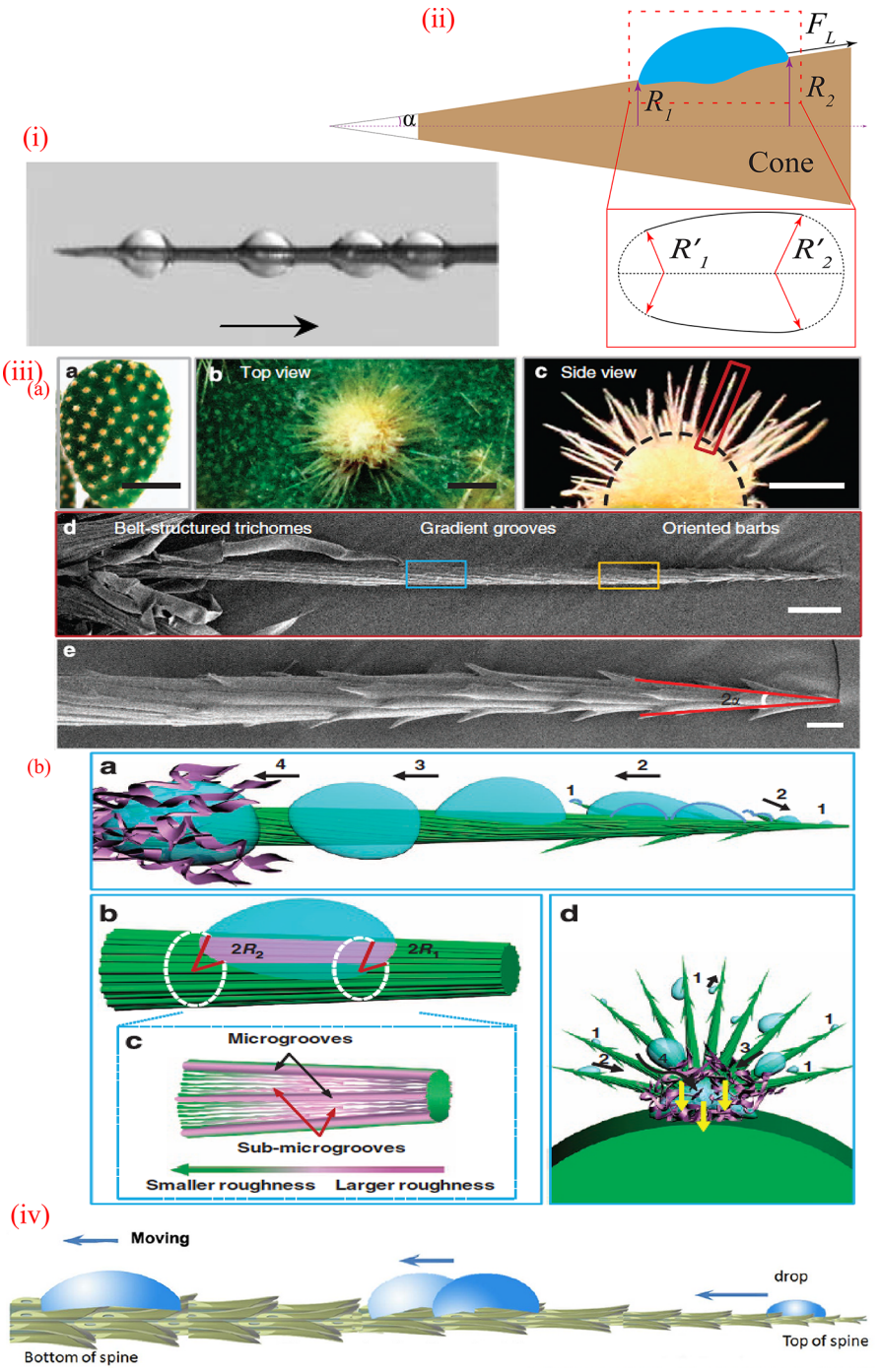


**Figure 9.** Passive transport on three-dimensional structures found in nature: (i) Multiexposed photograph (frames captured 1.6 s apart) of a millimetric, barrel-shaped drop of silicone oil (viscosity 5 mPa s) on a tapered copper wire. Reproduced with permission from ref 165. Copyright 2004 Cambridge University Press. (ii) Transport of a clam shell-shaped droplet on a conical spire structure. (iii) (a) Appearance and surface spine structures of the cactus, and (iii) (b) mechanism of fog collection on the cactus relying on the Laplace pressure gradient. Reproduced with permission from ref 170. Copyright 2012 Springer Nature. (iv) Fast droplet transport in a semiopen configuration of a splayed spine of cactus *Gymnocalycium baldianum*. Droplet moving continuously on a spine with splayed capillary microtube array composed of overlapping tilted-up scales from the tip to the base of the spine serving water self-gathering. Reproduced with permission from ref 174. Copyright 2015 Springer Nature.

hydrophobic patterns. Rapid passive transport has been attained on substrates made of paper and plastic, as well as metal.[78] Apart from rapid transport, higher-order designs made from the wedge tracks also enabled passive, complex manipulation (section 3.2) of small liquid volumes. Huang et al. further used this principle to achieve underwater passive transport of nonpolar organic liquids.[160]

It has been stated that high "science-to-mass" ratio microfluidic devices will play an important role in scientific space exploration.[161] Relying only on capillary forces, wettability confined tracks enable gravity-independent liquid transport, making it an attractive technology for passive (independent of active liquid actuation components) reduced-gravity or zero-gravity applications. Additional research is needed, nonetheless,


https://doi.org/10.1021/acs.chemrev.2c00045
Chem. Rev. 2022, 122, 16752−16801

to identify the existing usage/pain points and how one can carefully design experiments to address various challenges using wettability patterned passive microfluidics. By varying the design parameters (wedge angle $\alpha$ and length $L$) of the track, one can tune the total distance of liquid transport, velocity, and flow rate as required to accomplish specific lab-on-chip operations. Sen et al.[162] presented a generalized description of the capillary-driven transport of liquids of different viscosities and surface tension on such a superhydrophilic wedge-track laid on a superhydrophobic background. They found that for more viscous liquids, the transport rate becomes sluggish (see Figure 8v), but the overall flow trend remains similar. They further identified that when the spreading length $x$ and the time $t$ were nondimensionalized, respectively, as $X = x/L$ ($L$ being the length of the track) and $T = \gamma_{lg}t/\mu L$ ($\gamma_{lg}$ and $\mu$ being the liquid surface tension and viscosity, respectively), the nondimensionalized $X-T$ curves overlapped for fluids of widely varying viscosity and surface tension. The capillary-driven transport followed three distinct regimes (marked as I, II, and III in Figure 8vi). Regime I resembled the early stage spreading of unconfined viscous droplets through hemiwicking, yielding Washburn spreading characteristics (i.e., $X \sim T^{0.5}$); the second regime displayed a linear trend (i.e., $X \sim T$), ensuing from a balance between the driving capillary force and the viscous resistive force; the third spreading regime followed a density-augmented Tanner spreading trend (i.e., $X \sim T^{0.1}$), which arises when the spreading film thickness becomes thin enough so that the dissipation at the contact line dictates the spreading behavior. Such mode of capillary-driven transport on wedge-shaped wettability confined tracks was not restricted only to water droplets; the principle was also harnessed to transport low surface-tension liquids with $\gamma_{lg}$ as low as 23.8 mN/m.[163] For a surface immersed in water, a similar design with opposite contrast of wettability (i.e., a superhydrophobic wedge-track laid on a superhydrophilic background) was shown to induce capillary-driven transport of air bubbles dispensed underneath the wettability patterned surface.[164] Unlike the spreading of liquid droplets on a wedge track, propagation of the air-bubble front, however, showed a linear temporal variation; a scaling argument revealed that the spreading velocity for the bubble on the superhydrophobic wedge track arises from an inertia−capillary force balance and varies as the inverse of the square root of the track width.

*3.1.2.4. Transport along Three-Dimensional Conical Structures.* Laplace pressure-driven directional transport has also been realized on three-dimensional structures. A large number of these works have leveraged the Laplace pressure gradient that is developed on a wetting liquid droplet on a conical surface[165] to effect droplet motion from the tip (region of higher curvature) toward the cone base (region of lower curvature), as shown in Figure 9i. It is important to note that droplets can reside on a slender fiber in two different stable morphologies depending on the size of the droplet and the wettability of the cone, viz., an axisymmetric *barrel shape* and an asymmetric *clamshell shape*.[166−168] In a *barrel* shape, the liquid volume wraps completely around the fiber, while in the clamshell configuration, the droplet partially covers the cone. The substrate curvature gradient results in a Laplace pressure differential between the two opposite sides of the droplet. The resulting unbalanced force,[169] $F_L = \gamma_{lg}\left(\frac{1}{R_1'} - \frac{1}{R_2'}\right)\frac{\sin 2\alpha}{R_2 - R_1}V_{drop}$, as shown in Figure 9ii for a clamshell-shaped droplet, drives the droplet in the direction where the substrate curvature decreases ($\alpha$ denotes the semiapex angle of the cone, $R_1$ and $R_2$ the local substrate curvature radii at the two ends of the droplet, and $R_1'$ and $R_2'$ the curvature radii at the rear and front contact lines of the droplet, respectively). In a barrel configuration, the droplet wraps round the whole cone, and thus, the radii of curvature at the front and rear contact lines match with the local substrate curvatures at the two ends of the droplet (thus $R_1 = R_1'$ and $R_2 = R_2'$). This phenomenon is responsible for liquid transport on some biological structures, like cactus spines.[170] Based on the above biological structures, artificial systems consisting of bioinspired fibers and needles have been manufactured and used for fast water droplet collection and transport[171] (Figure 9iii). Akin to droplet transport on the outside of a cone, capillary-driven transport inside semiclosed conduits of tapered cross section has also been observed where the driving axial Laplace pressure gradient originates from the spatial variation of the curvature of the liquid conduit.[172] The same principle is harnessed to realize droplet transport in the beaks of *Phalaropes* and other types of shorebirds[173] or on splayed cactus spines of *Gymnocalycium baldianum* that feature cone-like structure covered with tilted scales[174] (Figure 9iv).

Capillary-driven droplet transport on open surfaces is a mature field in experimental interfacial science, where fluid transport has been successfully demonstrated on various wettability engineered surfaces. Admittedly, the durability of such wettability modifications remains contentious. Certain transport features have also remained elusive to this date. For example, the literature still lacks a comprehensive demonstration of purely capillary-driven rapid transport of droplets that do not leave behind a residual liquid film. The existing studies of such transports have deployed dielectric,[39] magnetic,[41] or gravity forces.[175] In contrast, for purely capillary-driven flows,[151] the transport velocity has been very low. Besides, plenty of ground must be covered in the area of numerical modeling of open-surface fluidic transport. Salient challenges in this context lie in the description of dynamic contact angle and incorporation of contact angle hysteresis at the three-phase contact line. Often, drop shapes are nonaxisymmetric on rough surfaces, rendering prediction of the contact-line velocity challenging. To the best of the authors' knowledge, no work exists for multiscale modeling capable of resolving the surface roughness features at the micro and nanoscales, while at the same time capturing fluid transport at the millimeter scale on an open surface. Although there are several works on droplet coalescence on an open surface, and capillarity-aided droplet-splitting upon impact,[33] droplet splitting *during* capillary-driven transport remains rare.[176]

## 3.2. Liquid Transport on Various Types of Surfaces

**3.2.1. Flat Surfaces.** Liquid manipulation studies have primarily focused on surfaces where the wettability modification has been brought about through chemical functionalization, micro- and nanoscale roughness features, or a combination of both.[33,45,72,73,77,78,159,162,163] Roughness induced on such surfaces were random, which originated from mechanical or chemical etching and/or depositions of nanocomposites. A detailed account of liquid transport on such surfaces has already been provided in section 3.1.

**3.2.2. Topographically Engineered Surfaces.** In contrast to the wettability engineered flat surfaces discussed in the previous section, several works have focused on generating spatial variation of wettability through imparting topographic features of specific patterns. One of the simplest examples of a topographic gradient is manifested by fixed-pitch microgrooves located adjacent to a flat uniform region on a surface (Figure 10,


https://doi.org/10.1021/acs.chemrev.2c00045
Chem. Rev. 2022, 122, 16752−16801

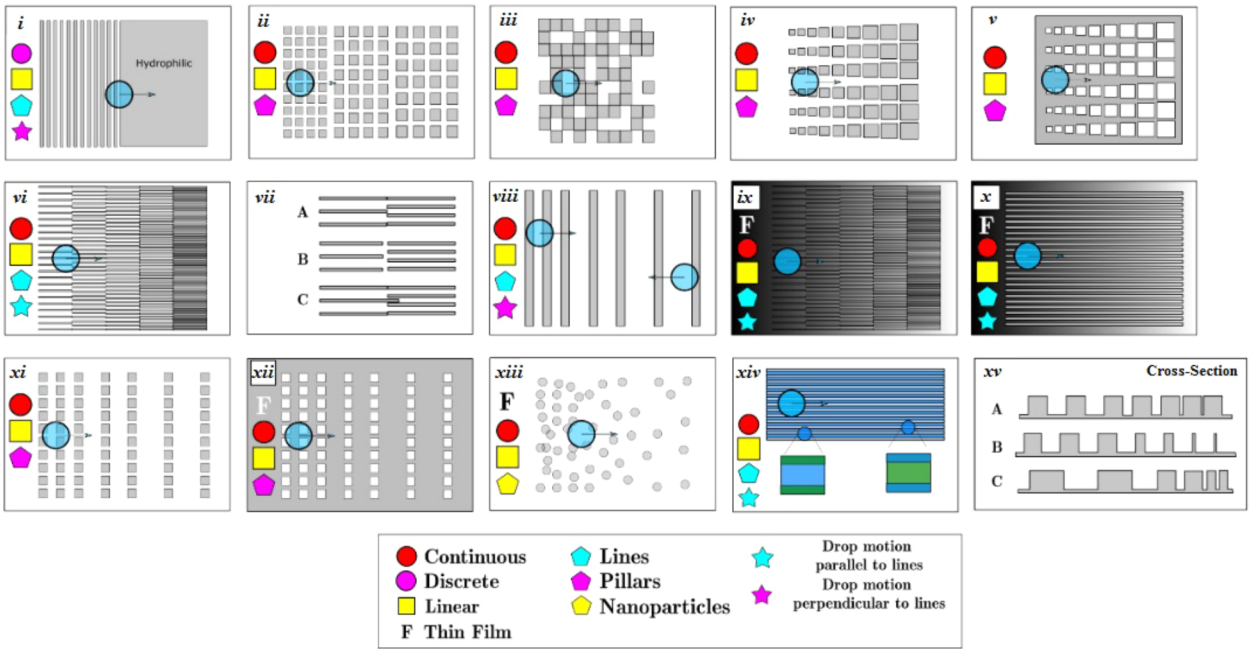


**Figure 10.** Liquid transport on linear-gradient surfaces using topography: (i) stepwise gradient: microgrooves adjacent to a flat uniform region, (ii) square micropillar arrays of varying dimensions,[102] (iii) hole-to-pillar density gradient,[109] (iv) square micropillar linear-array wedges,[122] (v) square microhole wedges,[122] (vi) biphilic surface inducing droplet motion along hydrophobic strips,[103,112] (vii) microstructural interface geometries associated with pattern (vi),[103] (viii) linear variable-pitch microgrooves,[48,104] (ix) double gradient with overlapping microgrooves,[108] (x) periodic microgrooves (10 $\mu$m pitch) plus silane coating with droplet motion parallel to grooves,[113] (xi) linear micropillar variable-pitch rows, (xii) gradient micropillar array on silicon with a fluoropolymer coating,[107] (xiii) micro/nanopatterned surface created using a stainless steel mesh and electrochemical gradient,[117] (xiv) biphilic condensing surface with hydrophobic microlines on a hydrophilic substrate,[128] (xv) different cross-sectional views associated with pattern (viii).[48,105,121]

pattern i), whereas, the topographic gradients demonstrated by Shastry et al.[102] consisted of square micropillars with silane and Teflon coatings; Figure 10, pattern ii. It is important to note that droplets moved on these gradients only with forced vibration, but the authors argued that their analytical work could be used to determine the gradient steepness required to overcome contact angle hysteresis (CAH) for spontaneous droplet motion.[102] The authors derived a CAH-corrected net force for the droplet, given by

$$F_{\text{net,droplet}} = \gamma_{\text{lg}} \frac{\mathrm{d}\phi}{\mathrm{d}x}(\cos\theta_i + 1)\pi R^2 - \frac{C}{2}\gamma_{\text{lg}}\pi R^2 - \gamma_{\text{lg}}\phi_{\text{c}}(1 - \cos\theta_{i,a})2R \quad (11)$$

where $\gamma_{\text{lg}}$ is the liquid surface tension, $\mathrm{d}\phi/\mathrm{d}x$ the variation of the surface area fraction in the $x$-direction, C a dimensional constant, and $\theta_i$ is Young's intrinsic CA. Here, the first term on the right-hand side corresponds to the gradient driving force, and the next two terms correspond to the hysteresis force. Equation 11 leads to the calculation of a CAH force that increases as a function of gradient position from ~20 $\mu$N to ~200 $\mu$N, 6 mm away. The driving force also increased while moving along the gradient, yielding a maximum value between 10 and 20 $\mu$N before decreasing to zero. Other designs were comprised of a hole-to-pillar density gradient[109] (Figure 10, pattern iii) coated with a silane monolayer. The pillars had diameters of 20−30 $\mu$m and were randomly placed across the surface. The surfaces were characterized using 6 or 9 $\mu$L droplets and had CAs > 140°. In the hole structured regions, 6 $\mu$L or smaller droplets did not move at all, and this was attributed to strong pinning and suction at points of sealed air cushions within holes.[109]

Xu et al.[122] demonstrated gradient surfaces like those shown in Figure 10, patterns iv and v, with the holes and pillars having a square cross-sectional shape. While these appear to be the only gradient surfaces of their kind, spontaneous motion was not reported for either gradient.[122] Nonetheless, the authors measured critical tilt angles and proposed a novel adhesion energy model for these surfaces.

Yang et al.[103] demonstrated the first topographic version of Figure 10, pattern vi, based on chain-configuration grooves, where the gradient direction was parallel to the microgrooves. Others have referred to similar patterns as stripe pattern gradients.[112] These gradients included a coating to increase the surface hydrophobicity. The authors noted that this micro-grooved structure sets up a Laplace pressure gradient acting as a droplet transport-inducing mechanism.[103] They also investigated different stripe pattern interfaces (Figure 10, pattern vii) labeled as connecting (vii-A), separating (vii-B), and overlapping (vii-C) configurations.[103] Spontaneous motion was reported on patterns vii-A and vii-C, but droplets got stuck at the gap on vii-B, as this increased the CAH. The stripe pattern structures in this work had a line width of 5 $\mu$m and stripe lengths of 500 and 1000 $\mu$m. More interestingly, the authors deduced the gradient driving force from a different perspective. The Laplace pressure was $\Delta P = \gamma_{\text{lg}}(1/r_1 + 1/r_2)$, with $r_1$ and $r_2$ being the two radii of curvature of the droplet surface. They noted that the droplet motion occurs from the induced Laplace pressure whenever the droplet is positioned across an interface of two regions of different roughness, such that the actuating force is given by


https://doi.org/10.1021/acs.chemrev.2c00045
Chem. Rev. 2022, 122, 16752−16801

$$F_D = \gamma_{lg} A_{eff} \left\{ \left( \frac{1}{r_1} + \frac{1}{r_2} \right) - \left( \frac{1}{r_1'} + \frac{1}{r_2'} \right) \right\} \quad (12)$$

where $A_{eff}$ is the droplet's cross-sectional area that corresponds to the maximum height, and $r_1$, $r_2$ and $r_1'$, $r_2'$ represent the radii of curvature of the two distinct regions on which the droplet simultaneously lies on its right-hand and left-hand sides (Note: The projection of the area $A_{eff}$ is orthogonal to the direction of droplet movement). Yang et al. offered a simplified form of this equation by noting that on their stripe-based gradient $r_2 = r_2'$, resulting in

$$F_D = \gamma_{lg} A_{eff} \left( \frac{1}{r_1} - \frac{1}{r_1'} \right) \quad (13)$$

Four different gradient surfaces were investigated, each with the same change in area fraction. The surfaces included photoresist AZ 6112, Teflon, Parylene C, and PPFC. The authors used the PPFC sample to discuss forces acting on the droplet during motion.

Sun et al.[105] demonstrated the design in Figure 10, pattern viii on a silicon substrate, where the gradient direction was perpendicular to the microgrooves. This surface was coated for increased hydrophobicity, but the coating itself did not form a gradient. The gradient's cross-sectional structure was similar to Figure 10, pattern xv(A). The direction of droplet motion on such surface depends on whether the droplet is in the Cassie–Baxter (CB)[177] or Wenzel (W)[178] state. Based on CB theory, a CB droplet should move toward a region of increased microgroove pitch (higher area fraction), whereas a W-state droplet should move toward a region of reduced microgroove pitch.[105] Spontaneous motion was not observed on pattern (viii). Sun et al. also produced Figure 10, pattern v, which demonstrated the spontaneous slip mode attributed to the CB state.[105] For their stripe pattern gradient, the four groups of line widths were 200, 100, 50, and 20 $\mu$m, and the channel widths were 200, 100, 70, and 40 $\mu$m, while the stripe length was ~3 mm. On this stripe-based gradient, a 10 $\mu$L water droplet was shown to move ~6 mm in 1.5 s, giving an average velocity of ~4 mm/s.[105]

Yang et al.[106] demonstrated spontaneous droplet motion on a stripe-based gradient (Figure 10, pattern v) on silicon coated with Teflon.[106] An equation for droplet velocity was derived from a force balance consisting of gradient and viscous forces, which predicted an average velocity of 62.6 mm/s, whereas the measured velocity was 62.5 mm/s. They found the driving and resistance forces at an area fraction interface of 0.25 and 0.5 to be 4.91 $\mu$N and 2.46 $\mu$N, respectively.

Lai et al. used the design in Figure 10, pattern ix, which combined a stripe-based topographic gradient and a surface coating energy gradient, thus producing a double-gradient surface.[108] Their stripe pattern had overlapping microgrooves (pattern vii-C) identical to those tested in ref 103, resulting in a slightly more gradual change in the surface energy as compared with the stripe patterns produced in refs 105 and 106. Spontaneous droplet travel distances on pattern (ix) surface without a coating, with a coating, and with a combined structure and coating were found to be approximately 2.5, 6, and 9 mm, respectively; the peak droplet velocity was ~70 mm/s.[108] Lai et al. also derived a droplet force balance using a quasi-steady model including a CAH-corrected driving force and the hydrodynamic force based on the wedge approximation. They used a CAH-corrected driving force, which for a spheroidal droplet shape is

$$F_d = 2\gamma_{lg} \int_0^{\pi/2} [\cos(\theta_A)_f - \cos(\theta_R)_r] \times \sqrt{\frac{(-a \sin\phi)^2 + (b \cos\phi)^2}{\left[1 + \left(\frac{a}{b} \tan\phi\right)^2\right]}}\, d\phi \quad (14)$$

where $a$ is the long axis and $b$ the short axis of the footprint ellipse.

Sommers et al. demonstrated a gradient design on a copper substrate, as shown in Figure 10, pattern viii, which was the first time on metal,[48] and had variable spacing, fixed channel width, and no additional coating. For a 2 mm droplet, this type of gradient demonstrated spontaneous slip mode motion with a span between 0.5 and 1 mm. Chandesris et al.[113] studied spontaneous droplet motion on a surface energy gradient superimposed onto microgrooves having a pitch of 10 $\mu$m, as described in Figure 10, pattern x. The local CA on their surface ranged from 22° to 104°. 60 $\mu$L droplets were used in the tests, which is considerably larger than most other studies. For horizontal tests, peak droplet velocities of ~60 mm/s for the patterned substrate and ~64 mm/s for the smooth substrate were obtained, with travel distances of 18 and 14 mm, respectively. Droplets were also found to spontaneously move uphill, even at 90° inclination. This is only one of a handful of works[73,113] where a passive gradient could promote upward vertical droplet motion. Chandesris et al.[113] also derived a new gradient driving force expression based on an elongated droplet, given by

$$F_d = F_{circle}(r) + 2rL\gamma_{lg} \frac{d\cos\theta}{dx} \quad (15)$$

where $F_{circle}$ is the gradient driving force for a droplet having a circular footprint and $L$ denotes the elongated length. The model was used to predict the droplet velocity and provided good agreement with measured data.[113]

Dorri et al.[115] used electrodeposition chemistry to produce a mixture of copper nanoparticles and nanodendrite structures to form a wettability gradient. Spontaneous droplet motion was only observed with the addition of a thiol coating. Reyssat et al.[107] produced a micropillar gradient surface with a fluoropolymer coating. Spontaneous droplet motion was not observed; however, droplet migration toward the hydrophilic side was observed with applied forced vibration; see Figure 10, pattern xii. Hou et al.[117] demonstrated the fabrication of a micro/nanopatterned gradient using a one-step cathodic deposition method onto a stainless-steel mesh substrate; see Figure 10, pattern xiii. The resulting gradient surface modified with 1-dodecanethiol was strongly SHPB, and the authors reported that CA measurements were not possible. An 8 $\mu$L droplet demonstrated spontaneous motion on this surface with a speed of ~18 mm/s over an estimated travel length >10 mm.

Tokunaga and Tsuruta demonstrated a fixed-pitch micro-grooved surface with HPB line widths and HPL channels;[127] see Figure 10, pattern xiv. To set up the HPB line widths and HPL channels, a thermal oxide layer was grown on the silicon with a mask that led to a HPB line width wider than the HPL channel width at one end of the substrate and the reverse on the other end. In a condensing environment, the condensate droplets moved at a microscale from a HPB line to a HPL channel; at the


https://doi.org/10.1021/acs.chemrev.2c00045
Chem. Rev. 2022, 122, 16752−16801

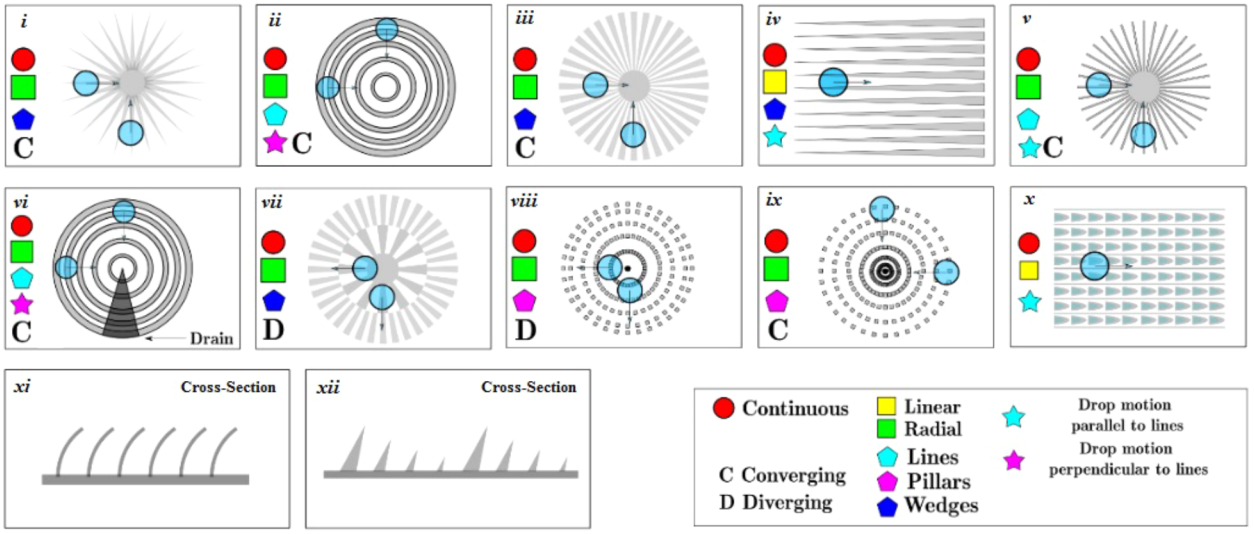


**Figure 11.** Liquid transport on radial gradients and/or compound surfaces created using surface topography directional asymmetry and/or chemical coatings: (i) radial gradient with topographic wedges pointing radially outward (droplet motion to center), (ii) radial variable-pitch microgroove rings,[104] (iii) converging radial wedges,[114,116] (iv) array of parallel microscale wedges,[72] (v) tunable radial gradient (converging/diverging) with re-entrant structure,[93] (vi) topographic coated radial gradient with drainage path,[121] (vii) diverging biphilic radial surface, (viii) diverging micropillar radial pattern,[126] (ix) converging micropillar radial pattern,[126] (x) topological fluid diode,[119] (xi) deflected nanopillar arrays,[111] and (xii) pine-needle and cactus-spine inspired pillar hybrid structure.[128]

macroscale, the HPB line width and HPL channel-width variation set up the spontaneous sweeping of larger droplets. A 10 $\mu$L droplet for example moved spontaneously with the rear end traveling ~10 mm.

Misiiuk et al. prepared a gradient type, as shown in Figure 10, pattern viii, using laser etching, which promoted a nanoscale line-edge roughness supporting a SHPB wetting state at one end of the gradient.[129] As first reported in ref 105, this style of gradient also displayed bimodal transport of liquid droplet depending upon the surface contamination. When the surface was cleaned, the Wenzel wetting state was promoted, resulting in spontaneous spreading. Once a hydrocarbon overlayer had naturally formed on the surface, the CB state was promoted, resulting in spontaneous slip movement.[129]

Whereas the previous gradients were generally linear by design, other researchers have focused on radial gradients. A topographic radial gradient presented by Khoo et al. (similar to Figure 11, pattern i) consisted of topographic wedges pointed radially outward.[104] This gradient showed spontaneous droplet spreading toward the center of the radial pattern when a droplet was deposited on the surface. Two gradients were tested, one having 20 wedge-shaped features and the other 40 features. For the former surface, droplet velocity and travel distance on the front and rear edges were found to be 72.5 and 52.5 mm/s and 1.5 mm and 1.25 mm, respectively, for a 1.1 $\mu$L droplet. On the surface with 40 wedge shapes, a 0.4 $\mu$L droplet was tested, and the front and rear edge velocities were much smaller, showing a maximum speed at both edges just over 2.75 mm/s.[104]

Sun et al. produced a converging topographic gradient like that shown in Figure 11, pattern ii,[105] with a cross-section similar to Figure 10, pattern xv(A), and a uniform silane coating to reduce wettability. The authors noted that droplets did not move spontaneously on this gradient despite the combined effect of both coating and topographic gradients; nonetheless, this work remains one of the earliest attempts at achieving droplet motion on a radial gradient. Li et al. fabricated a converging compound gradient consisting of microscale grooves configured similar to Figure 11, pattern iii.[114] It is noted that the wedges in that pattern are magnified to clarify their shape, whereas in ref 114 a close-up image was needed to show this shape. Droplets moved spontaneously on this surface toward the HPL center; the observed velocity of a 3 $\mu$L droplet was up to 40 mm/s. A 1.5 $\mu$L droplet would reach the center of the gradient if placed 1.5 mm from the center with an average velocity of 30 mm/s. The same measurements were carried out for 4 and 5 $\mu$L droplets, both showing the same speed and travel distance of 25 mm/s and 2.5 mm, respectively. Droplet motion was also studied on an array of wedges by Khoo et al.[72] (similar to Figure 11, pattern iv) with reported droplet velocities reaching 0.5 m/s.

Zamuruyev et al. presented a converging topographic gradient[116] that was similar to Figure 10, pattern vi, but with the microgrooves converging to a point in a radial pattern. The lines appeared to overlap in places (Figure 10, pattern vii(C)), and like other similar patterns, the converging gradient induced spontaneous droplet motion. Zamuruyev et al. found that upon coalescence, droplets could transition from the Wenzel state to the CB state, and they noted that this characteristic was important for self-cleaning.[116] This work investigated both dry and condensing wetting characteristics. For the dry surface, maximum droplet velocity and travel distance were found to be ~22 mm/s and just over 6 mm, with the measured values of driving, CAH and viscous forces being ~7.8, ~5.8, and ~2 $\mu$N, respectively.

Li et al.[93] presented a radial gradient, similar to Figure 11, pattern v, that could be tuned to spontaneously converge a droplet toward the HPL center, pin the droplet, or spread it away from the center. A key novelty of that work was that the microgrooves were undercut, thus creating re-entrant structure, thereby enhancing the effective wetting state.[179] For a 1 $\mu$L hexadecane droplet, a travel length ~2.6 mm was observed (droplet center measurement).

Liu et al. developed a radial gradient fabricated on silicon, like that shown in Figure 10, pattern vi, but wrapped around in a circular shape.[118] Spontaneous droplet motion (slip mode) was


https://doi.org/10.1021/acs.chemrev.2c00045
Chem. Rev. 2022, 122, 16752−16801

demonstrated, and the droplet traveled in a ∼180° circular arc (Figure 6a[118]). Yasuda et al.[101] tested a 5 μL droplet on a curved wedge array, but specific quantitative results were not presented. Additionally, no example images of their patterns were provided.

Sommers et al.[121] demonstrated a converging radial gradient like that shown in Figure 11, pattern vi, fabricated on a copper substrate, with the cross-sectional configuration similar to Figure 10, pattern xv(B). Their radial gradient was designed with a gutter region to allow droplets to drain away from the HPL center when oriented vertically. The microgroove width and depth were 25 and 100 μm, respectively. The channel spacing was varied to promote the gradient structure. Droplets were anticipated to be in the Wenzel state on this surface under condensing conditions, and as such, the same gradient design model presented in ref 48 was used to design this radial gradient. Injected droplets (5−38 μL) were studied, and spray testing was performed.[121] The droplets were observed to move spontaneously toward the gradient center (i.e., the HPL region). Travel distances for 5 and 10 μL droplets peaked around 2.3 and 2.2 mm, respectively, and the maxima were determined based on different droplet injection locations across the gradient. Travel distances as large as ∼4 mm were observed, depending on the starting location and droplet volume.

Wang et al.[124] created a bidirectional wettability gradient using a converging radial gradient similar to Figure 11, pattern v, and the authors referred to the microgrooves as microfin structures. The 50 μL water droplets moved spontaneously toward the HPL center when deposited on the dense-grooved region (where droplets initially exhibited a CB state). However, when a droplet was deposited on a wetted surface, or in a region of low-density lines (where it initially exhibited a Wenzel state), it moved to the outer region of the gradient. The pertinent driving capillary force was derived after accounting for the microfin geometry following the approach of Zheng et al.,[180] so that

$$F_D = -\pi R_b^2 \gamma_{lg} \frac{nd(1 + \cos\theta_o)}{2\pi R^2} \quad (16)$$

where $b$ denotes the groove width, $n$ the number of microfins, $d$ the width of a microfin, and $\theta_0$ the intrinsic contact angle of the droplet on the smooth wall. The average droplet speed was 30 mm/s in the CB state, and the distance traveled was ∼3 mm. When the surface was in the Wenzel state, the average speed was 48 mm/s, and the droplet moved by a greater distance, ∼3.85 mm. The maximum average speed obtained in this work was slightly over 50 mm/s.

Kumar et al. demonstrated various converging and diverging gradient patterns of micropillars,[126] shown in Figure 11, patterns viii and ix. The converging pattern was designed with the micropillar pitch decreasing toward the center; whereas for the diverging pattern, the micropillar pitch increased toward the center.[126] This study did not investigate droplet deposition at a location where the gradient could propel the droplet, instead focusing on the wetted perimeter when a droplet was deposited in the central part of the gradient. The authors found that a droplet's wetted diameter for the radially decreasing structure was smaller than that observed for the radially increasing surface.

Li et al.[119] developed a so-called "topological fluid diode," a surface structure capable of passively spreading a droplet while keeping one end pinned (see Figure 11, pattern x). Wang et al.[120] demonstrated a means of producing a passive wetting gradient using velocity-controlled laser etching to fabricate hierarchical micro/nanopatterned features on stainless steel, where they found that different laser velocity sequences could be used to produce different gradient results. Yang et al.[125] demonstrated a method for fabricating a gradient of dimples on a $Si_3N_4$ ceramic using a femtosecond laser, where the surface with the highest microdimple density showed the fastest spreading with corresponding spreading speeds ∼17.5 mm/s.

Chu et al.[111] presented a surface consisting of asymmetric nanopillars. A thermal bimetallic effect was employed to promote nanopillar deflection, where deflection angles could be controlled between 2° and 52°. The nanopillar arrays were uniform and their cross-sectional geometry is shown in Figure 11, pattern xi. These surfaces demonstrated a spontaneous spreading mode where one droplet edge was pinned, while the other end would spread in the direction of the tilted nanopillars.[111] Feng et al.[128] demonstrated an interesting gradient surface inspired by pine needles and cactus spines and demonstrated spontaneous droplet motion (see Figure 11, pattern xii). A zinc oxide overcoat was used to increase hydrophobicity, and an interesting tip-induced flipping mechanism was observed on the asymmetric pillars.

**3.2.3. Wrinkled Surfaces.** Wrinkled surfaces (Figure 12) can be fabricated by applying a strain to a substrate of interest.

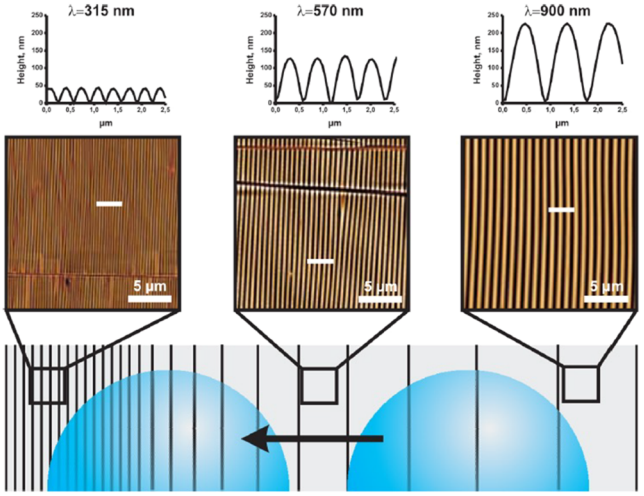


**Figure 12.** Wrinkle gradient concept with water droplet (in blue) moving toward domains of higher wrinkle density (i.e., smaller wrinkle dimensions). The white bars in the AFM images (middle row) indicate the location where the cross sections were measured (at top). Adapted with permission from ref 181. Copyright 2016 American Chemical Society.

The wrinkle wavelength ($\lambda$) and amplitude ($A$) were determined in ref 123 in terms of $\bar{E} = E/(1 - \nu^2)$ where $E$ and $\nu$ are the elastic modulus and Poisson's ratio of the material, respectively. With the subscripts $f$ and $s$ referring to the film and substrate, respectively, the critical strain for wrinkle formation is[123]

$$\varepsilon_c = \frac{1}{4}\left(\frac{3\bar{E}_s}{\bar{E}_f}\right)^{2/3} \quad (17)$$

The relationship between the wrinkle structure relative height and the prestrain was[123]


https://doi.org/10.1021/acs.chemrev.2c00045
Chem. Rev. 2022, 122, 16752−16801

$$\frac{A}{\lambda} = \frac{1}{2\pi}\frac{\left(\frac{\varepsilon_{pre}}{\varepsilon_c} - 1\right)^{1/2}}{\left(\frac{\bar{E}_f}{3\bar{E}_s}\right)^{1/3}} = \frac{1}{\pi}\sqrt{\varepsilon_{pre} - \varepsilon_c} \quad (18)$$

Langley et al.[110] presented a microgrooved gradient of a prestrained elastomer coated with thermally evaporated aluminum. A difference in advancing and receding CAs was observed for droplets on the surface. Motion was induced only in a preferential direction when a forced vibrational frequency similar to that of the water droplet was applied.[110] A 10 $\mu$L water droplet on a wrinkled gradient surface, when vibrated at an amplitude of 600 $\mu$m close to its resonance frequency of 210 Hz, resulted in an average speed of 200 $\mu$m/s.[110] Hiltl and Boker[181] realized spontaneous droplet motion, without any forced vibration, to a speed of ∼5 mm/s by leveraging wrinkled gradient surfaces prepared using bilayer materials (PDMS and $SiO_x$, with each layer having different mechanical properties resulting in wrinkling upon strain release). They also noted that the mechanism of motion for each side of the 3 $\mu$L volume droplet was different, while the front side demonstrated the stick−slip mechanism due to pinning on the nanostructure, and the rear end demonstrated continuous motion.

Chai et al. demonstrated a double-gradient on a wrinkled surface, comprising a chemical gradient and a pillar gradient.[123] This had similarities to the surface presented in ref 113 in that the microgrooves and gradient direction were parallel; as a result, droplets moved along the microgrooves.[123] Water droplets were tested separately on a surface with just the chemical gradient, the wrinkled surface plus the pillar gradient, as well as the wrinkled surface including both the pillar and chemical gradients. The droplet showed the least motion (i.e., shortest spreading distance) on the chemical gradient. On the wrinkled surface with the pillar gradient (single-gradient surface), droplets demonstrated spontaneous spreading toward the HPL region. For the double-gradient surface, spreading intensified toward the HPL region producing the longest droplet elongation. Because the wrinkle structure was parallel with the gradient direction, the former was expected to modify the droplet shape but not lead to a droplet driving force. The authors also tested in situ and ex situ controls of the droplet spreading length by applying external strain. A key finding was that the spreading length of a 5 $\mu$L droplet fluctuated between 6.8 ± 0.6 and 10.5 ± 0.5 mm under the effect of external strain.

While much work has been published in the area of wettability gradients and many different designs have been demonstrated, most efforts to date have centered on traditional substrate materials (i.e., silicon, glass, etc.) and have employed simple gradient designs (i.e., linear, radial, etc.). Very little work has been performed on metal substrates, which serve as the primary material in many engineering applications. Furthermore, curvilinear droplet paths are still largely unexplored with a couple of exceptions.[118,119] What are the special requirements in laying the wettability gradient for the design to perform in microgravity environments? These are still largely unanswered questions. Moreover, most of the works to date have focused on deposited droplets, whereas in some applications, droplets originate on the surface via condensation or melted frost.[78,182] More research is needed in this space to verify the efficacy of wettability gradients for these types of applications. Is self-propelled droplet behavior still evident? Furthermore, some of the capillary-driven transport on wettability patterned surfaces rely on precise initial positioning of droplets in order for droplet travel to occur, such as on confined wettability tracks (i.e., wedge-shape gradients, etc.). It is not widely documented how such surfaces would perform when the droplets grow (or are dispensed) at random locations. Another area for continued research and investigation is the application of wettability gradients to low-surface-tension liquids, where omnidirectional spreading behavior is more commonly seen. Clearly, a different approach is needed here to attain rapid, directional transport.[163]

#### 3.2.4. Slippery Liquid-Infused (SLIP) Porous Surfaces.

The self-propelled droplet transport described so far in this review is restricted by the liquid viscosity and pinning force due to CAH. Several studies have emerged in an attempt to lower the liquid−solid adhesion by leveraging a biomimetic approach. Taking cue from the pitcher plant (*Nepenthes alata*), which features hierarchical micro/nanotextured surfaces with a stable lubricant layer locked in the crevices of the surface of the leaves, researchers have developed lubricant-infused surfaces. Wong et al.[183] proposed detailed mechanisms for fabricating slippery liquid-infused porous surfaces (SLIPS). In general, SLIPS require a micro/nanotextured rough solid with a positive spreading parameter $S$, where the lubricant could quickly spread to form a stable oil film. SLIP surfaces can only be used to repel liquids that are immiscible with the infused lubricant. These surfaces have advantages, such as self-healing, very low CAH, etc. Therefore, these surfaces are used to manipulate liquids for different applications. Although SLIPS reduce the CAH, they cannot create any net force to propel the droplet in any direction. Generally, the movement of the droplets is demonstrated in the gravitational direction and/or in the direction of overall surface energy gradient created through a spatial gradient of topography.

It is important to note that liquid manipulations on SLIPS requires a proper understanding of the underlying physics of the interactions of four distinct phases, namely the liquid, the lubricant (oil), air, and solid surface. Earlier, Smith et al.[36] provided a detailed thermodynamic analysis of the possible configurations of a droplet on a SLIP surface. The choice of lubricants can control droplet motion. It has been observed that low-viscosity droplets, like water, roll over SLIP surfaces with velocities inversely proportional to the lubricant viscosity.[36] The spreading of liquid on SLIPS is dependent on the spreading coefficient $S = \gamma_{wa} - \gamma_{wo} - \gamma_{oa}$, where $\gamma$ represent the surface energy, and the subscripts wa, wo, and oa denote the water−air, water−oil, and oil−air interfaces, respectively. For $S < 0$, the oil does not spread over the water, whereas, for positive $S$, the oil covers the water, leading to cloaking.[36] The apparent contact angle on a SLIP surface can be estimated from Young's equation,[184] which derives $\cos\theta = \frac{\gamma_{oa} - \gamma_{ow}}{\gamma_{oa} + \gamma_{ow}}$. On a tilted surface, a droplet generally slides over a SLIPS; however, Smith et al.[36] showed that the droplet could roll over the surface when a highly viscous lubricant was present. The velocity $V$ of the droplet compared to the velocity $V_i$ at the water−oil interface can be written as[36]

$$\frac{V_i}{V} \sim \left(1 + \frac{\mu_o R}{\mu_w h}\right)^{-1} \quad (19)$$

where $R$ is the droplet radius and $h$ the lubricant's thickness, whereas, $\mu_o$ and $\mu_w$ are the viscosities of the lubricant oil and water, respectively. Keiser et al.[185] showed that the velocity of the droplet on a plate tilted at an angle ($\alpha$) is proportional to the in-plane component of the droplet weight for $\mu_w \gg \mu_o$ so that


https://doi.org/10.1021/acs.chemrev.2c00045
Chem. Rev. 2022, 122, 16752−16801

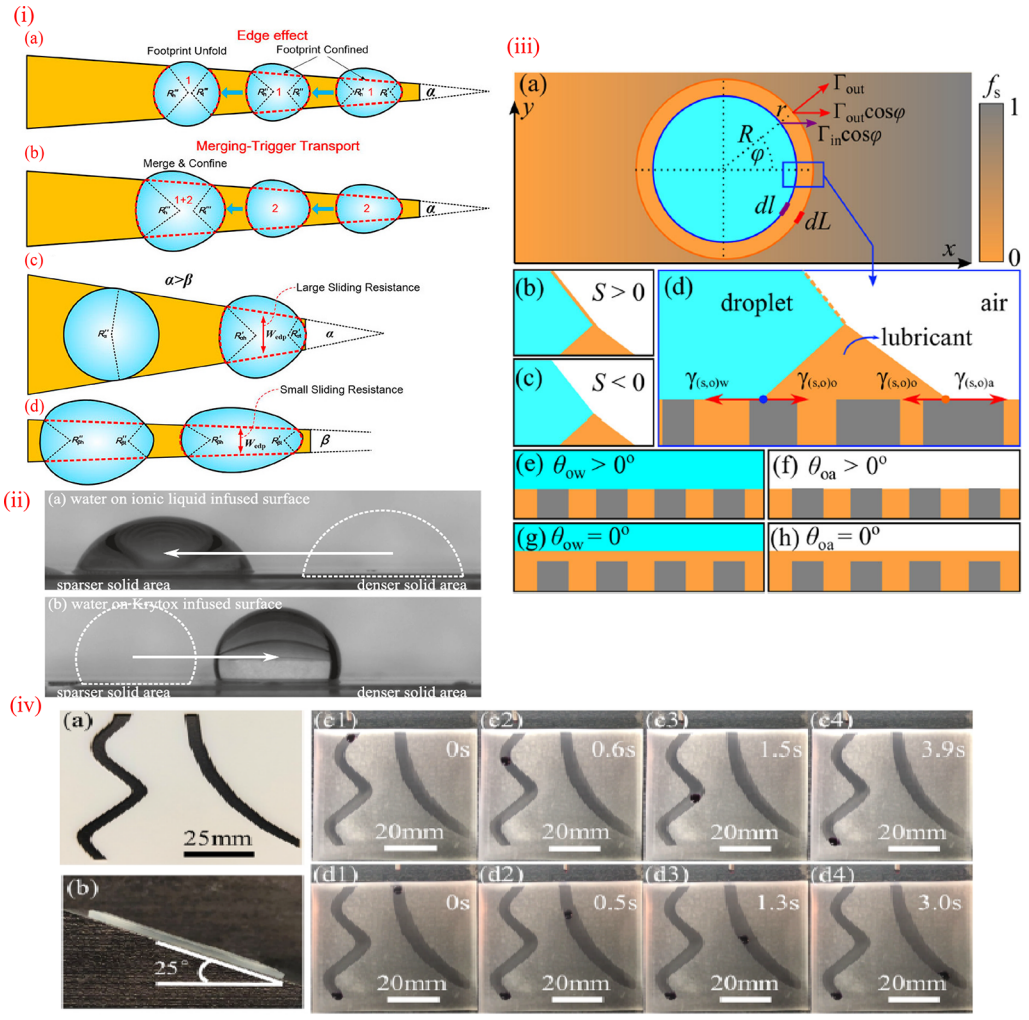


**Figure 13.** Liquid transport on SLIPS. (i) Droplet moving along a wedge-shaped SLIPS. (a) Schematic of self-driven droplet transport, (b) merging of a droplet with another droplet, which triggers further motion, (c,d) schematic depiction of droplet transport for different wedge angles. Reproduced with permission from ref 184. Copyright 2021 American Chemical Society. (ii) Side view of droplet transport on SLIPS containing solid−liquid contact fraction gradient. Reproduced with permission from ref 186. Copyright 2020 Springer Nature. (iii) Schematic of droplet placed on a solid surface gradient. Spreading of the liquid for positive and negative spreading parameters shown in (b) and (c), respectively. Infusion schemes by Krytox oil layers for different contact angles are shown in (e−h). Reproduced with permission from ref 186. Copyright 2020 Springer Nature. (iv) Droplet movement on different types of inclined SLIPS tracks on a tilted surface (25° with horizontal). Reproduced with permission from ref 187. Copyright 2020 American Chemical Society.

$$V \sim \frac{\rho g R^2}{\mu_w} \sin \alpha \tag{20}$$

For $\mu_w \ll \mu_o$, the droplet experiences a nonlinear frictional force and its velocity is dependent on the fraction $\varphi$ of the surface covered by the oil. The droplet velocity is expressed as

$$V \sim \frac{(\rho g)^{3/2} R^3}{\gamma_{oa} \mu_w \beta \varphi^{3/2}} \sin^{3/2} \alpha \tag{21}$$

Here, $\beta$ is the dissipation at the tip of the meniscus. Thus, in this case, with increased microstructure fraction, the velocity of the droplet declines due to increased friction.

Yang et al.[184] reported droplet transport on a grooved nanotextured SLIPS. They also demonstrated droplet transport on a nanotextured wedge-shaped SLIPS (Figure 13i) on a superhydrophobic background surface. This design ensured the self-driven transport of the droplet on the SLIPS even in the absence of gravity. When placed on the wedge-shaped SLIPS, the dispensed liquid is squeezed into an egg-shaped volume with different curvatures at the front ($R_f$) and back ($R_b$) of the droplet. This curvature difference generates a Laplace pressure difference,[184]

$$\Delta P \approx 2\gamma_{wo}\left(\frac{1}{R_b} - \frac{1}{R_f}\right) \tag{22}$$

The droplet moves on the SLIPS as long as the net driving Laplace pressure difference is greater than the sliding resistance. The sliding resistance for cloaking SLIPS can be estimated as

$$F_r \approx \gamma_{wo} W_{dp} (\cos \theta_R - \cos \theta_A) \tag{23}$$

Here, $W_{dp}$ is the droplet's interfacial width normal to the moving direction, while $\theta_A$ and $\theta_R$ represent the advancing and receding contact angles, respectively.

Unidirectional droplet motion can also be achieved by leveraging a solid fraction gradient (i.e., fractional area of the sessile droplet in direct contact with the solid) on the surface.


https://doi.org/10.1021/acs.chemrev.2c00045
Chem. Rev. 2022, 122, 16752−16801

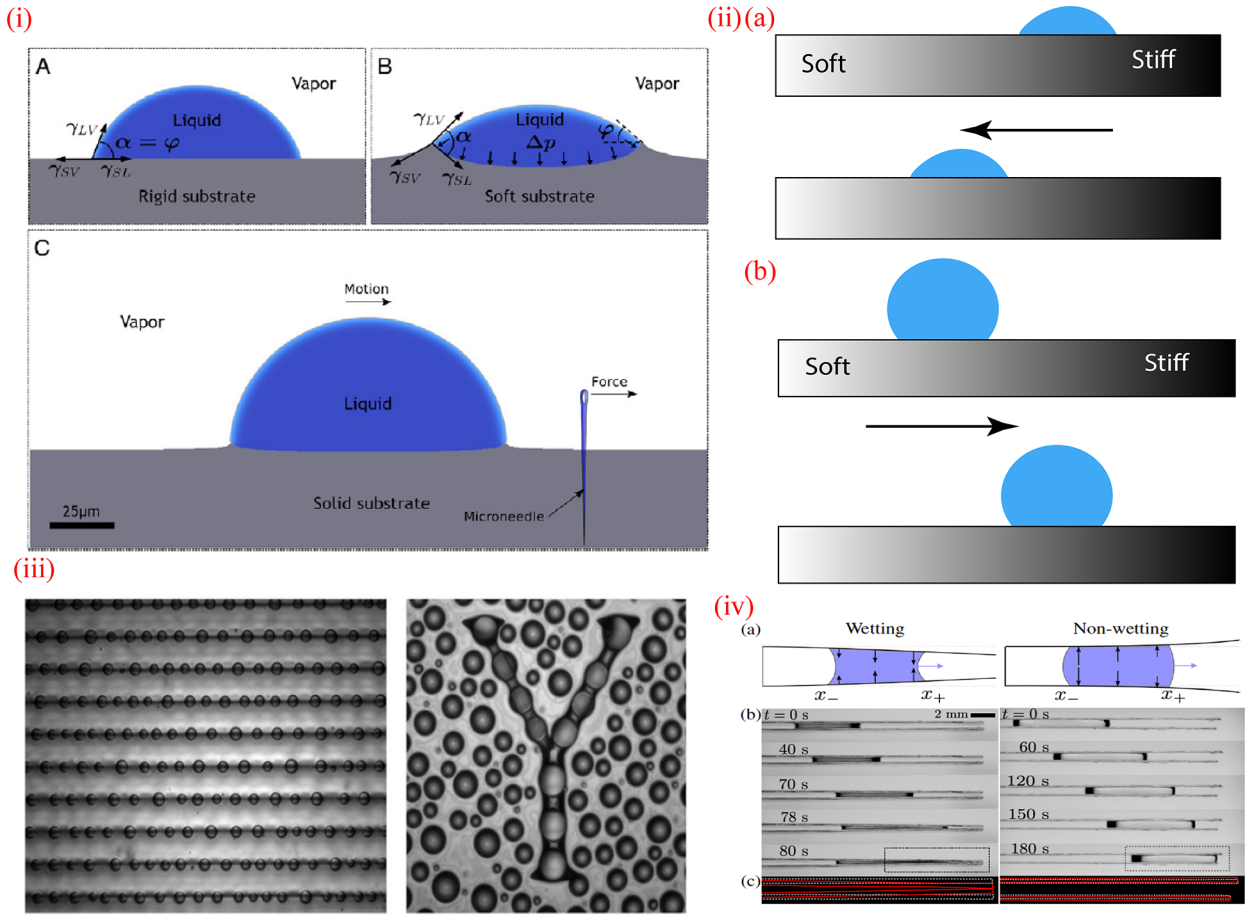


**Figure 14.** Droplet motion on soft surfaces. (i) (A) Schematic of a droplet on a rigid substrate, (B) droplet shape on a soft substrate. The apparent contact angle is $\varphi$. (C) Droplet motion due to tensotaxis. Reproduced with permission from ref 191. Copyright 2017 Elsevier. (ii) Droplet motion on a soft surface due to durotaxis: (a) a wetting droplet moves toward the softer part, while (b) a nonwetting droplet moves toward the higher-stiffness domain. (iii) Droplets organized on a soft surface due to durotaxis during condensation experiments. Reproduced with permission from ref 192. Copyright 2013 National Academy of Sciences. (iv) Wetting and nonwetting liquid transport on flexible channels due to bendotaxis. Reproduced with permission from ref 193. Copyright 2019 American Physical Society.

Sadullah et al.[186] have shown that the solid fraction gradient SLIPS can be used to control bidirectional droplet motion (Figure 13ii). The driving force on the droplet can be expressed as[186]

$$F_r \approx \gamma_{\text{eff}}\{\cos(\theta^{\text{eff}}_{\text{wals}}) - \cos(\theta^{\text{eff}}_{\text{walo}})\}\int_{\varphi} f_s(x)\cos(\varphi)Rd\varphi \quad (24)$$

Here, $\theta^{\text{eff}}_{\text{wals}}$ and $\theta^{\text{eff}}_{\text{walo}}$ are the effective contact angles of the drop on a smooth and lubricant-infused surface, respectively (the droplet radius is $R$ and the angle in the azimuthal direction is $\varphi$, as shown in Figure 13iii(a)). As the solid fraction ($f_s$) and the effective surface tension ($\gamma_{\text{eff}}$) are positive quantities, the direction of the motion of the droplet is dependent on the quantity ($\cos\theta^{\text{eff}}_{\text{wals}} - \cos\theta^{\text{eff}}_{\text{walo}}$). For an ionic-liquid-infused surface (e.g., BMIM), $\cos\theta^{\text{eff}}_{\text{wals}} < \cos\theta^{\text{eff}}_{\text{walo}}$; hence, the droplet moves toward the sparser solid area. On the contrary, for a nonionic-liquid-infused surface (e.g., Krytox) $\cos\theta^{\text{eff}}_{\text{wals}} > \cos\theta^{\text{eff}}_{\text{walo}}$, and the droplet motion occurs toward the region of denser solid fraction[36] (see Figure 13iii). Liu et al.[187] adopted a facile fabrication technique for creating wettability patterned SLIPS on superhydrophobic PDMS by using a sandpaper mold and a silanizing agent. Using a mask during plasma etching followed by oil impregnation, they created patterned SLIPS, as shown in Figure 13iv. They demonstrated the transport of liquid by tilting the surface at a certain angle.

In SLIPS, it is possible to transport a droplet without spreading. Therefore, the chances of volumetric loss of liquid due to a remnant sacrificial layer on the substrate are less. Although SLIPS provide a very low CAH and moderate stability in different conditions, controlling the drainage of the infused oil along with the transported liquid droplet has remained a challenge. In any circumstances, if the oil drains out or vaporizes, the SLIPS can no longer function as intended. The stability of the SLIPS depends on how well the lubricant adheres to the surface roughness. Recently, Laney et al.[188] showed that a precisely engineered nanostructure using silicon nanotubes on the surface resulted in better lubricant retention than the surfaces containing nanoholes or nanopillars. For more details on the different fabrication techniques of SLIPS, the reader is referred to the review by Villegas et al.[189]

**3.2.5. Soft Surfaces.** When a droplet is placed on a solid surface, the contact angle at the three-phase contact line can be estimated based on the surface tension of the different phases following Young's equation (Figure 14iA). However, Young's equation is valid only for a rigid flat surface, and it fails when elastocapillary forces dominate. The elastocapillary length scale ($L_f \sim \frac{\gamma_{lg}}{E}$) provides the relationship between the droplet size and


https://doi.org/10.1021/acs.chemrev.2c00045
Chem. Rev. 2022, 122, 16752−16801

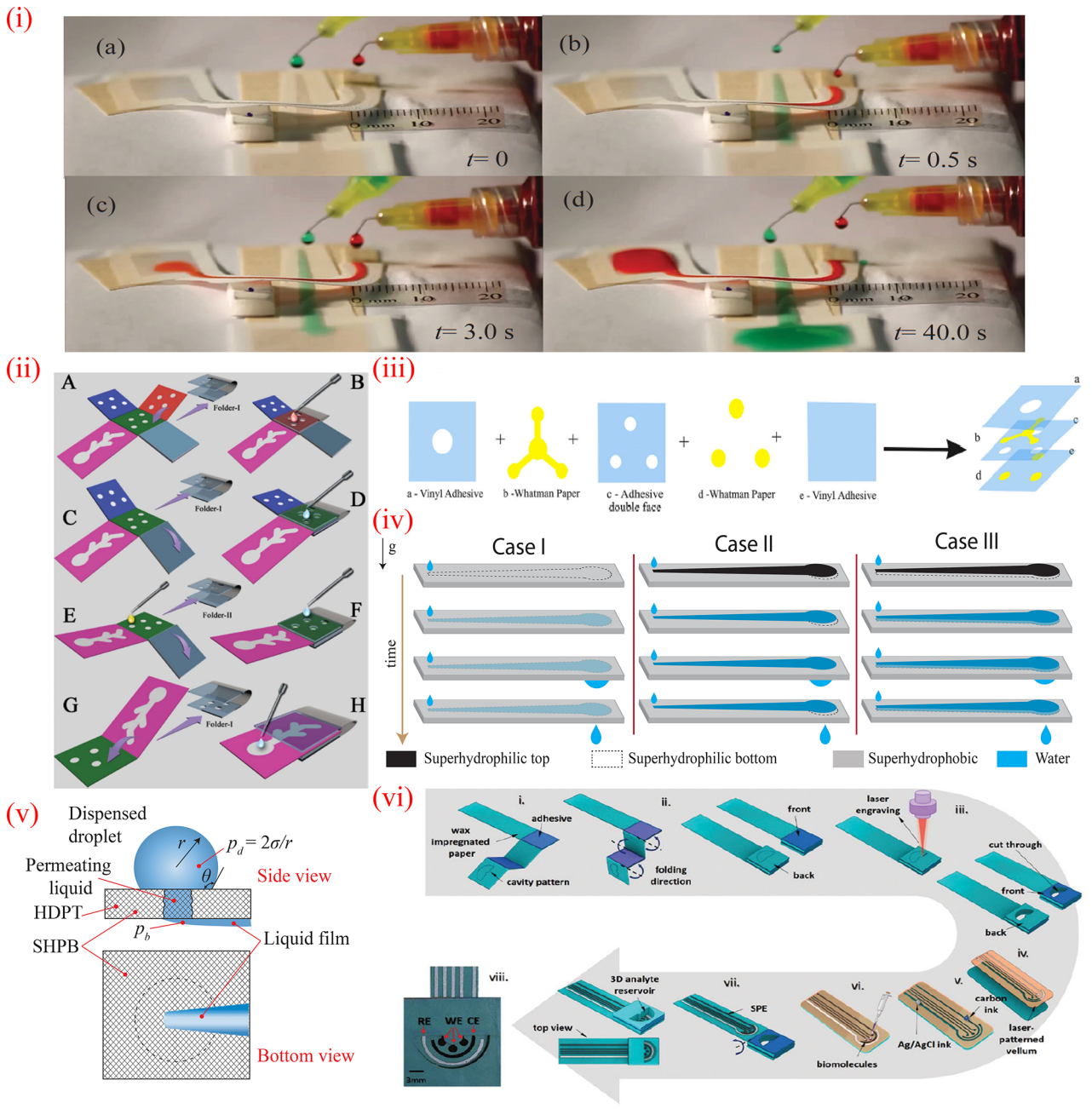


**Figure 15.** Three-dimensional transport of liquid microvolumes. (i) Combination of a straight (placed horizontally) and a curved (up and down ramp) wedge track demonstrating 3D liquid transport in a "highway overpass" design: (a) before dispensing the liquid droplets, and after dispensing (b,c) the first droplet pair (4.7 $\mu$L each), (d) after 17 droplets (~80 $\mu$L) dispensed on the curved track and 28 droplets (130 $\mu$L) on the straight one.[91] (ii) Origami-based 3D paper device assembly. Different tabs are folded in sequence to make the compact device. Reproduced with permission from ref 198. Copyright 2012 Royal Society of Chemistry. (iii) Cutting and sealing of filter papers to create a 3D device. Liquid permeates from one layer to the other through the holes and via wicking in the filter paper. Reproduced with permission from ref 200. Copyright 2017 Elsevier. (iv) Mechanism and local wettability control strategies of liquid transport on and through thin porous substrate (paper towel). In each case, the liquid droplet is dispensed at top left and emerges from the bottom right. (v) Demonstrated mechanism of droplet penetration from the superhydrophobic side (top) of the paper to a superhydrophilic wedge confined by superhydrophobic surroundings at the bottom side. (iv,v) Reproduced with permission from ref 34. Copyright 2018 American Chemical Society. (vi) 3D device with a 3D analyte reservoir. Reproduced with permission from ref 202. Copyright 2018 Royal Society of Chemistry.

Young's modulus $E$ of the surface. For soft surfaces like gels, if the droplet diameter is smaller than $L_f$, ridges form on the surface (see Figure 14iB) along the three-phase contact line. The interfacial force and the Laplace pressure create dimples on the surface, resulting in a noncircular contact line. For a nonwetting droplet, the imbalance in the horizontal forces created due to the difference in apparent contact angles on the opposite sides may propel the droplet on the soft surface.[190]

The droplet motion on deformable soft surfaces is complicated, thus the corresponding physics is not well understood.[190] The droplet transport due to the gradient of strain on the surface is known as tensotaxis.[191] The other mechanism of droplet transport on deformable surfaces, known


https://doi.org/10.1021/acs.chemrev.2c00045
Chem. Rev. 2022, 122, 16752−16801

as durotaxis, works due to a gradient of stiffness.[190] During durotaxis, the droplet moves toward the softer part of the substrate. The mechanisms of tensotaxis and durotaxis are commonly observed in cells, e.g., fibroblast cells, which move toward regions of higher compressive strain. Experimental studies of tensotaxis and durotaxis are sparse in the literature due to the complexity of creating surfaces with the gradient in strain but not in stiffness, and vice versa. Thus, both tensotaxis and durotaxis coexist during experimentation. Triggering tensotaxis is possible, as shown in Figure 14iC, by inserting a needle in a soft substrate and moving it nearby. Bueno et al.[190] provided a detailed theoretical understanding of the wetting and nonwetting droplet motion due to durotaxis. According to their findings, the wetting droplet moves toward the softer part of the surface, whereas the nonwetting droplet moves toward the area having higher stiffness, as shown schematically in Figure 14ii. Through the contact angle measurements on the advancing and the receding sides of the droplet for the cases of wetting and nonwetting droplet, Bueno et al.[190] explained that the droplet always moves toward the smaller apparent contact angle formed on the surface. The authors have also shown that, with confinement, it is possible to invoke the Laplace pressure and manipulate the droplet easily on the surface. Style et al.[192] experimentally demonstrated the control of droplet position and large-scale patterning of the droplet shape, based on the durotaxis behavior. As shown in Figure 14iii, the droplets organize in a particular direction during condensation on a soft surface. The prepared surface has nonuniform thickness; thus during the condensation process, the droplets quickly coalesce and move toward the thickest part of the surface via durotaxis.

Capillary-induced bending of deformable substrates has also been found to help transporting droplets. This type of droplet transport mechanism is termed bendotaxis; Bradley et al.[193] have shown experimentally that the direction of the droplet motion is independent of its wetting characteristics on the surface. The mechanism of bendotaxis is shown in Figure 14iv. Here, two deformable walls of a flexible channel are clamped on one end, while the other ends are free. Two configurations are possible depending on the wetting character of the liquid droplet, as shown in Figure 14iv(a), while the resulting transport is depicted in Figure 14iv(b). For a wetting liquid, the walls are deflected inward, and the bending is stronger toward the open end than the clamped end. Due to this nonuniform bending, a pressure difference develops on the two sides of the liquid droplet, as shown in Figure 14iv(a). This difference creates a net pressure gradient toward the free ends. From scaling arguments, it was shown that for small droplet size, this pressure gradient takes the form[193]

$$\frac{\partial P}{\partial x} \sim \frac{L^2 {\gamma_{lg}}^2 \cos^2\theta(\Delta X)}{H_0^3 B} \tag{25}$$

where $B$ is the bending stiffness of the wall per unit width, $L$ the length of the formed channel, $\Delta X$ the initial droplet length along the direction of motion, $H_0$ the separation between the walls, $\gamma_{lg}$ the liquid surface tension, and $\theta$ the sessile droplet contact angle. The phenomena are similar even for nonwetting droplets, although the wall-bendings are on the opposite side, as shown in Figure 14iv(a). In short, during bendotaxis, the liquid droplet always moves toward the free end. More details about elastocapillary-based liquid transport on flexible membranes and capillary tubes can be found elsewhere.[194]

Soft surfaces are generally prepared on PDMS or similar types of polymeric substrates. These surfaces have standardized fabrication processes and are often biocompatible. Although soft polymers, like PDMS, are standard in classical flow-through microfluidics, their usage in open-surface microfluidics is limited because of several reasons. One major problem faced in wettability engineering on PDMS is the tendency of hydrophobic recovery of a superhydrophilic surface; after being created using plasma etching, such surfaces tend to revert back to their thermodynamically favorable hydrophobic state.[195] Another problem with PDMS arises from its variation of wetting behavior with the contact duration with water and the associated change in the speed of the advancing and receding liquid fronts.[196] It was also reported in the literature that the advancing and receding contact angles are highly sensitive to the casting protocol of PDMS and the extent of pretreatment. These problems are detrimental to attaining repeatability and reproducibility of droplet-transport on PDMS-based surface-microfluidic platforms. On thermal applications, soft surfaces do enjoy a few specific advantages like low thermal conductivity and low nucleation density, favoring their applications in thermal insulations, retarding condensation from humid air, or even delaying freezing.[197] However, ensuring adequate durability and the integration of the soft surface with the base substrate under adverse thermal conditions are challenging.

**3.2.6. Three-Dimensional Transport Configurations.** In all previous sections, liquid transport occurred on a plane. However, there exist situations where it may be required to transport droplets in 3D. Ghosh et al.[33] showed that a wettability confined superhydrophilic track on a flexible surface may be tilted out of plane to move liquid up the incline. This was further extended by Megaridis et al.[91] to generate 3-D liquid transport on open surface microfluidic platforms. Figure 15i(a−d) shows sequential snapshots of 3D liquid transport on such a curved track laid on a flexible polyethylene terephthalate (PET) film, which is arranged in a "highway overpass" design over a separate straight track (green-dyed liquid). This three-dimensional transport arrangement offers the possibility of laying interwoven complex circuits of open microfluidic channels passing over others without fluid contact, thus minimizing the chances of cross-contamination of the liquids.

Apart from the foregoing example, other modes of 3D liquid transport are, in general, possible mostly in porous materials with controlled wettability. As explained earlier, the liquid motion on a porous material is mainly governed by the wicking process, which allows the liquid to spread in all directions. By controlling the local wettability of the material, it is possible to control and manipulate liquid on thin porous substrates. The first concept of such a 3D paper-based microfluidic device was proposed by Ge et al. through the concept of paper origami.[198] Origami is a folding technique by which one can create complex 2D structures by folding a flat paper. As shown in Figure 15ii, sequentially folding the different tabs (filter, waste, and reagent) makes it possible to move liquids in 3D. In the origami process, liquid permeates through different planes when one folds and brings one surface close to the other. Although the process is simple, low-cost, and used by many researchers,[199] it requires manual intervention. Figure 15iii shows a 3D device built using plastic, filter papers, and adhesive tapes. Here, an adhesive double-layered tape was used as a spacer between two filter papers. The through-hole in the adhesive tape allowed the liquid to pass through from one filter paper to another. The other


https://doi.org/10.1021/acs.chemrev.2c00045
Chem. Rev. 2022, 122, 16752−16801

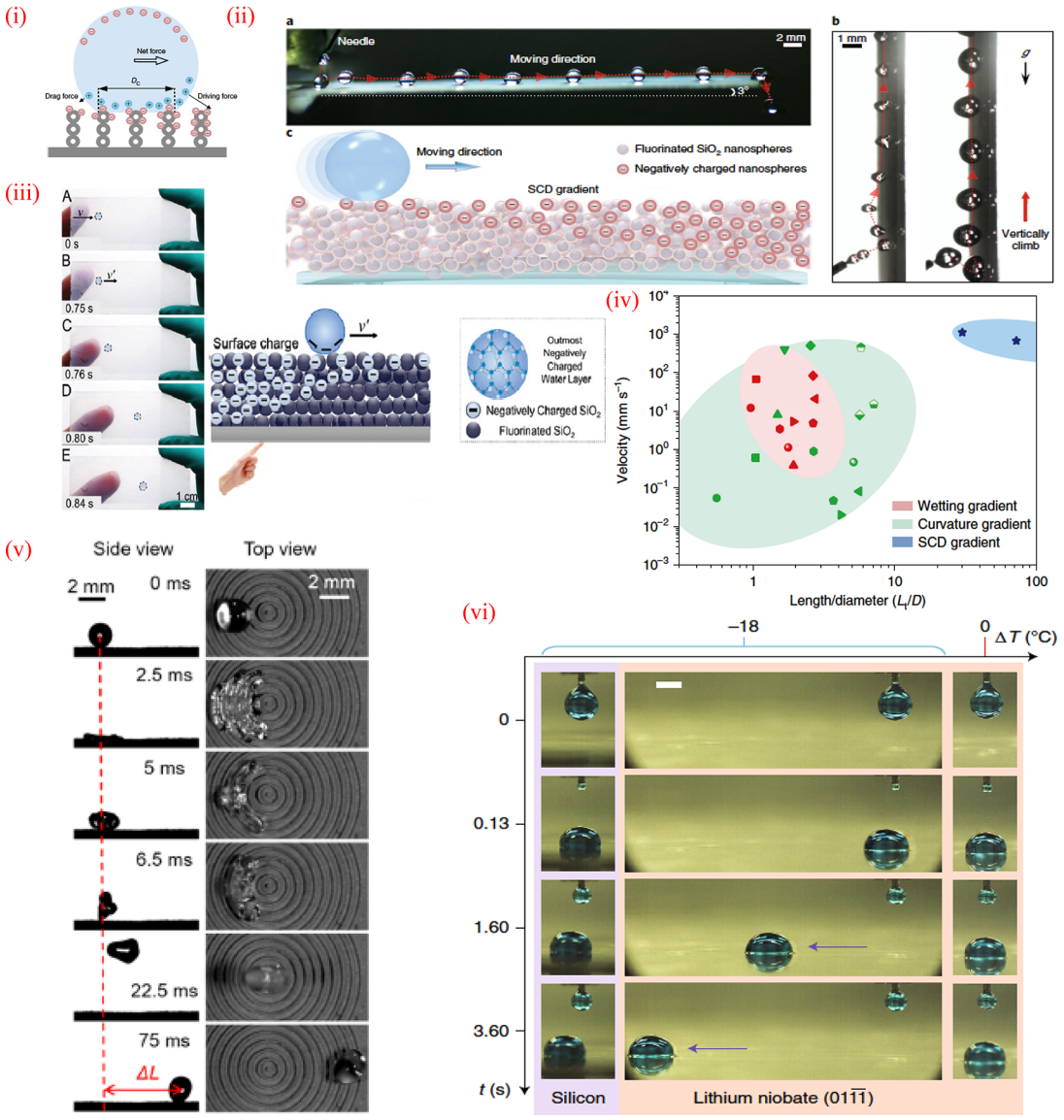


**Figure 16.** Noncategorized approaches of inducing droplet transport: (i) Mechanism on a surface charge density (SCD) surface. Adapted with permission from ref 206. Copyright 2019 Springer Nature. (ii) Schematic of SCD gradient transport (c) and experimental evidence (a,b) of droplet motion. Adapted with permission from ref 206. Copyright 2019 Springer Nature. (iii) Fluid transport mechanism due to electrostatic repulsive force created by finger touch. Adapted with permission from ref 207. Copyright 2020 Royal Society of Chemistry. (iv) Map of transport velocity vs length scale achieved by different mechanisms. Adapted with permission from ref 206. Copyright 2019 Springer Nature. (v) Directional transport on a spirally grooved surface after orthogonal droplet impact. Adapted with permission from ref 208. Copyright 2020 American Chemical Society. (vi) Thermal energy-driven movement of a cold droplet on a room-temperature lithium niobate substrate (scale bar denotes 2 mm). Adapted with permission from ref 210. Copyright 2021 Springer Nature.

common approach of transporting liquids in 3D is cutting and sealing porous papers to create 3D assemblies.[200]

Recently, Chatterjee et al.[34] demonstrated three different ways of manipulating liquids in 3D on a high-density, thin paper towel (HDPT). The paper towel was spray-coated with a superhydrophobic nanocomposite ($TiO_2$ + perchloro-alkyl methacrylate copolymer) and then selectively rendered superhydrophilic by exposing portions of the substrate to UV radiation through a photomask. Figure 15iv, case I shows a design where the top surface of the paper was rendered all superhydrophobic and a superhydrophilic, wettability confined wedge track was formed via selective UV exposure on the bottom surface through a photomask. A water droplet dispensed on the top surface permeated through the paper when the Laplace pressure ($p_d$) within the droplet exceeded the breakthrough pressure of the paper.[201] Once the breakthrough pressure was reached, the liquid permeated to the bottom side and spread directionally only on the superhydrophilic wedge track from the narrow to the wider end due to the Laplace pressure gradient (Figure 15iv and ref 33). Once the liquid builds up on the wedge track on the bottom surface, a backpressure ($p_b$) builds up due to the curvature of the pendant liquid on the track. The net pressure difference ($p_d - p_b$) drives the liquid from the top to the bottom surface of the HDPT (see Figure 15v), which can be estimated from Darcy's law; see Chatterjee et al., ref 34. With sustained deposition of liquid on the top surface and vertical permeation, the wedge track pumps the liquid horizontally and drips from the other end, as shown in Figure 15iv. In case II of the same figure, the superhydrophilic wedge track was laid on the top surface, and a circular


https://doi.org/10.1021/acs.chemrev.2c00045
Chem. Rev. 2022, 122, 16752−16801

superhydrophilic reservoir was patterned at the bottom surface (under the wide end of the track over it). The superhydrophilic reservoir at the top and the bottom were perfectly aligned. This configuration allowed the liquid to first transport horizontally on the top surface and then permeate at the end of the track through the superhydrophilic reservoir. In case III of Figure 15iv, two identical and perfectly aligned superhydrophilic wedge tracks were laid on the top and the bottom surfaces of the HDPT. In this configuration, the liquid was transported horizontally on both top and bottom as a film and then dripped from the bottom reservoir at right. Often 2D paper-based devices suffer from inadequate separation from the sample storage, transport, and sensing areas, leading to contamination and poor detection. To address such complicating issues, multilayering the paper-based design, with liquid transport in the third dimension, has emerged as a viable option. Punjiya et al.[202] proposed a 3D device with an analyte reservoir, as shown in Figure 15vi. Using a laser, they carved the analyte reservoir on a folded paper architecture and laid the liquid flow path.

A salient advantage of 3D transport, manipulation, and control of liquid droplets on and through substrates lies in leveraging the additional dimensionality of the transport direction to attain more functionality for a given chip configuration. This attribute is useful for a number of different applications. For example, targeted drug delivery to a wound from the outer surface of a bandage may be achieved through a combination of capillary-driven transport and imbibition of liquids.[203] Similar 3D transport may find several other applications, like sweat sampling and biomarker monitoring and point-of-care diagnostic applications, which are further discussed in section 4. Because most such flows occur in porous substrates, one has to pay attention to avoid liquid flow path blockage from contaminants or solid contents in the liquid. Also, the residual liquid retention inside the porous substrate may significantly alter the liquid transport throughput in these 3D substrates. Another challenge faced in such transport is the time-dependent variation of liquid perfusion rates in porous media due to swelling of the fibers (in the porous media), saturation of the substrate (by the liquid), and the variation of the evaporation pull (of the liquid) with progressive wetting of the substrate.[204] The good news is that new techniques are being developed to ameliorate this problem; for example, creating osmotic pressure difference across the porous medium by using hydrogel pads has been shown to drive stable and predictable transport over a wide range of operating conditions.[205]

Over the past three decades, researchers have demonstrated passive directional transport of various liquids on open surfaces. These works have primarily focused on surface fabrications, identifying new methods of liquid transport, and exploring new fluid physics. However, many challenges remain to be addressed. For example, fabrication of durable surfaces using green technologies has emerged as a new requirement for industry, while breakthroughs are still awaited in the domain of pumpless transport of low surface-tension and highly viscous liquids.

### 3.3. Other Approaches of Inducing Droplet Transport

Apart from the conventional liquid transport technique on the surfaces mentioned earlier, there are a few nonconventional methods of liquid transport, which are either particular to the conditions applied or have limited applications. In general, these nonconventional techniques are not generic and cannot be easily applied to any type of surface/liquid combination.

Sun et al.[206] demonstrated a novel approach to create surface charge density (SCD) on a superamphiphobic surface, which they made by coating $SiO_2$ nanospheres on a glass substrate and then used 1*H*,1*H*,2*H*,2*H*-perfluorooctyltrichlorosilane (PFOTS) to hydrophobize it. The resulting surface featured stacked-nanosphere pillars (Figure 16i). By impacting water droplets on such a surface, they demonstrated a method of creating SCD on it and showed that droplet transport could be controlled by manipulating the SCD, as shown in Figure 16ii. Experimentally, they showed that the SCD ($\rho_Q$) varies with Weber number ($We = \rho U^2 L/\gamma_{lg}$, with $\rho$ being the liquid density, $U$ the droplet velocity, and $L$ the droplet length scale) as $\rho Q \sim We^{0.74}$. The SCD created on the surface generates an unbalanced electric force that helps to propel each droplet on the surface. The driving force ($F_d$) on the droplet may be represented as

$$F_d = \frac{k_e \rho_{Qa} S_p Q_w}{r^2} \tag{26}$$

where $k_e$, $S_p$, $Q_w$, $\rho_{Qa}$, and $r$ denote the Coulomb constant, the projected surface of the pillar, polarization charge, surface charge density at the advancing side, and the distance between the pillar to the droplet, respectively. Upon several simplifications, one may write,[206]

$$F_d = \nabla \frac{{k_e}^2}{r^4} (\varepsilon_r - 1) \varepsilon_0 {\rho_{Qa}}^2 {S_p}^2 \cos\theta \tag{27}$$

where $\theta$, $\varepsilon_r$, and $\varepsilon_0$ are the angle between the horizontal component and the direction of electric force, relative dielectric constant of the droplet, and electric permittivity in vacuum, respectively. During the motion of the droplet, the restraining force can be expressed as

$$F_r = \nabla \frac{{k_e}^2}{r^4} (\varepsilon_r - 1) \varepsilon_0 {\rho_{Qr}}^2 {S_p}^2 \cos\theta \tag{28}$$

where $\rho_{Qr}$ is the surface charge density on the receding side of the droplet. The velocity scale can be obtained from the forces as $U \sim (\varepsilon_r - 1)\ \varepsilon_0 k$, where $k$ is the surface charge density gradient. Thus, the velocity of the droplet can be controlled by the charge density distribution of the surface. Using this approach, Sun et al.[206] demonstrated droplet motion on different types of substrates placed in different orientations. They highlighted that the "*droplet can self-propel over virtually any long distance*" at high velocity. Recently, Li et al.[207] demonstrated droplet motion on a superhydrophobic surface using electrostatic repulsive forces. As shown in Figure 16iii, when the user brought a finger with negative surface charge close to the drop (the droplet and the substrate were also negatively charged), electrostatic repulsive force pushed the droplet away from the finger. Li et al. achieved a droplet velocity ~17 mm/s for a 2 $\mu$L droplet. In SCD, the droplet velocity was reported to be 1 order of magnitude higher than velocities attained with wetting gradient or curvature gradient surfaces reported earlier (see Figure 16iv). Although the SCD and electrostatic repulsive forces provide higher droplet mobility, the effectiveness of these methods decreases with increased relative humidity.

By creating circular groove arrays, Liu et al.[208] showed that an impacting droplet could be given a directional transport. By properly designing the grooved surface, as shown in Figure 16v, they showed that the droplet first spread, recoiled, and finally jumped off the surface, landing at a distant location after the impact. A similar concept of droplet vectoring was demonstrated earlier by Schutzius et al.[209] Tang et al.[210] demonstrated that


https://doi.org/10.1021/acs.chemrev.2c00045
Chem. Rev. 2022, 122, 16752−16801

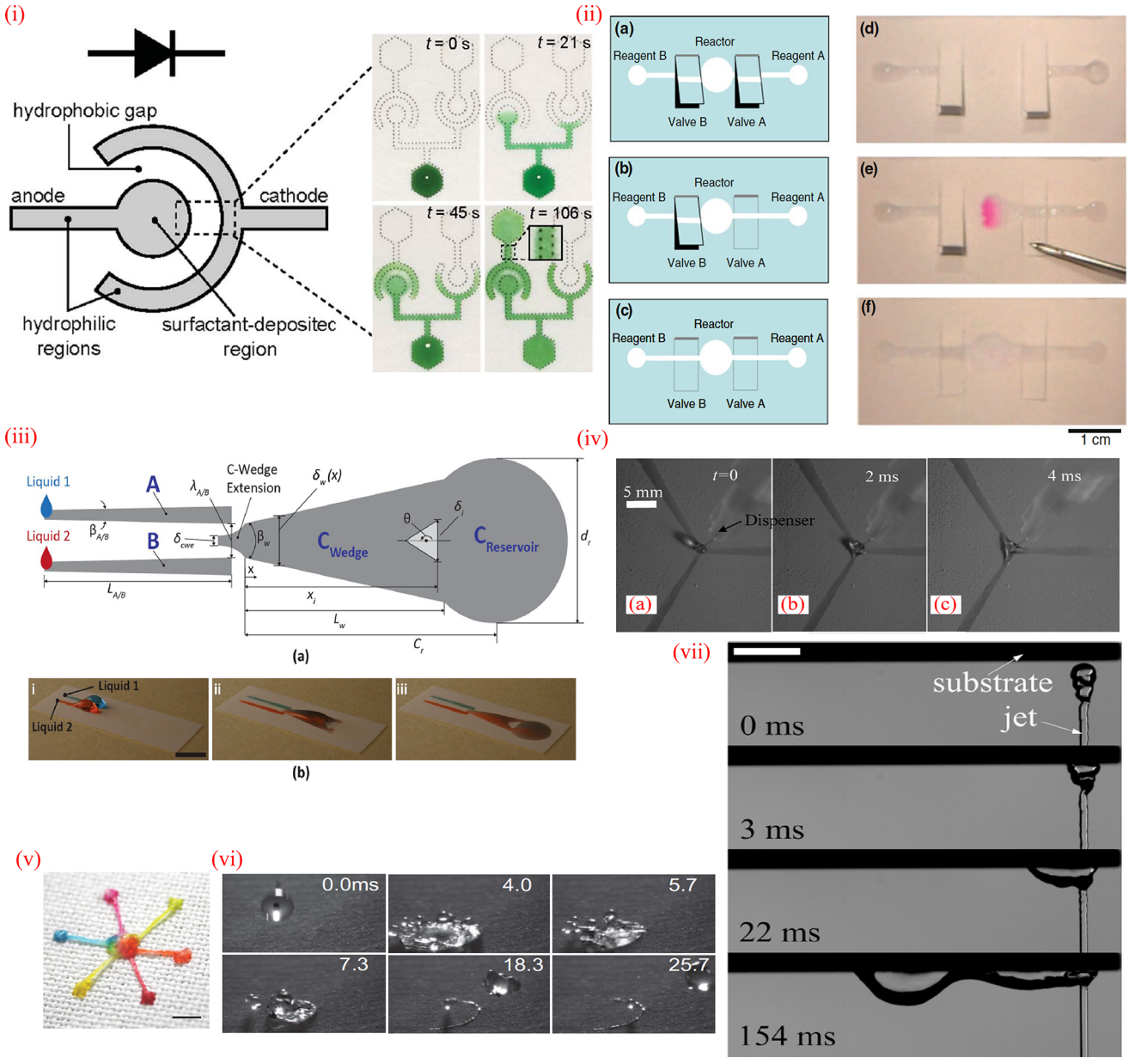


**Figure 17.** Complex liquid manipulation with engineered surfaces: (i) Schematic of a single-use fluidic diode (left). Time-sequenced photographs showing the fluid (green) wicking toward two parallel diodes. In the right diode, the liquid is stopped, whereas in the left diode the liquid passes across. Total time of wicking was ~100 s. Reproduced with permission from ref 212. Copyright 2012 Royal Society of Chemistry. (ii) (left) Design of simple paper-based microfluidic reactor consisting of two sample dosing sites, two valves, and one central reaction pad; (a−c) show the sequence of operations; (right) paper-based microfluidic reactor based on this design tested using acid−base neutralization reaction. (d) Phenolphthalein indicator solution was deposited onto the central reaction zone. (e) HCl and NaOH solutions were added in reagent zones A and B (labeled in (a−c), respectively. (f) NaOH solution was introduced first into the reaction zone to trigger color change. HCl solution was introduced subsequently into the reaction zone via valve A to neutralize NaOH in the reaction zone. Reproduced with permission from ref 132. Copyright 2012 American Institute of Physics. (iii) (top) Schematic of a self-driven surface micromixer (SDSM). (bottom) Representative images of (b(i)) before, (b(ii)) during, and (b(iii)) after mixing of two water droplets passively, initially dispensed on tracks A and B. Droplets were dyed for better visualization. Black scale bar denotes 1 cm. Reproduced with permission from ref 221. Copyright 2017 Springer Nature. (iv) SIMO multiplexing sequences of a water droplet splitting three and five ways, passively, on radially spaced diverging superhydrophilic tracks. Reproduced with permission from ref 33. Copyright 2014 Royal Society of Chemistry. (v) MISO configuration: multiple droplets (different color) are transported by Laplace pressure differences and merged at the center of a wettability patterned fabric. Reproduced with permission from ref 224. Copyright 2013 Royal Society of Chemistry. (vi) Time sequence of images showing a 2 mm droplet's orthogonal impact and vectoring on a hydrophilic arc surrounded by a superhydrophobic background. Adapted with permission from ref 209. Copyright 2014 Springer Nature. (vii) Snapshots with time stamps of a vertical capillary water jet impinging with ~2.9 m/s on a wettability patterned plate (horizontal), getting diverted laterally and transported along the length of a diverging superhydrophilic track (right to left). Gravity is acting downward. Track design similar to Figure 8ii is fabricated on an aluminum sample. Scale bar denotes 5 mm. Reproduced with permission from ref 229. Copyright 2016 Elsevier.

when a cold droplet (initially at 6 °C) touches a lubricated Si wafer, it stays still. However, the droplet moves, as shown in Figure 16vi, on a lubricated lithium niobate substrate. The motion of the droplet is thermal-energy driven. More discussion



https://doi.org/10.1021/acs.chemrev.2c00045
Chem. Rev. 2022, 122, 16752−16801

on energy source-driven motion is out of the scope of the current review as it requires external energy input.

### 3.4. Complex Microfluidic Tasks

A microfluidic system must facilitate liquid movement in ways that the chip can perform its intended task, e.g., mixing, splitting, metering, etc.[2,211] Wettability patterned passive surface microfluidics has been used to achieve such movement of liquids and to demonstrate multistep fluidic functionalities. An important roadblock in the development of next-generation microfluidic devices is minimizing the number of on-chip components required and the number of steps in operating the device. Passive surface microfluidics offers promise to mitigate some challenges in this area. In this section, we highlight some capabilities of complex manipulation of liquids, such as unidirectional transport (valves/diodes), mixing, multiplexing, separation of fluid-mixture constituents, and even passive transport against gravity.

**3.4.1. Fluidic Valving and Gating.** The ability to cease liquid flow and reinstate it on-demand is an essential requirement for numerous microfluidic tasks. Researchers have developed surface microfluidic valves and diodes to stop and trigger liquid flow as per process requirements. Chen et al.[212] designed a fluidic diode on a single sheet of paper to control the transport of liquid on wicking tracks. They fabricated trigger and delay valves and demonstrated complex manipulation of two different liquids using hydrophobic and hydrophilic wettability patterned surfaces. In their approach, the upstream end of the one-way valve was impregnated with a surfactant, which dissolved in the carrier fluid, allowing it to wick through a wettability barrier (a less wettable porous region) to the downstream side. When the fluid attempted to wick in the reverse direction, the carrier fluid could not reach the surfactant and hence could not overcome the wicking barrier (Figure 17i). Flexible-surface microfluidic substrates, like paper, polymer sheets, plastics, etc., offer innovative solutions for designing fluidic valves. Li et al.[213] created a valve on a wettability patterned cellulose substrate by cutting and folding a part of the liquid-carrying track, as shown in Figure 17ii. Unfolding the paper, i.e., bringing it level with the rest of the substrate, initiated liquid flow from one region to another. Multiple such valves/switches can be placed in series to facilitate reaction of two or more liquids. When a physical obstruction, such as an absorbent pad, is placed in a liquid-carrying hydrophilic channel that is surrounded by a hydrophobic background, restriction in liquid flow can be imposed. By strategically placing an absorbent pad on a hydrophilic channel and varying the physical dimensions of the pad, Toley et al.[214] delayed the liquid flow on a cellulose-based surface. They successfully reported delays ranging from 3 to 20 min by tuning the length and depth of the absorbent pad. Feng et al.[215] developed 3D printed capillary ratchets which mimicked the structure of *Araucaria* leaf: the structures featured transverse and longitudinal reentrant curvatures in the range of the capillary length of water. Wetting of liquids of high and low surface tensions on the 3D printed structures showed unidirectional motion in opposite directions; for example, ethanol ($\theta_{eq} \sim 21°$) showed liquid transport in the direction of rachet-tilting, while water ($\theta_{eq} \sim 59°$) exhibited the reverse trend. The micropatterned surface was also found to aid or oppose capillary rise of liquid through such structured surface.

While the foregoing discussion has covered liquid gating on a surface, unidirectional permeation of liquid droplet across a porous substrate also has practical relevance. Liquid-diode behavior across a permeable porous medium has been demonstrated by Wu et al.[216] and Mates et al.,[201] who demonstrated that when a nonwoven porous material was rendered hydrophobic on one side and hydrophilic on the other, a liquid droplet dispensed on the hydrophobic side could penetrate to the opposite side (provided the Laplace pressure inside the droplet exceeded the threshold penetration pressures of the porous structure), but a similar transport in the reverse direction (i.e., from the hydrophilic side to the hydrophobic one) was prevented. Widodo et al.[217] demonstrated similar directional penetration across cotton fabrics by spraying a commercially available hydrophobizing spray on one side and leveraging the intrinsic wettable nature of cotton on the other. Shou and Fan[218] proposed an all-hydrophilic fluid diode using porous materials having asymmetric pores. The anisotropy of the threshold penetration pressure from the two sides led to capillary flow in a chosen direction. The direction-dependent flow process and the breakthrough pressure can be explored experimentally and explained theoretically in terms of the Gibbs pinning criterion and re-entrant theory.[218]

**3.4.2. Mixing.** Surface microfluidic mixers have been developed by several research groups. These devices require power input and have appeared in terms of electrowetting on dielectric, magnetic, dielectrophoretic, surface acoustic, or thermocapillary designs.[219] A key criterion in designing microfluidic devices for POC solutions is to minimize off-chip components, thus facilitating ubiquitous use, especially for field deployment and healthcare in low-resource environments. Achieving efficient mixing without any external energy input is a severe challenge, and at the same time, a necessity when low cost is of the essence. While the literature is replete with wicking passive micromixers, there are few prior reports of Laplace pressure-driven surface micromixers with facile fabrication, minimal manufacturing cost, and operational complexity. The most common passive surface mixing approach is spot mixing, where a presuffused analyte is reacted with the deposited sample.[220] The mixing time scales are limited by diffusion, which is a very slow ~O(10s) process. Laplace pressure driven (LPD) mixing devices on wettability patterned substrates offer a promising way to improve the mixing time scales by 3 orders of magnitude ~O(100 $\mu$s).[221] Ghosh et al.[33] first proposed a wettability engineering approach to achieve LPD transport and demonstrated rapid mixing. Wettability patterns offer advantages on planar superhydrophobic patches and are analogous[222] to 3D obstacles in conventional closed-channel mixers, which explore chaotic mixing to improve overall mixing efficiency.[223] Morrissette et al.[221] developed a self-driven surface micromixer and investigated the effect of laying 2D hydrophobic patches on superhydrophilic tracks. They quantified the mixing index (MI) in several superhydrophobic islands configurations (e.g., shape, size, orientation). Depending upon the device, Morrissette et al.[221] achieved rapid (<0.5 s) mixing with moderate MI ~ 0.7 or relatively slower (>1 s) mixing with high MI ~ 0.9 (maximum achievable MI is 1). In certain designs, MI ~ 0.85 was achieved within 200 ms, which is an acceptable value for practical POC devices. Although wettability patterned surfaces have paved the platform for simple, passive micromixers, further research is needed to define the limitations and realize the full potential of this technique with respect to different applications. As an example, Figure 17iii demonstrates some design details in this context.

**3.4.3. Multiplexing.** Like mixing, multiplexing liquid into several quanta is an essential attribute required for several


https://doi.org/10.1021/acs.chemrev.2c00045
Chem. Rev. 2022, 122, 16752−16801

microfluidic tasks and has to be achieved passively. Based on specific requirements, multiplexing can be either single-input multiple-output (SIMO) or multiple-input single-output (MISO). For example, to perform multiple biomarker-based or repetitive diagnostics with a single drop of biological fluid (urine, etc.), SIMO is preferred. Wettability patterning has proven to be a powerful tool to achieve SIMO[33] and MISO[224] multiplexing. Parts iv and v of Figure 17 depict multiple superhydrophilic tracks passively transporting liquid. The number, precision, and resolution of multiplexing tracks is dependent on the fabrication technique used. More sophisticated micronano fabrication will yield higher-resolution multiplexing capabilities.

**3.4.4. Droplet Stopping/Restarting.** Droplet stopping and restarting are often needed for incubation and serial protocols of a microfluidic platform. Some methodologies that have shown promise here include the use of magnetorheological (MR) fluids and ferrofluids, which could serve as transporters or shuttle mechanism for delivery of the target droplet. Previous research on gradient surface (where droplet motion occurs spontaneously) has demonstrated that a uniform magnetic field could be used to alternately pin and/or release a ferrofluid droplet on the surface.[225] In this way, the magnetic field can act as a switch, while the transport is effected by capillary force. Other possible mechanisms for restarting droplet motion include droplet coalescence with a volatile actuating fluid; for example, Sellier et al.[226] observed that the coalescence of an ethanol−water droplet pair (or toluene−silicone oil) on a confined HPL track resulted in the spontaneous motion of a water droplet over a distance of ∼10 mm. In some cases, it was reported that the actuated droplet could even be displaced without apparent contact with the actuating droplet, suggesting the importance of the vapor phase interaction and the apparent need for a highly volatile liquid to be used in the actuating droplet. The motion only lasted for a short duration though and also worked best on highly wettable substrates with low CAH.[226]

Other potential methods of initiating droplet motion include the use of sound waves, mechanical/forced vibration, and pulsed air.[102,158] Lv and Hao,[158] for example, found that using an oscillator frequency of 80 Hz and amplitude of 0.75 mm, a 20 $\mu$L water droplet could travel a few millimeters on a hydrophobic surface featuring microstructure with spatial gradient. Shastry et al.[102] also showed that water droplets could be propelled down a topographical gradient using mechanical vibrational energy with a travel distance of 6.2 mm. It is currently unclear, however, if these methods could be easily coupled with existing lab-on-a-chip applications as they also require external energy input.

**3.4.5. Droplet/Jet Impact.** Impacting drops or liquid jets are pervasive in applications ranging from cooling electronics[227] to lab-on-chip.[209] Controlling the impact behavior of $\mu$-volume droplets on wettability patterned surfaces has value for some surface microfluidic applications.[228] Utilizing the competition between inertial and surface tension forces, microvolume droplets were bounced nonorthogonally off flat substrates upon orthogonal impact.[209] Figure 17vi documents the sequence of droplet impact on a semicircular hydrophilic arc followed by oblique ejection. Upon impact, the droplet was seen to first spread radially over the surface, flattening out, and reaching a maximum diameter and then contracting in a receding stage. Due to the significant difference in contact angles on the hydrophilic−superhydrophobic anisotropic surface, a net horizontal component of surface tension force develops during the receding phase of the droplet, thus propelling it parallel (to the right in Figure 17vi) to the substrate upon recoil. Such passive droplet vectoring capabilities have ramifications in surface microfluidic and liquid-based soft templating applications. Koukoravas et al.[229] diverted a capillary jet that impacted orthogonally upon a diverging superhydrophilic track surrounded by a superhydrophilic background and demonstrated spatially selective cooling of hot surfaces (Figure 17vii). The volume of the liquid propelled forward can be tuned based on the geometry of the wettability pattern and the jet-impact velocity. Impact-based droplet/jet manipulation on wettability patterned tracks may invigorate researchers' interest in designing novel, facile, easy-to-use POC, and enhanced cooling devices.

While a detailed discussion on droplet and jet impact on wettability engineered surfaces is beyond the scope of this review, the reader could refer to pertinent works in the literature on a few salient attributes: (i) comprehensive review of droplet impact on solid surfaces of different wettabilities[230] and heated walls,[231] (ii) the role of wettability on impact dynamics,[232] (iii) transient heat transfer behavior during droplet impact on hydrophobic, superhydrophobic, and biphobic (hydrophobic spots in a superhydrophobic background) surfaces,[233] (iii) Leidenfrost behavior droplet impact regimes on wettability engineered surfaces,[234,235] (iv) self-propelled droplets on Leidenfrost surfaces,[236] (v) jet impingement on wettability engineered surfaces,[237] and (vi) heat transfer during jet impingement on wettability patterned surfaces.[233,238]

The foregoing section discussed the feasibility of achieving a diverse range of complex microfluidic tasks on open surfaces. While each such task needs special features of wettability engineering on the pertinent substrate, integration of more than one tasks on a single chip is yet to be realized on a given surface. Moreover, certain challenges still exist in the performance metrics of these complex tasks. For example, in the configuration of metered dispensing on wettability patterned surface,[33] the sacrificial volume on the wettable tracks may lead to volumetric errors. The precision of these complex microfluidic tasks also depends strongly on the liquid surface tension and the substrate wettability. Therefore, the repeatability and reproducibility of such complex microfluidic tasks may largely vary with the local and temporal fluctuation in the concentration and pH of the biochemical samples, local surface blemishes, and the extent of on-chip chemical reaction in a biofluid application. Furthermore, other challenges have also emerged, viz., (i) droplet motion stopping/restarting, (ii) droplet splitting in open-channel flows, (iii) combining different actuation mechanisms, (iv) facilitating greater travel distances, (v) creating more durable gradient designs, and (vi) improved droplet modeling. With respect to the first challenge, it is still difficult except in special cases with active actuations (i.e., magnetic fields and ferrofluids,[225] electrowetting,[39] etc.) to pin a droplet while in motion on a gradient and/or restart a droplet's motion once stopped. The delivery of multiple droplets of the same volume from a single deposited sample has also long been a source of great interest in lab-on-a-chip applications. Considerable focus has already been devoted to this topic but challenges still remain. Methods of splitting droplets in closed channel flows (i.e., Y-shaped and L-shaped junctions) do not always extend to open-channel microfluidic flows, although some progress has been made.[33,176,239]

A frontier issue that has remained unaddressed is wettability tuning on-the-go. For instance, questions that have dawned in the surface microfluidics community are: Can the wettability be


https://doi.org/10.1021/acs.chemrev.2c00045
Chem. Rev. 2022, 122, 16752−16801

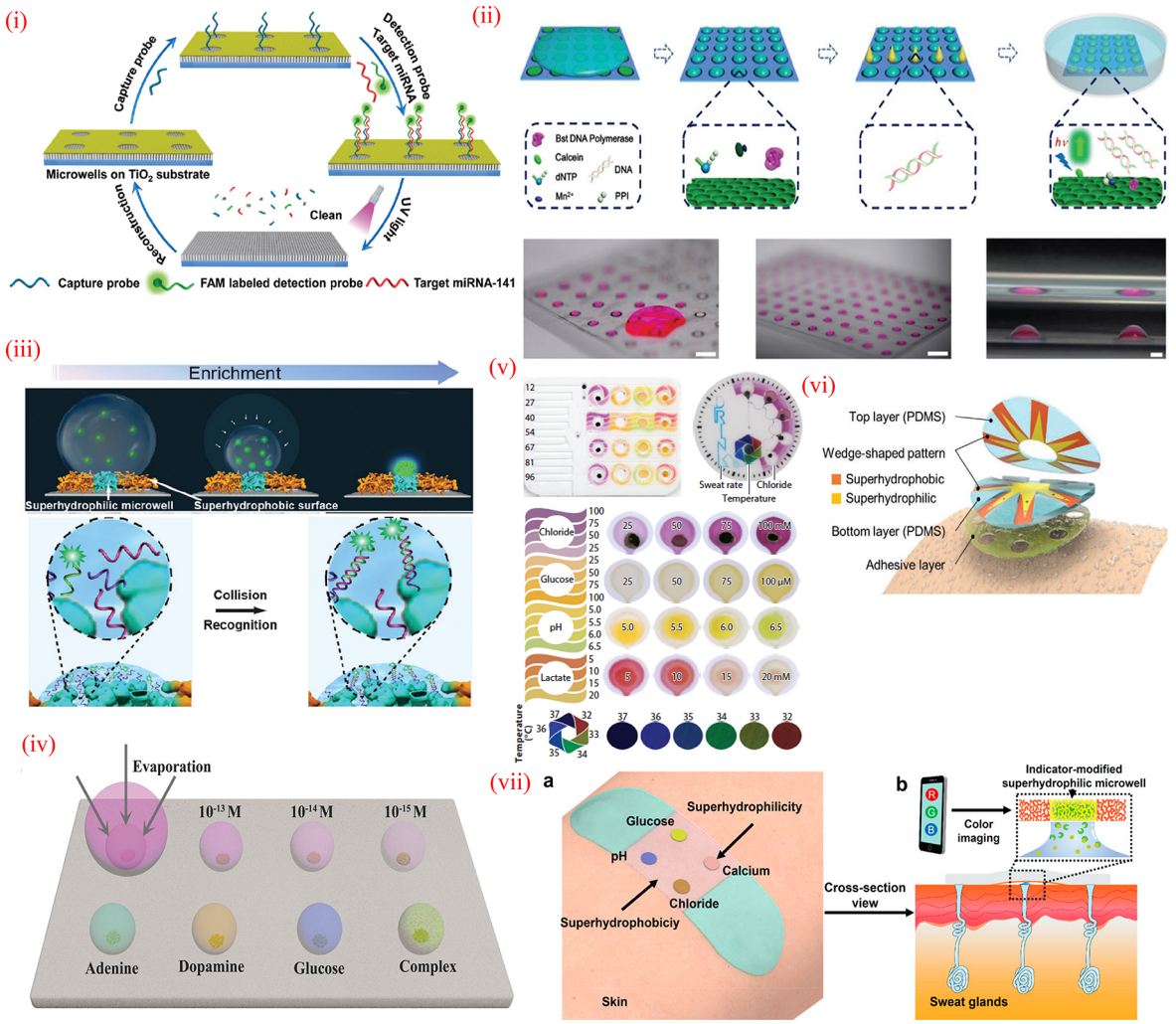


**Figure 18.** Wettability modified sensors. (i) Schematic of a wettable patterned biochip for miRNA detection. Adapted with permission from ref 245. Copyright 2018 Elsevier. (ii) Wettability patterned nitrocellulose substrate for nucleic acid detection. Scale bars are 1 cm, 1 cm, and 1 mm, respectively. Adapted with permission from ref 246. Copyright 2018 Royal Society of Chemistry. (iii) Evaporation-based DNA detection. Adapted with permission from ref 247. Copyright 2015 Wiley. (iv) SERS-based detection of ultralow concentration of adenine, dopamine, glucose, and rhodamine. Adapted with permission from ref 248. Copyright 2015 Wiley. (v) Biomarker detection in sweat. Adapted with permission from ref 249. Copyright 2018 American Association for the Advancement of Science. (vi) Schematic of sweat analysis patch. Adapted with permission from ref 250. Copyright 2021 Wiley. (vii) Schematic of sweat analysis flexible band. Adapted with permission from ref 251. Copyright 2019 American Chemical Society.

tuned selectively during the transport? Can microfluidic circuits be tuned after the fabrication via mechanical strain, applied surface vibration, selective illumination, etc.? Most current techniques generate continuous streams of droplets. Can single droplets be generated on-demand on a surface? Future lab-on-a-chip applications will, in every likelihood, need to address these lingering questions. Even under ideal circumstances (i.e., CAH $\sim 1°$) there is an upper constraint regarding how far a droplet can travel on a single topographical gradient or how small a droplet can be moved on an open surface without pinning. To facilitate even longer travel distances, it is likely that combinatory approaches would be needed. A few possibilities include droplet coalescence, shape-based gradients, and temperature (Marangoni) gradients. Functionally graded materials with multiple-deposited layers, for example, could also be used to create a topographical nonuniformity with gravitational assist.

## 4. APPLICATIONS

The ease of liquid transport on open surfaces makes the approach useful for a wide range of applications, starting from lab-on-chip and POC medical diagnostics to heat transfer and water collection from the atmosphere. The various passive transport mechanisms described in the earlier sections are relatively new, and most are still in their exploratory phase. This section accentuates some existing applications of passive surface microfluidics and wettability patterned substrates, which play a vital role in different engineering and biological applications. Recent research focuses on the applications of wettability patterned surfaces in energy, water harvesting, low-cost point-of-care diagnostics, sensors, tissue engineering, cellular studies, etc., which are elaborated here.

### 4.1. Sensing

Due to the low-cost, environmental friendliness, and ease of fabrication, paper-based sensors have historically enjoyed the greatest preference of researchers. Many excellent review articles have been published on wettability modified materials deployed in sensors[240−242] and electronics.[243,244] Apart from paper, different polymers, silicon, and plastic surfaces are also used as sensor materials. Wettability modified or patterned surfaces are


https://doi.org/10.1021/acs.chemrev.2c00045
Chem. Rev. 2022, 122, 16752−16801

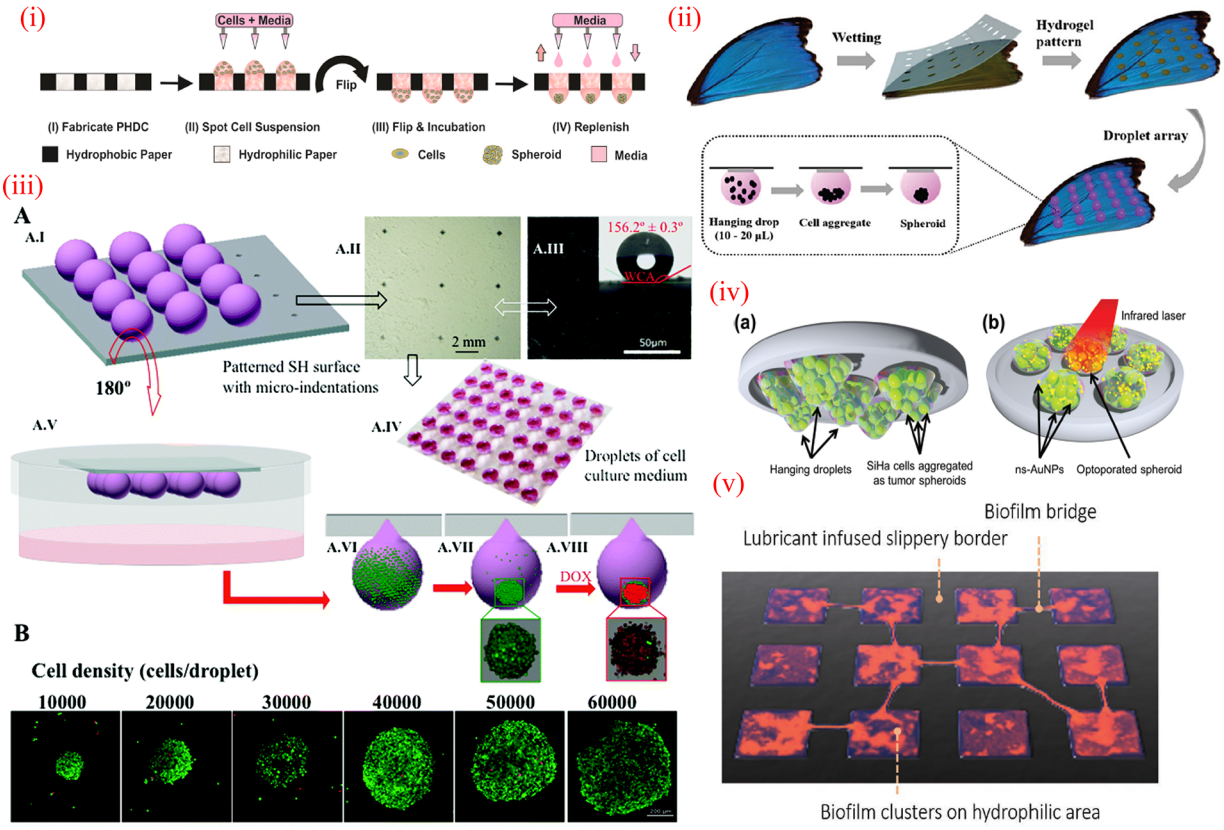


**Figure 19.** Wettability modified surfaces for cellular studies. (i) Paper-based surface used to create hanging droplet spheroids. Due to the porous structure, replenishment of the medium is possible. Adapted with permission from ref 255. Copyright 2018 American Chemical Society. (ii) 3D cell culture in hydrogel-based hanging droplet method. Adapted with permission from ref 256. Copyright 2019 American Chemical Society. (iii) Microindentation on a superhydrophobic polystyrene surface used as a platform for droplet spheroids. Adapted with permission from ref 257. Copyright 2015 Royal Society of Chemistry. (iv) Cancer spheroid creation through hanging droplet method. The drug delivery was performed by a laser-induced optoporation technique. Adapted with permission from ref 258. Copyright 2021 Royal Society of Chemistry. (v) Biofilm formation on SLIPS. Adapted with permission from ref 259. Copyright 2019 Wiley.

sometimes used along with standard detection techniques like spectroscopy, surface-enhanced raman scattering (SERS), etc., to create microfluidic sensors.

Liquid dispensed on a wettability patterned surface prefers to move toward the (super)hydrophilic areas, which is used in miRNA detection on a renewable, wettable, patterned glass-based biochip, as shown in Figure 18i.[245] The design claims high detection limits by using fluorescent molecules and UV light-based cleaning of the organic material from the surface after usage, making this device sensitive and economical. Inspired by the Stenocara beetle, Chi et al.[246] demonstrated a nucleic acid detection technique on a nitrocellulose substrate (see Figure 18ii). By implementing loop-mediated isothermal amplification (LAMP), they could detect DNA efficiently. As mentioned earlier, the wettability patterned surfaces helped in pinning the droplet at a particular location. With time, the analyte concentration increased due to evaporation of the fluid. The enrichment of the analyte concentration caused stronger fluorescent signals,[247] as shown in Figure 18iii for DNA detection. A similar approach was used by Song et al.[248] for detecting ultralow concentrations of adenine, dopamine, glucose, and rhodamine. They created superhydrophilic areas on a superhydrophobic background and deposited Au areoles on the superhydrophilic areas to facilitate SERS-based detection technique with enhanced sensitivity (see Figure 18iv). The droplet-based detection on wettability patterned surfaces is beneficial, as these droplets also work as microreactors. It is interesting to note that the reaction rate increases inside these microreactors due to evaporation and thermal Marangoni flows. It is also possible to detect several analytes from the deposition patterns after complete evaporation of the droplet.

Figure 18v shows colorimetric detection of different biomarkers like glucose, lactate, chloride, and pH in sweat. Using a low-cost, passive microfluidic technique, Choi et al.[249] showed that the enzymatic reactions could efficiently detect different biomarkers in sweat. As shown in Figure 18v, their device also has a "thermochromic liquid crystal temperature sensor" and a microfluidic channel to measure body temperature and overall sweat loss, respectively. Son et al.[250] demonstrated sweat collection and analysis using an epidermal sweat collection patch, as shown schematically in Figure 18vi, where the multilayered device has an adhesive bottom layer to adhere to the skin. The other two PDMS layers were wettability patterned to facilitate sweat transport. Wedge-shaped superhydrophilic patterns were created on both PDMS layers to passively transport the fluid toward the center of the device. Son et al. demonstrated the detection of lactate and glucose by connecting the sweat collection patch with an electronic sensor that could measure the impedance/current. A flexible superwettable band for sweat analysis was developed by He et al.[251] (Figure 18vii). Using a cellphone-assisted detection technique, they demonstrated that their wearable devices could detect pH, glucose,


https://doi.org/10.1021/acs.chemrev.2c00045
Chem. Rev. 2022, 122, 16752−16801

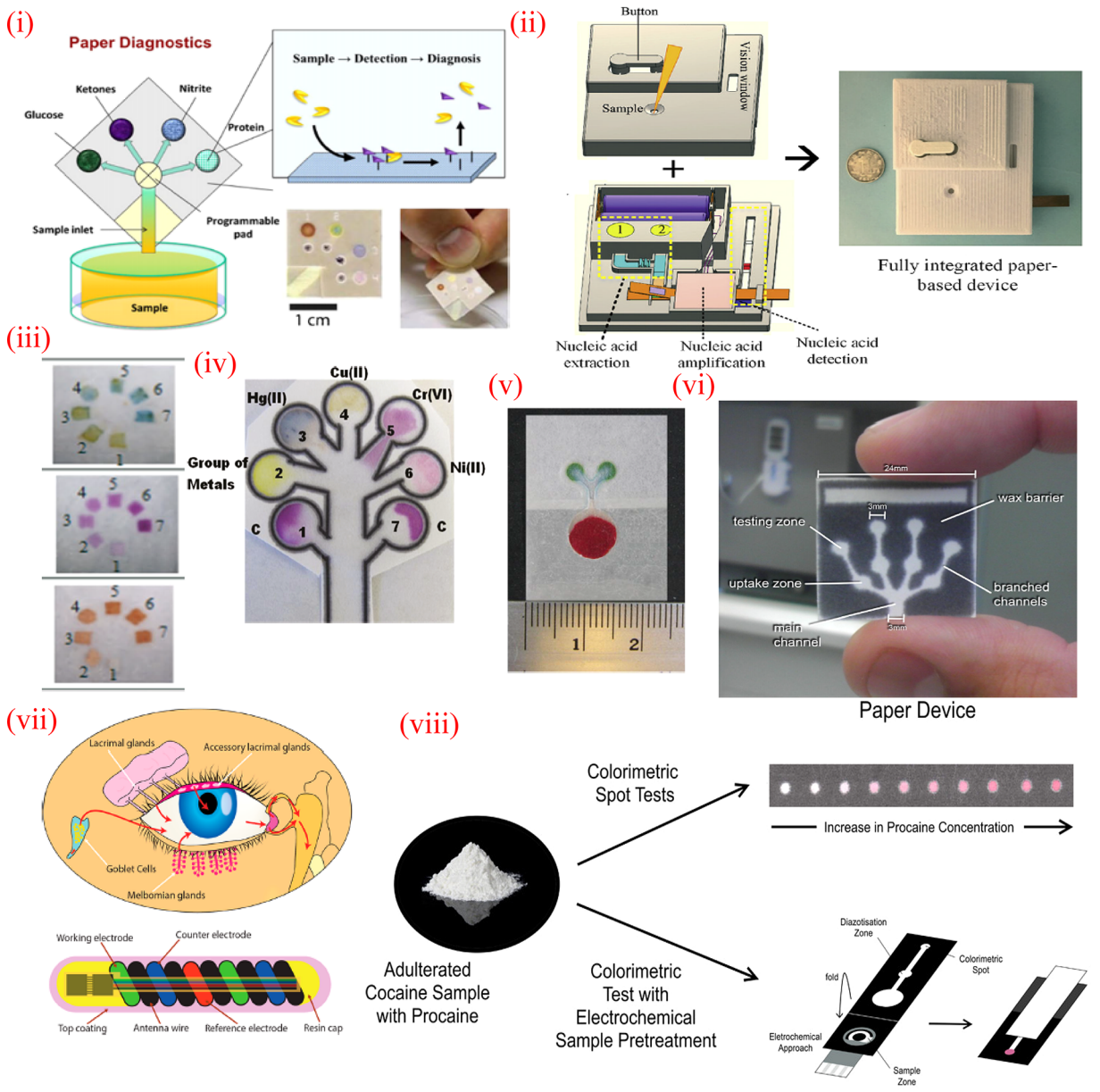


**Figure 20.** Point-of-care diagnostic devices using microfluidic techniques. (i) Paper-based device for urine sample analysis. Adapted with permission from ref 261. Copyright 2013 Springer Nature. (ii) Paper-based nucleic acid testing and amplification device. Adapted with permission from ref 265. Copyright 2017 Royal Society of Chemistry. (iii) Images of "double inlet" $\mu$CAD after detection of protein, nitrite, and glucose, respectively. Adapted with permission from ref 266. Copyright 2015 Springer. (iv) Detection of individual heavy metals from a water sample using a multiplexed bioactive paper sensor. Aqueous samples containing Hg(II), Cu(II), Cr(VI), and Ni(II) were added to the circular regions of assay zones with markers for identifying individual elements. Reproduced with permission from ref 270. Copyright 2011 American Chemical Society. (v) Micro PAD ($\mu$PAD) applied with whole blood concurrence with plasma separation and determination of human serum protein. Adapted with permission from ref 271. Copyright 2018 Royal Society of Chemistry. (vi) $\mu$PAD for nitrite detection in saliva, showing the hydrophilic main channel, branched channels, uptake zones, and testing zones surrounded by hydrophobic wax layer. Reproduced with permission from ref 272. Copyright 2014 Elsevier. (vii) Schematic showing tear production and a device to measure glucose concentration in tears. Adapted with permission from ref 274. Copyright 2018 American Chemical Society. (viii) Paper-based device to detect procaine from cocaine samples. Adapted with permission from ref 275. Copyright 2018 American Chemical Society.

calcium, and chloride in sweat. Similarly, Koh et al.[252] fabricated a wearable stretchable microfluidic device for chemical analysis of sweat. Their design consisted of four paper-based colorimetric chemical assays, which required microliter volumes of sweat to determine the concentrations of lactate, glucose, creatinine, pH, and chloride ions. A similar design for sweat analysis using textile-based fluid handling and an optical detection system has been reported by Curto et al.[253]

## 4.2. Cell Culturing

Wettability confined liquids can also serve for cell culturing on open microfluidic platforms. Recently, it has been shown that 3D cell culture has a better in vivo resemblance than the classical 2D Petri dish based cell culture.[254] Among the various available strategies, 3D cell culture on a hanging drop is the most popular approach. The stages of creating hanging drops on a paper-based wettability patterned substrate[255] are shown in Figure 19i. In the


https://doi.org/10.1021/acs.chemrev.2c00045
Chem. Rev. 2022, 122, 16752−16801

hanging drop method, the cells proliferate and, due to gravity, settle at the tip of the drop, as shown in Figure 19i. Thus, a cell spheroid forms after the aggregation. Shao et al.[256] reported a hydrogel-based hanging droplet strategy using butterfly wings as a biotemplate (see Figure 19ii). A superhydrophobic polystyrene surface with a microindentation was used by Neto et al.[257] as a hanging droplet platform for L929 (fibroblast-like cells). Their approach reduced the cytotoxicity, as they did not make any chemical modifications of the surface. The surface with the hanging drops was kept over the cell medium to minimize evaporative losses, as shown in Figure 19iii. They also performed a drug screening test by adding an anticancer drug on the droplet spheroid. Gupta et al.[258] created a cancer cell spheroid using the hanging drop method, shown in Figure 19iv, and also demonstrated a laser-based drug delivery method using gold nanoparticles on the cell spheroid. Using a nanosecond pulsed laser, they demonstrated an optoporation technique to deliver propidium iodide into a human cervical cancer cell spheroid. Lei et al.[259] studied the behavior of *Pseudomonas aeruginosa* on SLIPS, as shown in Figure 19v; they observed a biofilm cluster on the superhydrophilic part of the patterned SLIPS, whereas, for the superhydrophobic areas, formation of thin bridges were observed.

### 4.3. Point-of-Care (POC) Diagnostics

The role of microfluidics in biomedical research has been summarized by Sackman et al.,[7] who highlighted the gradually growing importance of microfluidics in applications outside engineering, as based on publications in biology and medicine journals. The efficacy of microfluidic systems in rapid, inexpensive, and straightforward POC medical tests for the developing world is well-established.[260] The use of capillary-driven transport in POC devices relying on paper surfaces started from the seminal work of Martinez et al.,[130] who showed simultaneous detection of glucose and protein in microliter volumes of urine. Such multiplexed assays on paper-based surfaces with minimal sample volumes have also been demonstrated using wax (hydrophobic) and paper (hydrophilic) for patterning. Novak et al.[261] reviewed the different low-cost techniques for POC identifications of infectious and noncommunicable diseases. One such device for urine analysis is shown in Figure 20i. The use of everyday materials, like wax and paper, further reduced the fabrication time.[262] Exhaustive reviews of such paper-based devices for POC diagnostics exist in the literature.[263,264] A paper-based nucleic acid testing (NAT) device is shown in Figure 20ii; it contains a reagent storage facility and is capable of nucleic acid extraction, amplification, and testing.[265] The wicking capillary transport for multiplex assays has also been extended to cloth-based analytical devices (CAD). Colorimetric detection of bovine serum albumin (BSA) in artificial urine was shown by Nilghaz et al.[266] on CAD-fabricated wax patterning on cotton cloth, as shown in Figure 20iii. Similar immunoassay has also been demonstrated on silk yarns with predefined flow pathways using a hydrophobic barrier.[267] In brief, biodetection is being practiced on any kind of fibrous surface ranging from cellulosic paper to cotton and polyester threads.

Paper-based microfluidic devices have also been used to create networks with multiple inlets to perform automatic sequential delivery of multiple fluids to a detection zone.[268,269] Such designs facilitated convergence of reagents from multiple inlets to common detection regions that can be further utilized to drive multistep sequences autonomously. Hossain and Brennan reported heavy metal detection from water using similar paper-based devices (see Figure 20iv).[270] Other potential applications of liquid transport on paper-based microfluidic devices include blood plasma separation (Figure 20v) from whole blood[271] and controlled biofluid removal, such as skin surfaces experiencing heavy perspiration.[68] Bhakta et al.[272] developed a micro paper analytic device (PAD) to identify and quantify the levels of nitrite in saliva, which has been proposed as a potential marker of periodontitis. Their device comprised of a hydrophilic main channel, branched channels, uptake zones, and testing zones surrounded by the hydrophobic wax barrier, as shown in Figure 20vi. They claimed that this device might also be used to quantify nitrite in food and water samples (nitrates in food and water are linked with N-nitroso compounds that have known carcinogenicity[273]) and other biological samples. Kownacka et al.[274] developed a device to measure the glucose from tears, as shown in Figure 20vii, and reported good correlation between the measured glucose level in tears and that present in blood. Silva et al.[275] developed a low-cost, sensitive, and easy-to-use colorimetric device for identifying "procaine in seized cocaine samples." They increased the efficiency of the device by adding an electrochemical pretreatment unit (see Figure 20viii).

A recent upsurge in attempts of leveraging open-surface fluidic transport for Covid-19 detection offers testimony for the technology to address mainstream microfluidic challenges. Covid-19 is extremely contagious due to its transmission via airborne droplets. The virulent characteristics of the SARS-CoV-2 virus are observed as in any RNA-based virus, which can quickly replicate viral proteins in the host cell, thus making detection at the early stages of infection very crucial.[276] Nucleic acid testing for detection of SARS-CoV-2, which has been globally adopted as the primary method to trace the presence of the virus in the swab samples, has several different variants, e.g., reverse transcription-polymerase chain reaction (RT-PCR), loop-mediated isothermal amplification (LAMP) and clustered regularly interspaced short palindromic repeats (CRISPR). Recently, Bhalla et al.[277] reviewed the challenges and opportunities of biosensors applicable for Covid-19.

The Covid-19 pandemic has led to the widespread use of personal protective equipment (PPE), such as face masks, hand sanitizers, etc., to reduce the risk of virus spreading. Mahaparta et al. presented a review of surface engineering pertinent for developing antibacterial and antiviral PPE.[278] Sarkar et al. developed an extremely low-cost do-it-yourself face mask that used a combination of a hydrophilic cotton layer sandwiched between a pair of hydrophobic, polypropylene nonwoven fabric layers.[279] The triple-layer assembly harnessed the principle of "liquid diode";[201] the combination of the hydrophobic innermost (facing the user) and hydrophilic middle layer blocks the carry-over of droplet to the outermost hydrophobic layer even during heavy exhalation, sneezing, or coughing by the user. The outermost hydrophobic layer, on the other hand, offers a large enough transport barrier to prevent inward permeation of any airborne droplet as the mask user inhales.

The point-of-care diagnostic strategies mentioned earlier became a very powerful tool during the recent Covid-19 pandemic. With a high number of cases globally during the different waves, it became critical to eliminate the need for highly skilled professionals and complicated protocols for diagnosis of this deadly infection. Cost-effective POC tests became an innovative way to address this challenge.[280] Shen et al.[281] showed an integrated microfluidic system using RT-PCR,


https://doi.org/10.1021/acs.chemrev.2c00045
Chem. Rev. 2022, 122, 16752−16801

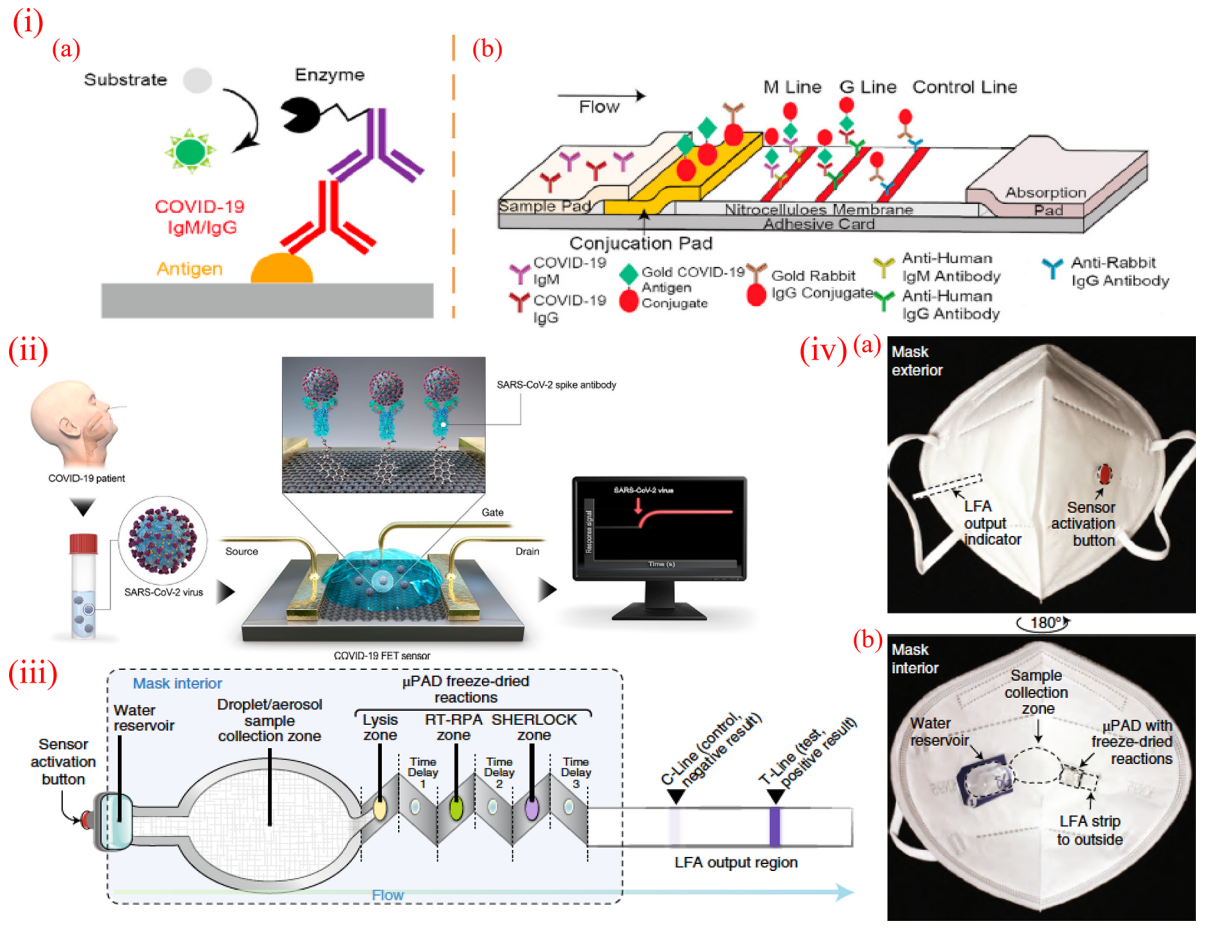


**Figure 21.** Covid-19 detection strategies using fluidic approaches. (i) Covid-19 testing using (a) ELISA and (b) lateral flow assay. Adapted with permission from ref 284. Copyright 2021 Elsevier. (ii) Schematic for Covid-19 infection detection starting from biological sample collection. Field effect transistor (FET) biosensors are used on a graphene-based sensing system. Adapted with permission from ref 285. Copyright 2020 American Chemical Society. (iii) Schematic of sensor component used in a face mask. Water flows through wicking material from the water reservoir, moving viral particles collected from the wearer's respiration from the sample collection zone to downstream freeze-dried reactions integrated into a μPAD device. The final output is visualized by an LFA (lateral flow assay) strip that is passed externally through the mask. Adapted with permission from ref 286. Copyright 2021 Springer Nature. (iv) Photographs of SARS-CoV-2 sensor integrated into a facemask. Adapted with permission from ref 286. Copyright 2021 Springer Nature.

which allows automatic virus purification and lysis, improving upon the detection time, which is very critical during a pandemic. Such incremental advancements to existing techniques to make faster and easier detection and develop systems integrated with smartphones have been summarized by Song et al.[282] One interesting variation in this regard was reported by Liu et al.,[283] who incorporated centrifugal microfluidics with fluorescent immunoassay for detecting viral antigens of SARS-Cov-2. The entire process described there took only 15 min from sample loading to single readout, making it an ideal POC platform for Covid-19 detection. Along with POC devices, there exist biosensor-based detection systems, which are well tabulated by Song et al.[282] The conventional testing of Covid-19 by using ELISA and lateral flow assay is shown in Figure 21i.[284] Seo et al.[285] developed an aqueous-solution-gated field effect transistor (FET) biosensors for SARS-CoV-2 detection (Figure 21ii), where a droplet of phosphate-buffered saline deposited on the substrate led to efficient gating effect so that the FET system could detect SARS-CoV-2. Nguyen et al.[286] developed a facemask with embedded sensor for rapid detection (Figure 21iii). The sensor had a collection zone, a liquid wicking path, freeze-dried reaction zones, and a lateral flow assay (LFA) strip for SARS-CoV-2 detection. The integrated sensor on the facemask is shown in Figure 21iv. The sensor can be operated by using an activation switch, as shown in Figure 21iv(a). The interior wall of the facemask and all components of the sensor are shown in Figure 21iv(b). Recent advances in preserving the conformational epitopes of SARS-CoV-2 antigens immobilized through metal−organic framework encapsulation on microtiter plate have opened the possibility of room-temperature storage for enzyme-linked immunoassay for detection and quantification of antibodies against SARS-CoV-2.[287] Such technology can be implemented on open-surface microfluidic platforms for pathogen detection as well. Due to the high demand for rapid Covid-19 detection, a few products have been commercialized that employ end-to-end "all in one" fully automated technology, which is simpler, easier to handle, and affordable: Cepheid,[288] GeneXpert,[289] and Bosch.[290]

The Covid-19 crisis has underscored the importance of developing user-friendly, highly scalable, open-surface microfluidic detection systems that may be extended to rapid detection of not just the novel corona virus but also other similar deadly viruses, as and when needed, with minimum design modification. Keeping in mind the pervasiveness,


https://doi.org/10.1021/acs.chemrev.2c00045
Chem. Rev. 2022, 122, 16752−16801

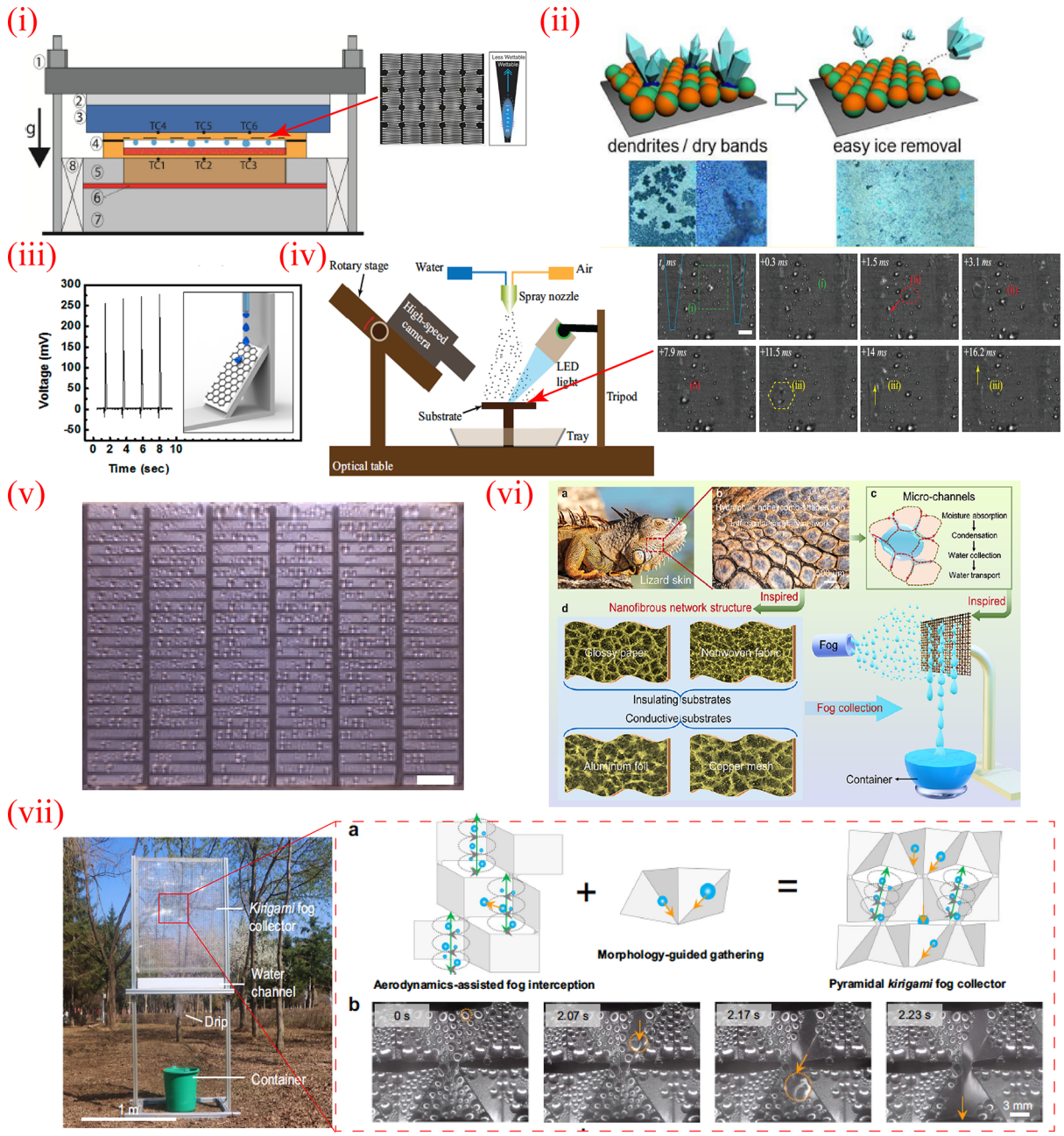


**Figure 22.** Applications of surface wettability patterns in energy and water conservation. (i) Vapor chamber with wettability patterned condenser. Adapted with permission from ref 292. Copyright 2022 ASME. (ii) Janus surface for anti-icing. Adapted with permission from ref 293. Copyright 2016 American Chemical Society. (iii) Nanoenergy generation from the motion of droplet on an inclined graphene surface. Adapted with permission from ref 294. Copyright 2016 American Chemical Society. (iv) Droplet transport during spray impact on a horizontal surface. Reproduced with permission from ref 296. Copyright 2021 MDPI under the terms of the Creative Commons CC BY license [https://creativecommons.org/licenses/]. (v) Dropwise condensation of water vapor on a wettability patterned aluminum surface bearing staggered interdigitated superhydrophilic tracks that facilitate passive drainage of the condensate from the vertically placed substrate. Scale bar is 10 mm. Adapted with permission from ref 299. Copyright 2016 Elsevier. (vi) Fog harvesting using bioinspired nanofibrous substrate. Adapted with permission from ref 301. Copyright 2021 American Chemical Society. (vii) Kirigami-based fog collector for water harvesting from the atmosphere. The Kirigami structures and the droplet transport on them are shown in a and b. Adapted with permission from ref 302. Copyright 2021 Springer Nature.

enormity, and rapidly mutating traits of the SARS-CoV2 virus, the salient needs for mass deployment of low-cost surface microfluidic devices in the events of a future pandemic (or the future waves of the current one) may be subsumed into the following design criteria: (i) ability to multiplex (to detect the right variant and eliminate false detection), (ii) ease of upgrading the protocol (to accommodate new strains), (iii) amenability to mass fabrication, (iv) ease in operation (for use en masse), and (v) ability of rapid detection.

### 4.4. Energy and Water Conservation

Capillary-driven liquid transport on open surfaces at miniature length scales has strong relevance in heat and mass transfer, as well as in energy and water harvesting applications. For example, intense heat removal from small spaces has always been a concern in electronics cooling and thermal management.


https://doi.org/10.1021/acs.chemrev.2c00045
Chem. Rev. 2022, 122, 16752−16801

Koukoravas et al.[229,291] used rapid liquid transport along a long, wettable wedge-shaped track on a superhydrophobic background to cool a heated metal plate using an orthogonal jet. They leveraged capillary-driven, directional transport of the cooling liquid over the hot spot, which was offset from the impact point. They demonstrated that such a strategy allowed for a higher heat-to-flow rate ratio as compared to other competing technologies.[229] They further found that the cooling performance improved when the track width was below the capillary length of the working fluid.[291] Cooling performance was also found to improve by using multiple, narrow tracks laid over the heated domain.[291]

Damoulakis et al.[292] developed a novel wettability patterned vapor chamber and used it as a thermal diode. The schematic of the device is shown in Figure 22i. The inset shows the wettability patterned condenser surface, where combinations of superhydrophilic wedges and bands were used to transport the liquid back to the wick-lined evaporator (bottom of the vapor chamber). Kirillova et al.[293] created heterogeneous wettable surfaces by coating Janus particles with both hydrophilic and hydrophobic sides. They demonstrated experimentally that the dendritic growth of ice formation and the surrounding dry area helps in removing the ice from the surface efficiently. The process is shown in Figure 22ii. Kwak et al.[294] reported that graphene-PTFE surfaces generate electricity due to the "triboelectrification-induced pseudocapacitance" on the graphene, when a droplet moves over the surface. Electricity generation from the continuous motion of the water droplet is shown in Figure 22iii. A wettability patterned design for heat transfer applications using an array of spray nozzles was patented by Joshi and Dede.[295] Thomas et al.[296] demonstrated the transport of liquid on a horizontal, wettability patterned metal surface upon high-speed spray impact (see schematic in Figure 22iv). The metal surface featured several superhydrophilic wedge tracks laid on a superhydrophobic background. The time lapse images in the inset of Figure 22iv show the coalescence of the droplets after impact and final drainage through the superhydrophilic tracks. Capillary-driven transport has also been deployed for energy-related applications, like liquid water transport in fuel cells and oil recovery.[297]

Wettability patterns have been used to collect water from the atmosphere.[298] At high heat fluxes, the condensed droplets coalesce, eventually forming a continuous film on the surface. Ghosh et al.[78] used an interdigitated arrangement of wedge-shaped wettability confined tracks on a less wettable background of mirror-finish aluminum to enhance the removal of condensate from a condenser plate via the Laplace pressure gradient. The design was further improved by Mahapatra et al.,[299] where the wedge tracks had a staggered arrangement shown in Figure 22v; this design led to ∼31% improvement in water collection under a typical atmospheric water-harvesting scenario. Wang et al.[300] deployed an array of wedge-shaped superhydrophilic bumps (∼30−120 $\mu$m long, wedge tip angle ∼10°) on a tilted, superhydrophobic surface, leveraging the Laplace pressure gradient and gravity to generate out-of-the-plane droplet jumping to promote condensate removal, thereby showing significant improvement in water collection from humid air via dropwise condensation. Inspired by the lizard skin structure, Zhang et al.[301] created a fog harvesting system, shown in Figure 22vi, and reported by 200% superior water collection in their nanofibrous surfaces compared to plain surfaces. Li et al.[302] reported a 3D folded structure, known as Kirigami, to create a fog harvesting system, as shown in Figure 22vii. They created "cubic structure" and "square facets" from aluminum-coated PET sheets to collect the harvested fog droplets and transport them toward the collector. Their 3D pyramidal-structured mesh collected almost twice as much water as compared to the traditional Raschel mesh.

## 5. DISCUSSION: ROADBLOCKS AND FUTURE DIRECTIONS

### 5.1. Current Challenges

Exploration of passive surface microfluidics has been initiated in recent years. Although this domain offers significant promise in novel $\mu$-volume liquid manipulation techniques, as with any newly introduced technology, there remain several challenges that must be mitigated if the technology is to find widespread use. In this review article, we have tried to identify some of these challenges, with the intent to help the community overcome the associated roadblocks.

Grassroot-level end users of most microfluidic technologies are not fluid physicists or micronano fabrication experts; rather, the majority of practitioners consists of clinicians, public health officials, aid workers, or NGO volunteers. With this condition in mind, the biggest challenge is to develop passive surface microfluidic technology to be as facile as possible, minimizing expert intervention. Integrating the fluid transport and biochemistry with appropriate detection and reporting mechanisms is a key to develop user-friendly POC testing devices. End-user cost is another important parameter because the demand for such technology is expected to be pervasive in developing countries. On the technical front, more experiments and fundamental studies need to be performed by the microfluidics research community to identify the operating limits of the passive liquid manipulation mechanisms in terms of flow rates, fluid transport distance, material compatibility, especially at the device level. Proof of concept in academic laboratories is a good first step for any emerging technology, but the real value is realized when the technology is validated (i.e., it proves equivalent or better than an existing protocol) and emerges as a commercially viable product with tangible consequences for the common good. Thus, the technology should cater to applications with high product volume and low product cost.

One of the principal concerns in the commercial viability of a single-use surface microfluidics-based POC diagnostic device is its shelf life and its packaging and storage requirements. The shelf life of an open-surface platform depends on various factors, including the environmental temperature, relative humidity, dust exposure, and even the presence of light. It has been often observed that the wettability characteristics of the material change in the presence of sunlight or UV radiation and also under thermal cycling. Thus, special care needs to be taken for proper storage and handling of the devices if they are photosensitive. From the fluid-dynamic perspective, achieving throughput and transport speed and the flexibility of real-time control that are comparable to those in traditional flow-through microfluidics has remained one of the principal challenges of passive, surface microfluidic transport. Additional challenges arise, as pointed out in section 3.1, due to losses of sample liquid from the surface through evaporative loss and residual liquid volume (left behind on the substrate). Except for cases where these otherwise negative attributes are actually leveraged to achieve the target functionality,[74,204] meticulous efforts are warranted to minimize such interfering effects. Also, as pointed


https://doi.org/10.1021/acs.chemrev.2c00045
Chem. Rev. 2022, 122, 16752−16801

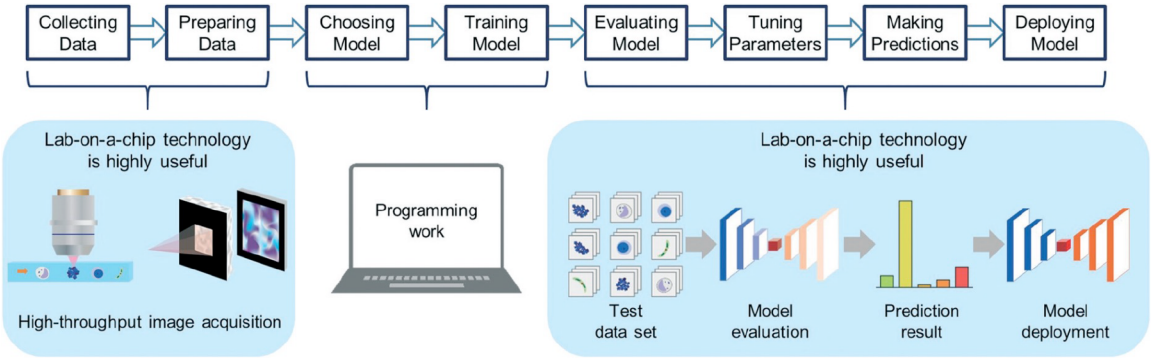


**Figure 23.** AI-based development in microfluidics. AI technology plays an important role in the first and final steps of lab-on-a-chip development. The excellent synergy between AI and lab-on-a-chip technology helps both the construction and implementation of AI in a large-scale, cost-effective, high-throughput, automated, and multiplexed manner. Adapted with permission from ref 317. Copyright 2020 Royal Society of Chemistry.

out in section 3.3, achieving a satisfactory level of pumpless, surface microfluidic transport while handling highly wetting/low surface tension and highly viscous liquids has remained an elusive target (it is very hard to create repellency to the former, or to achieve high transport speeds with the latter).

Furthermore, there are challenges in integrating the liquid handling platforms with the sensing elements of a POC device. Besides, distributed deployment of such low-cost biosensors for point-of-care use warrants for synergistic integration of the sensors with wireless and mobile communication and Internet of Things (IoT) equipment and protocols.[303]

## 5.2. Future Directions

Development of surface microfluidics has, so far, leveraged the art and science of surface chemistry, material science, micro- and nanofabrication, interfacial flow dynamics, biotechnology, and medical science and technology. As such, interdisciplinary research collaboration involving mechanical engineers, bioengineers, chemical engineers, clinicians, etc., is a necessary and important step to address the gamut of applications in the lab-on-chip domain. The simplicity and universal material compatibility (as long as wettability contrast is achieved) of open-surface, passive microfluidic platforms open boundaries beyond lab-on-chip applications (e.g., heat transfer and thermal management, jet cooling, personal hygiene products, water management in fuel cells, etc.). Additional research must also be conducted in other domains, e.g., anti-icing,[304] liquid transport on and through porous materials,[34,305] power electronics and battery cooling,[291] targeted drug delivery through porous surfaces, etc., that can benefit from open-surface microfluidics. It is worth noting that a widespread use of surface-microfluidic platforms would eventually require interfacing with conventional flow-through microfluidics as and when required. This would allow harnessing the best features of both approaches, thus enabling the design of versatile microfluidic platforms that have better compatibility with different laboratory equipment and are capable of tackling more complex problems.

While each of these related fields is still emerging in terms of unraveling newer attributes, particularly at the crossroads of each domain, two emerging areas that are worth special mention are the increasing role of Artificial Intelligence (AI) and Machine Learning (ML) in design of wettability engineering and the development of smart wearable technology. A third, highly promising yet elusive so far, field of microfluidics is the development of organ-on-a chip (OOC) platform based on open-surface microfluidics.

### 5.2.1. Role of AI/ML in Design of Wettability Patterns.

Artificial intelligence has been a booming field over the past few years, impacting all industry sectors. Although the concept existed from 1955,[306] the ease of gathering and processing data has made this emerging area accessible and a powerful tool to accelerate the innovation ecosystem in all sectors, including automotive, healthcare, defense, energy, etc. The paradigm shift of AI from theory in the computer science discipline to practical adaptation in real-life applications is critical for advancing these applications. The different subgroups of AI, like machine learning, deep learning, or general adversarial networks (GANs), etc., include effective generation as well as analysis of high amounts of data.[307−309] The end-to-end workflow in this area involves (a) data collection, (b) data preparation, (c) model choice, (d) model training, (e) model accuracy evaluation, (f) tuning of hyperparameters to improve accuracy, and (g) model utilization for prediction purposes.[310] The starting point of this workflow, namely, the data collection and data preparation, is both laborious but also critical, as it serves as the foundation and backbone of a strong predictive model. The data can be in the form of images or signals generated from either physical experiments or simulations.

In the microfluidics community, this emerging technology has started showing interesting benefits and fruitful results. A key component of work in this area harnesses insights in materials science and AI-based algorithms that can help significantly in rapid predictions based on material databases.[311,312] Physics-based modeling has its own challenges for predicting material properties, processing times, wear losses, etc., because of the inherent nonlinearity and lack of established models, whereas ML algorithms like Gaussian process regression (GPR), gradient boosting regression (GBR), support vector machine (SVM), and random forest provide predictions with accuracy of 95% or higher[313−315] in a short time.

AI methodologies have the potential to impact open-surface microfluidics technology as well. Gukeh et al.[316] extended the approach of leveraging ML algorithms for predicting UV exposure time to attain specific desired wettability, which was quantified using contact angle. This approach turned out to be beneficial for quick identification of the UV exposure time of a $TiO_2$-containing surface coating to achieve the desired wettability used as a driving mechanism for liquid transport over open surfaces.[33]

The healthcare industry with point-of-care diagnostics applications may reap immense benefits using the AI technology, specifically using high-throughput imaging as a


https://doi.org/10.1021/acs.chemrev.2c00045
Chem. Rev. 2022, 122, 16752−16801

tool to acquire data. Isokazi et al.[317] provided an excellent review on such usage where AI-boosted diagnosis using X-ray, CT, as well as MRI imaging[318] helped to address problems in DNA/RNA sequencing[319] and accurate identification of objects in samples.[320] The workflow used in all of these applications is explained in Figure 23. Although usage of deep learning architecture has recently gained traction in closed-channel microfluidics[321] and in complex systems, like organ-on-chip,[322] its use in open-surface microfluidics has remained, by and large, unexplored to date. Nonetheless, the recent works mentioned above give an inkling of the potential to formulate design criteria, flow behavior, and features of open-surface microfluidic devices using machine learning and deep learning approaches.

**5.2.2. Smart Wearable Technology.** Recent widespread development of wireless sensor networks (WSN) and Internet of Things (IoT) connected devices has unleashed a paradigm in microfluidics-based wearable biosensing, where the microfluidic device may be integrated with cloths or other functional gear worn by the user. Several such wearable biosensors use open-surface microfluidics and are being developed for monitoring physiological parameters, pathogen detection, or even for controlled drug dosing. Using wearable sensors helps gather the patient's physiological cues on a real-time basis, which can be a vital component of continuous health monitoring systems. In recent years, wearable technology has been developed for monitoring various critical and chronic diseases, for example, cardiopulmonary and vascular monitoring, glucose monitoring,[323] advanced wound monitoring,[324] etc. With the rising demand for decentralized medical care and the advancement of wearable technology, developing intelligent devices that can monitor and take part in critical health care is required. Design and fabrication of intelligent wearable biosensors with wettability patterned porous or nonporous surfaces is an upcoming research area for developing efficient, durable, and corrosion-resistant devices. Researchers are also interested in developing self-powered wearable sensors for health monitoring.[325] Li et al.[326] developed wettability modified wearable sensors to perform efficiently in a wet and corrosive environment. Although some studies exist on wettability modified sensors, dynamically adjustable surfaces with tunable wettability remain sparse.[327]

Continuous monitoring of glucose level in blood is essential for diabetes management. Smart self-monitoring devices can continuously check the glucose level and control the insulin level by pumping insulin.[323] These glucose-monitoring devices assess the patient's health condition, send the required data to the health care provider and take the necessary actions through actuating the on-board insulin pump. Another interesting development is the noninvasive continuous monitoring of ocular glucose level. A few companies are developing contact lenses that have built-in sensors for detecting and transmitting glucose levels via an IoT-based protocol.[323] Different other biomarkers can also be detected and diagnosed remotely with the advancement of intelligent sensors. Similar types of smart devices are also required for neurological function monitoring, particularly for postoperative management. Continuous monitoring devices are also required to diagnose mental health, Parkinson's and Alzheimer's diseases, chronic wound treatments, etc. Being new, the field of surface microfluidics is nascently evolving and the jury is still out on its long-term value.

**5.2.3. Organ on a Chip.** The World Economic Forum recognized organ-on-a-chip (OOC) as one of the "Top Ten Emerging Technologies".[328] The OOC platform mimics the environment of the physiological organs of humans or other living animals. Understanding human physiology and the interactions of the lower-level systems like cells, tissues, and genes are important in medicine, toxicology, drug development, and delivery, etc. The most reliable approach to understanding the functionality and mechanisms of the body could be the in vivo studies; however, due to the low throughput, high costs, and stringent clinical and ethical clearance issues, in vitro studies often offer viable alternatives, although at the cost of sacrificing the true ambience of biophysical parameters. The OOC platform provides an intermediate solution by mimicking the biophysical conditions on chip and allows one to conduct high-throughput clinical studies with great reliability before embarking on animal models. It is envisioned that the OOC platform will provide the necessary support for preclinical trials, faster drug development, and drug delivery trials and may replace the animal models in the future.[329]

Researchers have already developed OOC platforms for mimicking the functionalities of liver, kidney, lung, heart, intestine, etc., as reviewed in earlier publications.[329,330] Although this field has garnered a tremendous amount of research effort in the past 10 years and is progressing very fast, the development of multiorgan systems or human-on-a-chip still remains far away. Two major drawbacks of the existing effort are using photolithography-based fabrication approaches of classical microfluidic systems and the handling of PDMS. Further research is required to replace the classical flow-through microfluidics by open surface platforms to develop low-cost, mass customizable, reliable versions of OOC systems.[331]

## 6. CONCLUSIONS

This review has presented an update on passive open-surface microfluidics and its accelerating implementation on low-cost devices at the center of technological advancements in point-of-care diagnostics, environmental sensing, thermal management, and other related areas. The term passive has been used here to indicate the lack of external energy input and distinguish spontaneous self-driven transport from other active modes of transport. Different strategies of surface functionalization and the attributes of surface-microfluidic transport realized on the wettability engineered surfaces were discussed. Salient features, including the advantages and shortcomings of each approach of wettability engineering have been analyzed. It is worth noting that the requirements of durability of these surfaces differ from one application to another. For example, for a single-use POC application,[130] the surface functionalization should have a long shelf life, but during operation, it is only required that the surface functional groups do not wash out with the fluid shear while the device is in operation. Choice of the substrate material and the nature of surface functional groups in such applications is primarily driven by their cost and compatibility with the working fluid. On the contrary, for thermal applications, e.g., wettability engineered condensation surfaces,[299] or capillary wicking-based heat spreaders,[292] it is desirable that the substrate shows durability against thermal and fluidic cycling. Choice of the substrate and the wettability patterning strategy for such applications has a priority on durability over the cost aspect. It is interesting to observe from the literature that while many research groups in the field of surface microfluidics claim their methods to be facile and best suited for specific applications, a holistic picture of relative costs remains unclear. The cost of a surface microfluidic device should not just be estimated based on the raw materials (the substrates and the functionalizing


https://doi.org/10.1021/acs.chemrev.2c00045
Chem. Rev. 2022, 122, 16752−16801

chemicals) but also the upfront cost of the infrastructure involved in fabrication and usage. For example, a spray-coated nanocomposite surface[33] may involve more expensive chemicals than a micromachined surface,[107] but the latter entails deployment of highly capital-intensive microfabrication facilities. The target end-user cost would therefore strongly depend on the scalability of the wettability engineering process. A typical ballpark figure for the cost of a micropaper analytical device ($\mu$-PAD), which leverages 3D transport, is estimated to be less than 0.5 USD per device.[200] Therefore, a comprehensive survey on the relative cost of different surface fabrication strategies in terms of their performance and product durability is recommended as a future focus in this field.

The recent fundamental advances in surface microfluidics have not been accompanied yet by technological discovery with game-changing influence. However, the significant progress over the past two decades in the nanomaterials arena bears promise that microfluidic technologies will follow suit, eventually bearing fruit for low-resource environments where money, and more importantly, technical expertise, remain in sparse supply.

## ASSOCIATED CONTENT

### Special Issue Paper

This paper is an additional review for *Chem. Rev.***2022**, volume *122*, issue 7, "Microfluidics".

## AUTHOR INFORMATION


### Corresponding Author

**Constantine M. Megaridis** − *Department of Mechanical and Industrial Engineering, University of Illinois at Chicago, Chicago, Illinois 60607, United States;* orcid.org/0000-0002-6339-6933; Email: cmm@uic.edu

### Authors

**Pallab Sinha Mahapatra** − *Micro Nano Bio-Fluidics group, Department of Mechanical Engineering, Indian Institute of Technology Madras, Chennai 600036, India;* orcid.org/0000-0002-4073-9980

**Ranjan Ganguly** − *Department of Power Engineering, Jadavpur University, Kolkata 700098, India*

**Aritra Ghosh** − *Department of Mechanical and Industrial Engineering, University of Illinois at Chicago, Chicago, Illinois 60607, United States*

**Souvick Chatterjee** − *Department of Mechanical and Industrial Engineering, University of Illinois at Chicago, Chicago, Illinois 60607, United States*

**Sam Lowrey** − *Department of Physics, University of Otago, Dunedin 9016, New Zealand;* orcid.org/0000-0002-1019-4342

**Andrew D. Sommers** − *Department of Mechanical and Manufacturing Engineering, Miami University, Oxford, Ohio 45056, United States;* orcid.org/0000-0003-4365-0364

Complete contact information is available at: https://pubs.acs.org/10.1021/acs.chemrev.2c00045


### Author Contributions

CRediT: **Pallab Sinha Mahapatra** conceptualization, funding acquisition, writing-original draft, writing-review & editing; **Ranjan Ganguly** conceptualization, supervision, writing-original draft, writing-review & editing; **Aritra Ghosh** writing-original draft, writing-review & editing; **Souvick Chatterjee** writing-review & editing; **Sam Lowrey** writing-review & editing; **Andrew D. Sommers** writing-review & editing; **Constantine M. Megaridis** funding acquisition, supervision, writing-review & editing.

### Notes

The authors declare no competing financial interest.

### Biographies

Pallab Sinha Mahapatra is an assistant professor in the Department of Mechanical Engineering of the Indian Institute of Technology, Madras, India. He received his Ph.D. and B.E. degrees from the Department of Mechanical Engineering, Jadavpur University, in 2014 and 2007, respectively. He also held a postdoctoral research appointment at the University of Illinois at Chicago (UIC). His research includes interfacial flows, wettability engineering, collective dynamics, and energy systems.

Ranjan Ganguly is a professor in the Power Engineering Department of Jadavpur University (JU) and an adjunct professor in the Mechanical and Industrial Engineering Department of the University of Illinois at Chicago (UIC). He received his B.E. in Power Plant Engineering (1995) and M.E. in Heat Power specialization (2000) from JU. He received Ph.D. from UIC (2005) and had postdoctoral research stints at Universität Hannover, TU Darmstadt, Virginia Tech, and UIC. His primary research encompasses investigation of capillary-driven flow on surface microfluidic platforms, wettability engineering for sustainability, magnetic particle-based microfluidics, and thermodynamic analyses of energy systems.

Aritra Ghosh is a Senior Engineer at Lam Research, California, USA. He received his Ph.D. in Mechanical Engineering from the University of Illinois at Chicago and B.E. in Power Engineering from Jadavpur University, India. His doctoral thesis focused on manipulating microvolume liquids using wettability patterning. His current research interest lies at the intersection of developing high aspect ratio functional micro/nanostructures and 3D NAND/DRAM fabrication in the semiconductor industry. He has contributed research articles/talks/IP in surface microfluidics, wettability patterning, multiphase heat transfer, electronics cooling, and plasma etching.

Souvick Chatterjee is a Senior Team Lead at MathWorks in the Education Team in India and is working on academic collaborations in research and curriculum. Currently, he is focusing on Industry 4.0 and cyber physical systems through incorporating data analytics and predictive technologies in thermofluidic systems. He worked at the University of Illinois at Chicago as a postdoctoral associate on wettability engineering and flow through porous media. He completed his B.E. from Jadavpur University and a dual M.S.−PhD degree from Jadavpur University and Virginia Tech. His expertise is in modeling and simulation of thermofluidic systems, data analytics, and experimental studies using PIV, PDPA, and liquid transport on wettability engineered porous media.

Sam Lowrey received his Ph.D in Physics from the University of Otago, New Zealand, where he is currently a Senior Lecturer. His research interests range from optical micro/nanofabrication to engineering thermodynamics. He has published on topics including nanolithographic imaging, computational fluid dynamics model development for two-phase flow in heat exchanger systems, heat pump systems configured for drying, and topographic wetting gradient systems.

Andrew D. Sommers is a Professor in the Department of Mechanical and Manufacturing Engineering at Miami University in Oxford, Ohio. He earned his Ph.D. and M.S. degrees in Mechanical Engineering from the University of Illinois in Champaign—Urbana and his B.S. in Mechanical Engineering from Clemson University. In 2008, he was awarded the ASHRAE New Investigator Award. His primary research focus is air-side heat transfer and the impact of surface wettability on



https://doi.org/10.1021/acs.chemrev.2c00045
*Chem. Rev.* 2022, 122, 16752−16801

condensate retention and frost growth in HVAC&R systems, where he has contributed papers. His research interests also include microfluidics, frost/icing mitigation and control, and the use of surface tension gradients to facilitate water droplet movement in preferred directions on surfaces.

Constantine M. Megaridis is University Distinguished Professor in Mechanical and Industrial Engineering at the University of Illinois at Chicago. He received his Ph.D. in Mechanical Engineering and M.S. in Applied Mathematics, both from Brown University, and a B.S. in Mechanical Engineering from the National Technical University of Athens, Greece. His research interests focus on fundamental and technological aspects of fluid dynamics and heat transfer, especially in the domains of droplet/particle processes, interfacial phenomena, and thermal management. He has contributed research papers that combine theory and experiments in multiphase flows, surface engineering, and transport phenomena in microfluidics.

## ACKNOWLEDGMENTS

P.S.M. acknowledges Saikat Halder for editorial corrections and proofreading. P.S.M. acknowledges partial support by the Indian Institute of Technology, Madras, to the Micro Nano Bio Fluidics Group under the funding for the Institutions of Eminence scheme of the Ministry of Education, Government of India [sanction. no 11/9/2019-U.3(A)]. C.M.M. acknowledges partial support by the U.S. Office of Naval Research under award number N00014-20-1-2025 to the University of Nebraska—Lincoln via a subcontract to the University of Illinois at Chicago.

## REFERENCES

(1) Manz, A.; Harrison, D. J.; Verpoorte, E. M.; Fettinger, J. C.; Paulus, A.; Lüdi, H.; Widmer, H. M. Planar Chips Technology for Miniaturization and Integration of Separation Techniques into Monitoring Systems: Capillary Electrophoresis on a Chip. *J. Chromatogr. A* **1992**, *593*, 253−258.
(2) Whitesides, G. M. The Origins and the Future of Microfluidics. *Nature* **2006**, *442*, 368−373.
(3) Bruus, H.*Theoretical Microfluidics*; Oxford Publishing, 2006.
(4) Haeberle, S.; Zengerle, R. Microfluidic Platforms for Lab-on-a-chip Appli cations. *Lab Chip* **2007**, *7*, 1094−1110.
(5) Foresti, D.; Nabavi, M.; Klingauf, M.; Ferrari, A.; Poulikakos, D. Acoustophoretic Contactless Transport and Handling of Matter in Air. *Proc. Natl. Acad. Sci. U. S. A.* **2013**, *110*, 12549−54.
(6) Puri, I. K.; Ganguly, R. Particle Transport in Therapeutic Magnetic Fields. *Annu. Rev. Fluid Mech.* **2014**, *46*, 407−40.
(7) Sackmann, E. K.; Fulton, A. L.; Beebe, D. J. The Present and Future Role of Microfluidics in Biomedical Research. *Nature* **2014**, *507*, 181−189.
(8) Hourtane, V.; Bodiguel, H.; Colin, A. Dense Bubble Traffic in Microfluidic Loops: Selection Rules and Clogging. *Phys. Rev. E* **2016**, *93*, 032607.
(9) Cong, H.; Xu, X.; Yu, B.; Liu, H.; Yuan, H. Fabrication of Anti-protein-fouling Poly (Ethylene Glycol) Microfluidic Chip Electrophoresis by Sandwich Photolithography. *Biomicrofluidics* **2016**, *10*, 044106.
(10) Unger, M. A.; Chou, H. P.; Thorsen, T.; Scherer, A.; Quake, S. R. Mono-lithic Microfabricated Valves and Pumps by Multilayer Soft Lithography. *Science* **2000**, *288*, 113−116.
(11) Sia, S. K.; Whitesides, G. M. Microfluidic Devices Fabricated in Poly (Dimethylsiloxane) for Biological Studies. *Electrophoresis* **2003**, *24*, 3563−3576.
(12) Guckenberger, D. J.; de Groot, T. E.; Wan, A. M.; Beebe, D. J.; Young, E. W. Micromilling: A Method for Ultra-rapid Prototyping of Plastic Microfluidic Devices. *Lab Chip* **2015**, *15*, 2364−2378.
(13) Madou, M. J.*Fundamentals of Microfabrication: The Science of Miniaturization*; CRC Press, 2002.
(14) McDonald, J. C.; Duffy, D. C.; Anderson, J. R.; Chiu, D. T.; Wu, H.; Schueller, O. J. A.; Whitesides, G. M. Fabrication of Microfluidic Systems in Poly (Dimethylsiloxane). *Electrophoresis* **2000**, *21*, 27−40.
(15) Van Oss, C. J.; Ju, L.; Chaudhury, M. K.; Good, R. J. Estimation of the Polar Parameters of the Surface Tension of Liquids by Contact Angle Measurements on Gels. *J. Colloid Interface Sci.* **1989**, *128*, 313−319.
(16) Fowkes, F. M. Dispersion Force Contributions to Surface and Interfacial Tensions, Contact Angles, and Heats of Immersion. *Adv. Chem.* **1964**, *43*, 99−111.
(17) Parvate, S.; Dixit, P.; Chattopadhyay, S. Superhydrophobic surfaces: insights from theory and experiment. *J. Phys. Chem. B* **2020**, *124*, 1323−1360.
(18) Attinger, D.; Frankiewicz, C.; Betz, A. R.; Schutzius, T. M.; Ganguly, R.; Das, A.; Kim, C. J.; Megaridis, C. M. Surface engineering for phase change heat transfer: A review. *MRS Energy Sustain.* **2014**, *1*, No. E4.
(19) Kang, Z.; Kong, T.; Lei, L.; Zhu, P.; Tian, X.; Wang, L. Engineering Particle Morphology with Microfluidic Droplets. *J. Micromech Microeng.* **2016**, *26*, 075011.
(20) Bremond, N.; Bibette, J. Exploring Emulsion Science with Microfluidics. *Soft Matter* **2012**, *8*, 10549−10559.
(21) Zhu, P.; Kong, T.; Tang, X.; Wang, L. Well-Defined Porous Membranes for Robust Omniphobic Surfaces via Microfluidic Emulsion Templating. *Nat. Commun.* **2017**, *8*, 15823.
(22) Wu, R.; Kim, T. Review of Microfluidic Approaches for Fabricating Intelligent Fiber Devices: Importance of Shape Characteristics. *Lab Chip* **2021**, *21*, 1217−1240.
(23) Du, X. Y.; Li, Q.; Wu, G.; Chen, S. Multifunctional Micro/Nanoscale Fibers Based on Microfluidic Spinning Technology. *Adv. Mater.* **2019**, *31*, 1903733.
(24) Rykaczewski, K.; Paxson, A. T.; Staymates, M.; Walker, M. L.; Sun, X.; Anand, S.; Srinivasan, S.; McKinley, G. H.; Chinn, J.; Scott, J. H.; Varanasi, K. K. Dropwise Condensation of Low Surface Tension Fluids on Omniphobic Surfaces. *Sci. Rep.* **2015**, *4*, 4158.
(25) Xu, J. H.; Li, S. W.; Lan, W. J.; Luo, G. S. Microfluidic Approach for Rapid Interfacial Tension Measurement. *Langmuir* **2008**, *24*, 11287−11292.
(26) Tsai, S. S.; Wexler, J. S.; Wan, J.; Stone, H. A. Microfluidic Ultralow Interfacial Tensiometry with Magnetic Particles. *Lab Chip* **2013**, *13*, 119−125.
(27) Zhou, H.; Yao, Y.; Chen, Q.; Li, G.; Yao, S. A Facile Microfluidic Strategy for Measuring Interfacial Tension. *Appl. Phys. Lett.* **2013**, *103*, 234102.
(28) Zhao, B.; MacMinn, C. W.; Juanes, R. Wettability Control on Multiphase Flow in Patterned Microfluidics. *Proc. Natl. Acad. Sci. U. S. A.* **2016**, *113*, 10251−10256.
(29) Holtzman, R.; Segre, E. Wettability Stabilizes Fluid Invasion into Porous Media via Nonlocal, Cooperative Pore Filling. *Phys. Rev. Lett.* **2015**, *115*, 164501.
(30) Kang, K. K.; Lee, B.; Lee, C. S. Microfluidic Approaches for The Design of Functional Materials. *Microelectron. Eng.* **2018**, *199*, 1−5.
(31) Zhu, P.; Wang, L. Microfluidics-Enabled Soft Manufacture of Materials with Tailorable Wettability. *Chem. Rev.* **2022**, *122*, 7010−7060.
(32) Zhu, P; Wang, L.*Microfluidics-Enabled Soft Manufacture, ISBN 978−3-030−96462−7*; Springer Nature: Switzerland, AG, 2022.
(33) Ghosh, A.; Ganguly, R.; Schutzius, T. M.; Megaridis, C. M. Wettability Patterning for High-rate, Pumpless Fluid Transport on Open, Non-planar Microfluidic Platforms. *Lab Chip* **2014**, *14*, 1538−1550.
(34) Chatterjee, S.; Mahapatra, P. S.; Ibrahim, A.; Ganguly, R.; Yu, L.; Dodge, R.; Megaridis, C. M. Precise Liquid Transport on and through Thin Porous Materials. *Langmuir* **2018**, *34*, 2865−2875.
(35) Zhao, Y.; Wang, H.; Zhou, H.; Lin, T. Directional Fluid Transport in Thin Porous Materials and its Functional Applications. *Small* **2017**, *13*, 1601070.


https://doi.org/10.1021/acs.chemrev.2c00045
*Chem. Rev.* 2022, 122, 16752−16801

(36) Smith, J. D.; Dhiman, R.; Anand, S.; Reza-Garduno, E.; Cohen, R. E.; McKinley, G. H.; Varanasi, K. K. Droplet Mobility on Lubricant-impregnated Surfaces. *Soft Matter* **2013**, *9*, 1772−1780.
(37) Simpson, J. T.; Hunter, S. R.; Aytug, T. Superhydrophobic Materials and Coatings: A Review. *Rep. Prog. Phys.* **2015**, *78*, 086501.
(38) Martinez, A. W.; Phillips, S. T.; Whitesides, G. M.; Carrilho, E. Diagnostics for the Developing World: Microfluidic Paper-based Analytical Devices. *Anal. Chem.* **2010**, *82*, 3−10.
(39) Nelson, W. C.; Kim, C. J. Droplet Actuation by Electrowetting-on-dielectric (EWOD): A Review. *J. Adhes. Sci. Technol.* **2012**, *26*, 1747−1771.
(40) Park, S. Y.; Teitell, M. A.; Chiou, E. P. Single-sided Continuous Optoelectrowetting (SCOEW) for Droplet Manipulation with Light Patterns. *Lab Chip* **2010**, *10*, 1655−1661.
(41) Long, Z.; Shetty, A. M.; Solomon, M. J.; Larson, R. G. Fundamentals of Magnet-actuated Droplet Manipulation on an Open Hydrophobic Surface. *Lab Chip* **2009**, *9*, 1567−1575.
(42) Chakrabarty, D.; Dutta, S.; Chakraborty, N.; Ganguly, R. Magnetically Actuated Transport of Ferrofluid Droplets over Micro-Coil Array on a Digital Microfluidic Platform. *Sens. Actuators, B* **2016**, *236*, 367−377.
(43) Narayanamurthy, V.; Jeroish, Z. E.; Bhuvaneshwari, K. S.; Bayat, P.; Premkumar, R.; Samsuri, F.; Yusoff, M. M. Advances in Passively Driven Microfluidics and Lab-On-Chip Devices: A Comprehensive Literature Review and Patent Analysis. *RSC Adv.* **2020**, *10*, 11652−11680.
(44) Gau, H.; Herminghaus, S.; Lenz, P.; Lipowsky, R. Liquid Morphologies on Structured Surfaces: From Microchannels to Microchips. *Science* **1999**, *283*, 46−49.
(45) Schutzius, T. M.; Elsharkawy, M.; Tiwari, M. K.; Megaridis, C. M. Surface Tension Confined (STC) Tracks for Capillary-driven Transport of Low Surface Tension Liquids. *Lab Chip* **2012**, *12*, 5237−5242.
(46) Lowrey, S.; Misiiuk, K.; Blaikie, R.; Sommers, A. Survey of Micro/nanofabricated Chemical, Topographical, and Compound Passive Wetting Gradient Surfaces. *Langmuir* **2022**, *38*, 605−619.
(47) Edalatpour, E.; Liu, L.; Jacobi, A. M.; Eid, K. F.; Sommers, A. D. Managing Water on Heat Transfer Surfaces: A Critical Review of Techniques to Modify Surface Wettability for Applications with Condensation or Evaporation. *Appl. Energy* **2018**, *222*, 967−992.
(48) Sommers, A. D.; Brest, T. J.; Eid, K. F. Topography-based Surface Tension Gradients to Facilitate Water Droplet Movement on Laser-etched Copper Substrates. *Langmuir* **2013**, *29*, 12043−12050.
(49) Bayiati, P.; Tserepi, A.; Gogolides, E.; Misiakos, K. Selective Plasma-induced Deposition of Fluorocarbon Films on Metal Surfaces for Actuation in Microfluidics. *J. Vac. Sci. Technol., A* **2004**, *22*, 1546−1551.
(50) Ji, H.; Côté, A.; Koshel, D.; Terreault, B.; Abel, G.; Ducharme, P.; Ross, G.; Savoie, S.; Gagné, M. Hydrophobic Fluorinated Carbon Coatings on Silicate Glaze and Aluminum. *Thin Solid Films* **2002**, *405*, 104−108.
(51) Elkin, B.; Mayer, J.; Schindler, B.; Vohrer, U. Wettability, Chemical and Morphological Data of Hydrophobic Layers by Plasma Polymerization on Smooth Substrates. *Surf. Coat. Technol.* **1999**, *116*, 836−840.
(52) Yu, R.; Sommers, A. D.; Okamoto, N. C. Effect of a Micro-grooved Fin Surface Design on the Air-side Thermal-hydraulic Performance of a Plain Fin-and-tube Heat Exchanger. *Int. J. Refrig.* **2013**, *36*, 1078−1089.
(53) Ma, J.; Sett, S.; Cha, H.; Yan, X.; Miljkovic, N. Recent Developments, Challenges, and Pathways to Stable Dropwise Condensation: A Perspective. *Appl. Phys. Lett.* **2020**, *116*, 260501.
(54) Malinowski, R.; Parkin, I. P.; Volpe, G. Advances towards Programmable Droplet Transport on Solid Surfaces and Its Applications. *Chem. Soc. Rev.* **2020**, *49*, 7879−7892.
(55) Liu, J.; Li, S. Capillarity-driven Migration of Small Objects: A Critical Review. *Eur. Phys. J. E* **2019**, *42*, 1.
(56) de Gennes, P. G.; Brochard-Wyart, F; Quéré, D.*Capillarity and Wetting Phenomena: Drops, Bubbles, Pearls, Waves*; Springer Science & Business Media, 2013.
(57) Bonn, D.; Eggers, J.; Indekeu, J.; Meunier, J.; Rolley, E. Wetting and Spreading. *Rev. Mod. Phys.* **2009**, *81*, 739−805.
(58) Tanner, L. H. The Spreading of Silicone Oil Drops on Horizontal Surfaces. *J. Phys. D: Appl. Phys.* **1979**, *12*, 1473−1484.
(59) Lopez, J.; Miller, C. A.; Ruckenstein, E. Spreading Kinetics of Liquid Drops on Solids. *J. Colloid Interface Sci.* **1976**, *56*, 460−468.
(60) Brochard-Wyart, F.; Hervet, H.; Redon, C.; Rondelez, F. Spreading of "Heavy" Droplets: I. Theory. *J. Colloid Interface Sci.* **1991**, *142*, 518−527.
(61) Redon, C.; Brochard-Wyart, F.; Hervet, H.; Rondelez, F. Spreading of "Heavy" Droplets: II. Experiments. *J. Colloid Interface Sci.* **1992**, *149*, 580−591.
(62) Cazabat, A. M.; Stuart, M. A. Dynamics of Wetting: Effects of Surface Roughness. *J. Phys. Chem.* **1986**, *90*, 5845−5849.
(63) Rafaï, S.; Bonn, D.; Boudaoud, A. Spreading of Non-Newtonian Fluids on Hydrophilic Surfaces. *J. Fluid Mech.* **1999**, *513*, 77−85.
(64) Quéré, D. Wetting and Roughness. *Annu. Rev. Mater. Res.* **2008**, *38*, 71−99.
(65) Washburn, E. W. The Dynamics of Capillary Flow. *Phys. Rev.* **1921**, *17*, 273.
(66) Cate, D. M.; Adkins, J. A.; Mettakoonpitak, J.; Henry, C. S. Recent Developments in Paper-based Microfluidic Devices. *Anal. Chem.* **2015**, *87*, 19−41.
(67) Goldman, R. Curvature Formulas for Implicit Curves and Surfaces. *Comput. Aided Geom. Des.* **2005**, *22*, 632−658.
(68) Xing, S.; Harake, R. S.; Pan, T. Droplet-driven Transports on Superhydrophobic-patterned Surface Microfluidics. *Lab Chip* **2011**, *11*, 3642−3648.
(69) Hermann, M.; Bachus, K.; Gibson, G. T. T.; Oleschuk, R. D. Open Sessile Droplet Viscometer with Low Sample Consumption. *Lab Chip* **2020**, *20*, 1869−1876.
(70) Mahlberg, L.; Hermann, M.; Ramsay, H.; Salomons, T.; Stamplecoskie, K.; Oleschuk, R. D. Portable Microfluidic Platform Employing Young-Laplace Pumping Enabling Flowrate Controlled Applications. *Microfluid. Nanofluid.* **2021**, *25*, 48.
(71) Brinkmann, M.; Lipowsky, R. Wetting Morphologies on Substrates with Striped Surface Domains. *J. Appl. Phys.* **2002**, *92*, 4296−4306.
(72) Khoo, H. S.; Tseng, F. G. Spontaneous High-speed Transport of Subnanoliter Water Droplet on Gradient Nanotextured Surfaces. *Appl. Phys. Lett.* **2009**, *95*, 063108.
(73) Alheshibri, M. H.; Rogers, N. G.; Sommers, A. D.; Eid, K. F. Spontaneous Movement of Water Droplets on Patterned Cu and Al Surfaces with Wedge-shaped Gradients. *Appl. Phys. Lett.* **2013**, *102*, 174103.
(74) Cira, N.; Benusiglio, A.; Prakash, M. Vapour-mediated Sensing and Motility in Two-component Droplets. *Nature* **2015**, *519* (7544), 446−50.
(75) Chakraborty, M.; Ghosh, U. U.; Chakraborty, S.; DasGupta, S. Thermally Enhanced Self-propelled Droplet Motion on Gradient Surfaces. *RSC Ad v.* **2015**, *5*, 45266−45275.
(76) Darhuber, A. A.; Valentino, J. P.; Troian, S. M.; Wagner, S. Thermo-capillary Actuation of Droplets on Chemically Patterned Surfaces by Programmable Microheater Arrays. *J. Microelectromech. Syst.* **2003**, *12*, 873−879.
(77) Chaudhury, M. K.; Whitesides, G. M. How to Make Water Run Uphill. *Science* **1992**, *256*, 1539−1541.
(78) Ghosh, A.; Beaini, S.; Zhang, B. J.; Ganguly, R.; Megaridis, C. M. Enhancing Dropwise Condensation Through Bioinspired Wettability Patterning. *Langmuir* **2014**, *30*, 13103−13115.
(79) Liu, K.; Jiang, L. Metallic Surfaces with Special Wettability. *Nanoscale* **2011**, *3*, 825−838.
(80) Tian, D.; Song, Y.; Jiang, L. Patterning of Controllable Surface Wettability for Printing Techniques. *Chem. Soc. Rev.* **2013**, *42*, 5184−5209.
(81) Li, H.; Li, A.; Zhao, Z.; Li, M.; Song, Y. Heterogeneous Wettability Surfaces: Principle, Construction, and Applications. *Small Struct.* **2020**, *1*, 2000028.


https://doi.org/10.1021/acs.chemrev.2c00045
*Chem. Rev.* 2022, 122, 16752−16801

(82) Chi, J.; Zhang, X.; Wang, Y.; Shao, C.; Shang, L.; Zhao, Y. Bio-inspired Wettability Patterns for Biomedical Applications. *Mater. Horiz.* **2021**, *8*, 124−144.
(83) Li, H.; Yang, Q.; Li, G.; Li, M.; Wang, S.; Song, Y. Splitting a Droplet for Femtoliter Liquid Patterns and Single Cell Isolation. *ACS Appl. Mater. Interfaces* **2015**, *7*, 9060−9065.
(84) Liu, X.; Kanehara, M.; Liu, C.; Sakamoto, K.; Yasuda, T.; Takeya, J.; Minari, T. Spontaneous Patterning of High-Resolution Electronics via Parallel Vacuum Ultraviolet. *Adv. Mater.* **2016**, *28*, 6568−6573.
(85) Tadanaga, K.; Morinaga, J.; Matsuda, A.; Minami, T. Super-hydrophobic-superhydrophilic Micropatterning on Flower-like Alumina Coating Film by the Sol-gel Method. *Chem. Mater.* **2000**, *12*, 590−592.
(86) Lee, J. H.; Kim, S. K.; Park, H. H.; Kim, T. S. $Tio_2$ Coated Microfluidic Devices for Recoverable Hydrophilic and Hydrophobic Patterns. *J. Micromech. Microeng.* **2015**, *25*, 035032.
(87) Bodin-Thomazo, N.; Malloggi, F.; Guenoun, P. Marker Patterning: A Spatially Resolved Method for Tuning the Wettability of PDMS. *RSC Adv.* **2017**, *7*, 46514−46519.
(88) Pascual, M.; Kerdraon, M.; Rezard, Q.; Jullien, M. C.; Champougny, L. Wettability Patterning in Microfluidic Devices using Thermally-enhanced Hydrophobic Recovery of PDMS. *Soft Matter* **2019**, *15*, 9253−9260.
(89) Li, J.; Li, L.; Du, X.; Feng, W.; Welle, A.; Trapp, O.; Grunze, M.; Hirtz, M.; Levkin, P. A. Reactive Superhydrophobic Surface and Its Photoinduced Disulfide-ene and Thiol-ene (Bio) Functionalization. *Nano Lett.* **2015**, *15*, 675−681.
(90) Jin, Y.; Song, K.; Gellermann, N.; Huang, Y. Printing of Hydrophobic Materials in Fumed Silica Nanoparticle Suspension. *ACS Appl. Mater. Interfaces* **2019**, *11*, 29207−29217.
(91) Megaridis, C. M.; Ganguly, R.; Ghosh, A.; Schutzius, T., inventors; University of Illinois, assignee. Wettability Patterned Substrates for Pumpless Liquid Transport and Drainage, U.S. Patent 10,421,072, 2019.
(92) Schirmer, N. C.; Ströhle, S.; Tiwari, M. K.; Poulikakos, D. On the Principles of Printing Sub-micrometer 3D Structures from Dielectric-liquid-based Colloids. *Adv. Funct. Mater.* **2011**, *21*, 388−395.
(93) Li, J.; Hou, Y.; Liu, Y.; Hao, C.; Li, M.; Chaudhury, M. K.; Yao, S.; Wang, Z. Directional Transport of High-temperature Janus Droplets Mediated by Structural Topography. *Nat. Phys.* **2016**, *12*, 606−612.
(94) Bizi-Bandoki, P.; Benayoun, S.; Valette, S.; Beaugiraud, B.; Audouard, E. Modifications of Roughness and Wettability Properties of Metals Induced by Femtosecond Laser Treatment. *Appl. Surf. Sci.* **2011**, *257*, 5213−5218.
(95) Chen, B.; Johnson, Z. T.; Sanborn, D.; Hjort, R. G.; Garland, N. T.; Soares, R. R. A.; Van Belle, B.; Jared, N.; Li, J.; Jing, D.; Smith, E. A.; Gomes, C. L.; Claussen, J. C. Tuning the Structure, Conductivity, and Wettability of Laser-Induced Graphene for Multiplexed Open Microfluidic Environmental Biosensing and Energy Storage Devices. *ACS Nano* **2022**, *16*, 15−28.
(96) Hall, L. S.; Hwang, D.; Chen, B.; Van Belle, B.; Johnson, Z. T.; Hondred, J. A.; Gomes, C. L.; Bartlett, M. D.; Claussen, J. C. All-graphene-based open fluidics for pumpless, small-scale fluid transport via laser-controlled wettability patterning. *Nanoscale Horiz.* **2021**, *6*, 24−32.
(97) Patra, S.; Andriamiadamanana, C.; Tulodziecki, M.; Davoisne, C.; Taberna, P. L.; Sauvage, F. Low-temperature Electrodeposition Approach Leading to Robust Mesoscopic Anatase $TiO_2$ Films. *Sci. Rep.* **2016**, *6*, 21588.
(98) Ghosh, R.; Sahu, R. P.; Ganguly, R.; Zhitomirsky, I.; Puri, I. K. Photocatalytic Activity of Electrophoretically Deposited $Tio_2$ and Zno Nanoparticles on Fog Harvesting Meshes. *Ceram. Int.* **2020**, *46*, 3777−3785.
(99) Raman, A.; Jayan, J. S.; Deeraj, B. D.; Saritha, A.; Joseph, K. Electrospun Nanofibers as Effective Superhydrophobic Surfaces: A Brief Review. *Surf. Interfaces* **2021**, *24*, 101140.
(100) Lalia, B. S.; Anand, S.; Varanasi, K. K.; Hashaikeh, R. Fog-harvesting Potential of Lubricant-impregnated Electrospun Nanomats. *Langmuir* **2013**, *29*, 13081−13088.
(101) Yasuda, T.; Suzuki, K.; Shimoyama, I.Automatic Transportation of a Droplet on a Wettability Gradient Surface. In *7th International Conference on Miniaturized Chemical and Blochemlcal Analysts Systems, October 5-9, 2003, Squaw Valley, Callfornla*, 2003; Vol. *2*, pp 1129−1132.
(102) Shastry, A.; Case, M. J.; Bohringer, K. F. Directing Droplets using Microstructured Surfaces. *Langmuir* **2006**, *22*, 6161−6167.
(103) Yang, J. T.; Chen, J. C.; Huang, K. J.; Yeh, J. A. Droplet Manipulation on a Hydrophobic Textured Surface with Roughened Patterns. *J. Microelectromech. Syst.* **2006**, *15*, 697−707.
(104) Khoo, H. S.; Tseng, F. G.Self-directed Movements of Droplets on Radially Patterned Surfaces Based on Self-assembled Monolayers. In *International Conference on Microtechnologies in Medicine and Biology*; IEEE, 2006; pp 273−276.
(105) Sun, C.; Zhao, X. W.; Han, Y. H.; Gu, Z. Z. Control of Water Droplet Motion by Alteration of Roughness Gradient on Silicon Wafer by Laser Surface Treatment. *Thin Solid Films* **2008**, *516*, 4059−4063.
(106) Yang, J. T.; Yang, Z. H.; Chen, C. Y.; Yao, D. J. Conversion of Surface Energy and Manipulation of a Single Droplet across Micropatterned Surfaces. *Langmuir* **2008**, *24*, 9889−9897.
(107) Reyssat, M.; Pardo, F.; Quere, D. Drops onto Gradients of Texture. *EPL (Europhys. Lett.)* **2009**, *87*, 36003.
(108) Lai, Y. H.; Yang, J. T.; Shieh, D. B. A Microchip Fabricated with a Vapor-diffusion Self-assembled-monolayer Method to Transport Droplets across Superhydrophobic to Hydrophilic Surfaces. *Lab Chip* **2010**, *10*, 499−504.
(109) Spori, D. M.; Drobek, T.; Zurcher, S.; Spencer, N. D. Cassie-state Wetting Investigated by Means of a Hole-to-pillar Density Gradient. *Langmuir* **2010**, *26*, 9465−9473.
(110) Langley, K. R.; Sharp, J. S. Microtextured Surfaces with Gradient Wetting Properties. *Langmuir* **2010**, *26*, 18349−18356.
(111) Chu, K. H.; Xiao, R.; Wang, E. N. Uni-directional Liquid Spreading on Asymmetric Nanostructured Surfaces. *Nat. Mater.* **2010**, *9*, 413−417.
(112) Bliznyuk, O.; Jansen, H. P.; Kooij, E. S.; Zandvliet, H. J.; Poelsema, B. Smart Design of Stripepatterned Gradient Surfaces to Control Droplet Motion. *Langmuir* **2011**, *27*, 11238−11245.
(113) Chandesris, B.; Soupremanien, U.; Dunoyer, N. Uphill Motion of Droplets on Tilted and Vertical Grooved Substrates Induced by a Wettability Gradient. *Colloids Surf., A* **2013**, *434*, 126−135.
(114) Li, J.; Tian, X.; Perros, A. P.; Franssila, S.; Jokinen, V. Self-propelling and Positioning of Droplets using Continuous Topography Gradient Surface. *Adv. Mater. Interfaces* **2014**, *1*, 1400001.
(115) Dorri, N.; Shahbazi, P.; Kiani, A. Self-movement of Water Droplet at the Gradient Nanostructure of Cu Fabricated using Bipolar Electrochemistry. *Langmuir* **2014**, *30*, 1376−1382.
(116) Zamuruyev, K. O.; Bardaweel, H. K.; Carron, C. J.; Kenyon, N. J.; Brand, O.; Delplanque, J. P.; Davis, C. E. Continuous Droplet Removal upon Dropwise Condensation of Humid Air on a Hydrophobic Micropatterned Surface. *Langmuir* **2014**, *30*, 10133−10142.
(117) Hou, Y. P.; Feng, S. L.; Dai, L. M.; Zheng, Y. M. Droplet Manipulation on Wettable Gradient Surfaces with Micro-/nano-hierarchical Structure. *Chem. Mater.* **2016**, *28*, 3625−3629.
(118) Liu, C.; Sun, J.; Li, J.; Xiang, C.; Che, L.; Wang, Z.; Zhou, X. Long-range Spontaneous Droplet Self-propulsion on Wettability Gradient Surfaces. *Sci. Rep.* **2017**, *7*, 7552.
(119) Li, J.; Zhou, X.; Li, J.; Che, L.; Yao, J.; McHale, G.; Chaudhury, M. K.; Wang, Z. Topological Liquid Diode. *Sci. Adv.* **2017**, *3*, No. eaao3530.
(120) Wang, X.; Xu, B.; Chen, Y.; Ma, C.; Huang, Y. Fabrication of Micro/nano-hierarchical Structures for Droplet Manipulation via Velocity-controlled Picosecond Laser Surface Texturing. *Opt. Lasers Eng.* **2019**, *122*, 319−27.
(121) Sommers, A. D.; Panth, M.; Eid, K. F. Spontaneous Water Droplet Movement on a Copper Radial Gradient Surface. *Appl. Therm. Eng.* **2020**, *173*, 115226.
(122) Xu, C. X.; Jia, Z. H.; Lian, X. H. Wetting and Adhesion Energy of Droplets on Wettability Gradient Surfaces. *J. Mater. Sci.* **2020**, *55*, 8185−8198.


https://doi.org/10.1021/acs.chemrev.2c00045
*Chem. Rev.* 2022, 122, 16752−16801

(123) Chai, H.; Tian, Y.; Yu, S.; Cao, B.; Peng, X.; Zhang, Z.; Liu, A.; Wu, H. Large-range, Reversible Directional Spreading of Droplet on a Double-gradient Wrinkled Surface Adjusted under Mechanical Strain. *Adv. Mater. Interfaces* **2020**, *7*, 1901980.
(124) Wang, Y.; Cui, C.; Qi, B.; Wei, J.; Zhang, Y. Study of Droplet Self-migration on Silicon Surface with Radial Micro-fin Structures. *Exp. Therm Fluid Sci.* **2020**, *114*, 110075.
(125) Yang, Q.; Lv, Z.; Wu, T.; Chen, Y.; Ren, X.; Cheng, J.; Lou, D.; Chen, L.; Zheng, Z.; Rui, Q.; Liu, D. Formation Mechanism of Gradient Wettability of Si3N4 Ceramic Surface Induced using a Femtosecond Laser. *Phys. Status Solidi A* **2020**, *217*, 2000105.
(126) Kumar, M.; Bhardwaj, R.; Sahu, K. C. Wetting Dynamics of a Water Droplet on Micro-pillar Surfaces with Radially Varying Pitches. *Langmuir* **2020**, *36*, 5312−5323.
(127) Tokunaga, A.; Tsuruta, T. Enhancement of Condensation Heat Transfer on a Microstructured Surface with Wettability Gradient. *Int. J. Heat Mass Transfer* **2020**, *156*, 119839.
(128) Feng, S.; Delannoy, J.; Malod, A.; Zheng, H.; Quere, D.; Wang, Z. Tip-induced Flipping of Droplets on Janus Pillars: From Local Reconfiguration to Global Transport. *Sci. Adv.* **2020**, *6*, No. eabb4540.
(129) Misiiuk, K.; Lowrey, S.; Blaikie, R.; Juras, J.; Sommers, A. D. Development of a Coating-less Aluminium Superhydrophobic Gradient for Spontaneous Water Droplet Motion using One-step Laser-ablation. *Langmuir* **2022**, *38*, 1954−1965.
(130) Martinez, A. W.; Phillips, S. T.; Butte, M. J.; Whitesides, G. M. Patterned Paper as a Platform for Inexpensive, Low-volume, Portable Bioassays. *Angew. Chem., Int. Ed.* **2007**, *46*, 1318−1320.
(131) Choudhary, T.; Rajamanickam, G.; Dendukuri, D. Woven Electrochemical Fabric-based Test Sensors (WEFTS): A New Class of Multiplexed Electrochemical Sensors. *Lab Chip* **2015**, *15*, 2064−2072.
(132) Li, X.; Ballerini, D. R.; Shen, W. A Perspective on Paper-based Microfluidics: Current Status and Future Trends. *Biomicrofluidics* **2012**, *6*, 011301.
(133) Liu, Z.; Hu, J.; Zhao, Y.; Qu, Z.; Xu, F. Experimental and Numerical Studies on Liquid Wicking into Filter Papers for Paper-based Diagnostics. *Appl. Therm. Eng.* **2015**, *88*, 280−287.
(134) Fries, N.; Odic, K.; Conrath, M.; Dreyer, M. The Effect of Evaporation on the Wicking of Liquids into a Metallic Weave. *J. Colloid Interface Sci.* **2008**, *321*, 118−129.
(135) Patari, S.; Mahapatra, P. S. Liquid Wicking in a Paper Strip: An Experimental and Numerical Study. *ACS Omega* **2020**, *5*, 22931−22939.
(136) Schuchardt, D. R.; Berg, J. C. Liquid Transport in Composite Cellulose-Super Absorbent Fiber Network. *Wood Fiber Sci.* **1991**, *23* (3), 342−357.
(137) Patari, S.; Mahapatra, P. S. Imbibition of Liquids through a Paper Substrate in a Controlled Environment. *Langmuir* **2022**, *38*, 4736−4746.
(138) Subramanian, R. S.; Moumen, N.; McLaughlin, J. B. Motion of a Drop on a Solid Surface due to a Wettability Gradient. *Langmuir* **2005**, *21*, 11844−11849.
(139) Tam, D.; von Arnom, V.; McKinley, G. H.; Hosoi, A. E. Marangoni Convection in Droplets on Superhydrophobic Surfaces. *J. Fluid Mech.* **2009**, *624*, 101−123.
(140) Diguet, A.; Guillermic, R. M.; Magome, N.; Saint-Jalmes, A.; Chen, Y.; Yoshikawa, K.; Baigl, D. Photomanipulation of a Droplet by the Chromocapillary Effect. *Angew. Chem., Int. Ed.* **2009**, *48*, 9281−9284.
(141) Xiao, Y.; Zarghami, S.; Wagner, K.; Wagner, P.; Gordon, K. C.; Florea, L.; Diamond, D.; Officer, D. L. Moving Droplets in 3D using Light. *Adv. Mater.* **2018**, *30*, 1801821.
(142) Darhuber, A. A.; Valentino, J. P.; Troian, S. M. Planar Digital Nanoliter Dispensing System Based on Thermocapillary Actuation. *Lab Chip* **2010**, *10*, 1061−1071.
(143) Dai, Q.; Ji, Y.; Huang, W.; Wang, X. On the Thermocapillary Migration on Radially Microgrooved Surfaces. *Langmuir* **2019**, *35*, 9169−9176.
(144) Zhao, Y.; Liu, F.; Chen, C. H. Thermocapillary Actuation of Binary Drops on Solid Surfaces. *Appl. Phys. Lett.* **2011**, *99*, 104101.
(145) Linke, H.; Alemán, B. J.; Melling, L. D.; Taormina, M. J.; Francis, M. J.; Dow-Hygelund, C. C.; Narayanan, V.; Taylor, R. P.; Stout, A. Self-propelled Leidenfrost Droplets. *Phys. Rev. Lett.* **2006**, *96*, 154502.
(146) Leidenfrost, J. G.*De Aquae Communis Nonnullis Qualitatibus Tractatus*; Ovenius, 1756.
(147) Lagubeau, G.; Le Merrer, M.; Clanet, C.; Quéré, D. Leidenfrost on a Ratchet. *Nat. Phys.* **2011**, *7*, 395−398.
(148) Greenspan, H. P. On the Motion of a Small Viscous Droplet that Wets a Surface. *J. Fluid Mech.* **1978**, *84*, 125−143.
(149) Brochard, F. Motions of Droplets on Solid Surfaces Induced by Chemical or Thermal Gradients. *Langmuir* **1989**, *5*, 432−438.
(150) de Gennes, P. G. Wetting: Statics and Dynamics. *Rev. Mod. Phys.* **1985**, *57*, 827−863.
(151) Daniel, S.; Chaudhury, M. K. Rectified Motion of Liquid Drops on Gradient Surfaces Induced by Vibration. *Langmuir* **2002**, *18*, 3404−3407.
(152) Ito, Y.; Heydari, M.; Hashimoto, A.; Konno, T.; Hirasawa, A.; Hori, S.; Kurita, K.; Nakajima, A. The Movement of a Water Droplet on a Gradient Surface Prepared by Photodegradation. *Langmuir* **2007**, *23*, 1845−1850.
(153) Daniel, S.; Sircar, S.; Gliem, J.; Chaudhury, M. K. Ratcheting Motion of Liquid Drops on Gradient Surfaces. *Langmuir* **2004**, *20*, 4085−4092.
(154) Biance, A. L.; Clanet, C.; Quéré, D. First Steps in the Spreading of a Liquid Droplet. *Phys. Rev. E* **2004**, *69*, 016301.
(155) Zhu, X.; Wang, H.; Liao, Q.; Ding, Y. D.; Gu, Y. B. Experiments and Analysis on Self-motion Behaviors of Liquid Droplets on Gradient Surfaces. *Exp. Therm Fluid Sci.* **2009**, *33*, 947−954.
(156) Dos Santos, F. D.; Ondarcuhu, T. Free-running Droplets. *Phys. Rev. Lett.* **1995**, *75*, 2972−2975.
(157) Zorba, V.; Persano, L.; Pisignano, D.; Athanassiou, A.; Stratakis, E.; Cingolani, R.; Tzanetakis, P.; Fotakis, C. Making Silicon Hydrophobic: Wettability Control by Two-lengthscale Simultaneous Patterning with Femto-second Laser Irradiation. *Nanotechnology* **2006**, *17*, 3234.
(158) Lv, C.; Hao, P. Driving Droplet by Scale Effect on Microstructured Hydrophobic Surfaces. *Langmuir* **2012**, *28*, 16958−16965.
(159) Darhuber, A. A.; Troian, S. M.; Reisner, W. W. Dynamics of Capillary Spreading along Hydrophilic Microstripes. *Phys. Rev. E* **2001**, *64*, 031603.
(160) Huang, S.; Song, J.; Lu, Y.; Chen, F.; Zheng, H.; Yang, X.; Liu, X.; Sun, J.; Carmalt, C. J.; Parkin, I. P.; Xu, W. Underwater Spontaneous Pumpless Transportation of Nonpolar Organic Liquids on Extreme Wettability Patterns. *ACS Appl. Mater. Interfaces* **2016**, *8*, 2942−2949.
(161) Marlow, J.*Why Spacecraft of the Future Will Be Packed with Microfluidics?*Wired, 2013; https://www.wired.com/2013/06/why-spacecraft-of-the-future-will-be-packed-with-microfluidics/.
(162) Sen, U.; Chatterjee, S.; Ganguly, R.; Dodge, R.; Yu, L.; Megaridis, C. M. Scaling Laws in Directional Spreading of Droplets on Wettability-confined Diverging Tracks. *Langmuir* **2018**, *34*, 1899−1907.
(163) Morrissette, J.; Ghosh, A.; Campos, R.; Mates, J. E.; Mabry, J. M.; Megaridis, C. M. Fluorinated Nanocomposite Coatings for Confinement and Pumpless Transport of Low-surface-tension Liquids. *Adv. Mater. Interfaces* **2019**, *6*, 1901105.
(164) Gukeh, M. J.; Roy, T.; Sen, U.; Ganguly, R.; Megaridis, C. M. Lateral Spreading of Gas Bubbles on Submerged Wettability-confined Tracks. *Langmuir* **2020**, *36*, 11829−11835.
(165) Lorenceau, É; Quéré, D. Drops on a Conical Wire. *J. Fluid Mech.* **1999**, *510*, 29−45.
(166) Adam, N. K. Detergent Action and its Relation to Wetting and Emulsification. *J. Soc. Dye. Colour.* **1937**, *53*, 121−129.
(167) McHale, G.; Newton, M. I.; Carroll, B. J. The Shape and Stability of Small Liquid Drops on Fibers. *Oil Gas Sci. Technol.* **2001**, *56*, 47−54.


https://doi.org/10.1021/acs.chemrev.2c00045
*Chem. Rev.* 2022, 122, 16752−16801

(168) Carroll, B. J. The Accurate Measurement of Contact Angle, Phase Contact Areas, Drop Volume, and Laplace Excess Pressure in Drop-on-fiber Systems. *J. Colloid Interface Sci.* **1976**, *57*, 488−495.
(169) Li, Y.; Wu, H.; Wang, F. Stagnation of a Droplet on a Conical Substrate Determined by the Critical Curvature Ratio. *J. Phys. D: Appl. Phys.* **2016**, *49*, 085304.
(170) Ju, J.; Bai, H.; Zheng, Y.; Zhao, T.; Fang, R.; Jiang, L. A Multi-structural and Multi-functional Integrated Fog Collection System in Cactus. *Nat. Commun.* **2012**, *3*, 1247.
(171) Ju, J.; Yao, X.; Yang, S.; Wang, L.; Sun, R.; He, Y.; Jiang, L. Cactus Stem Inspired Cone-arrayed Surfaces for Efficient Fog Collection. *Adv. Funct. Mater.* **2014**, *24*, 6933−6938.
(172) Renvoisé, P.; Bush, J. W. M.; Prakash, M.; Quéré, D. Drop Propulsion in Tapered Tubes. *EPL (Europhys. Lett.)* **2009**, *86*, 64003.
(173) Prakash, M.; Quéré, D.; Bush, J. W. M. Surface Tension Transport of Prey by Feeding Shorebirds: The Capillary Ratchet. *Science* **2008**, *320*, 931−934.
(174) Liu, C.; Xue, Y.; Chen, Y.; Zheng, Y. Effective Directional Self-gathering of Drops on Spine of Cactus with Splayed Capillary Arrays. *Sci. Rep.* **2015**, *5*, 17757.
(175) Mertaniemi, H.; Jokinen, V.; Sainiemi, L.; Franssila, S.; Marmur, A.; Ikkala, O.; Ras, R. H. Superhydrophobic Tracks for Low-friction, Guided Transport of Water Droplets. *Adv. Mater.* **2011**, *23*, 2911−2914.
(176) Chowdhury, I. U.; Mahapatra, P. S.; Sen, A. K.; Pattamatta, A.; Tiwari, M. K. Autonomous Transport and Splitting of a Droplet on an Open Surface. *Phys. Rev. Fluids* **2021**, *6*, 094003.
(177) Cassie, A. B.; Baxter, S. Wettability of Porous Surfaces. *Trans. Faraday Soc.* **1944**, *40*, 546−551.
(178) Wenzel, R. N. Resistance of Solid Surfaces to Wetting by Water. *Ind. Eng. Chem.* **1936**, *28*, 988−994.
(179) Cao, L.; Hu, H. H.; Gao, D. Design and Fabrication of Micro-textures for Inducing a Superhydrophobic Behavior on Hydrophilic Materials. *Langmuir* **2007**, *23*, 4310−4314.
(180) Zheng, Y.; Bai, H.; Huang, Z.; Tian, X.; Nie, F. Q.; Zhao, Y.; Zhai, J.; Jiang, L. Directional Water Collection on Wetted Spider Silk. *Nature* **2010**, *463*, 640−643.
(181) Hiltl, S.; Böker, A. Wetting Phenomena on (Gradient) Wrinkle Substrates. *Langmuir* **2016**, *32*, 8882−8888.
(182) Daniel, S.; Chaudhury, M. K.; Chen, J. C. Fast Drop Movements Resulting From the Phase Change on a Gradient Surface. *Science* **2001**, *291*, 633−636.
(183) Wong, T. S.; Kang, S. H.; Tang, S. K. Y.; Smythe, E. J.; Hatton, B. D.; Grinthal, A.; Aizenberg, J. Bioinspired Self-repairing Slippery Surfaces with Pressure-stable Omniphobicity. *Nature* **2011**, *477*, 443−447.
(184) Yang, X.; Zhuang, K.; Lu, Y.; Wang, X. Creation of Topological Ultraslippery Surfaces for Droplet Motion Control. *ACS Nano* **2021**, *15*, 2589−2599.
(185) Keiser, A.; Keiser, L.; Clanet, C.; Quéré, D. Drop Friction on Liquid-infused Materials. *Soft Matter* **2017**, *13*, 6981−6987.
(186) Sadullah, M. S.; Launay, G.; Parle, J.; Ledesma-Aguilar, R.; Gizaw, Y.; McHale, G.; Wells, G. G.; Kusumaatmaja, H. Bidirectional Motion of Droplets on Gradient Liquid Infused Surfaces. *Commun. Phys.* **2020**, *3*, 166.
(187) Liu, M.; Peng, Z.; Yao, Y.; Yang, Y.; Chen, S. Flexible Functional Surface for Efficient Water Collection. *ACS Appl. Mater. Interfaces* **2020**, *12*, 12256−12263.
(188) Laney, S. K.; Michalska, M.; Li, T.; Ramirez, F. V.; Portnoi, M.; Oh, J.; Thayne, I. G.; Parkin, I. P.; Tiwari, M. K.; Papakonstantinou, I. Delayed Lubricant Depletion of Slippery Liquid Infused Porous Surfaces using Precision Nanostructures. *Langmuir* **2021**, *37*, 10071−10078.
(189) Villegas, M.; Zhang, Y.; Abu Jarad, N.; Soleymani, L.; Didar, T. F. Liquid-infused Surfaces: A Review of Theory, Design, and Applications. *ACS Nano* **2019**, *13*, 8517−8536.
(190) Bueno, J.; Bazilevs, Y.; Juanes, R.; Gomez, H. Wettability Control of Droplet Durotaxis. *Soft Matter* **2018**, *14*, 1417−1426.
(191) Bueno, J.; Bazilevs, Y.; Juanes, R.; Gomez, H. Droplet Motion Driven by Tensotaxis. *Extreme Mech. Lett.* **2017**, *13*, 10−6.
(192) Style, R. W.; Che, Y.; Park, S. J.; Weon, B. M.; Je, J. H.; Hyland, C.; German, G. K.; Power, M. P.; Wilen, L. A.; Wettlaufer, J. S.; Dufresne, E. R. Patterning Droplets with Durotaxis. *Proc. Natl. Acad. Sci. U. S. A.* **2013**, *110*, 12541−12544.
(193) Bradley, A. T.; Box, F.; Hewitt, I. J.; Vella, D. Wettability-independent Droplet Transport by Bendotaxis. *Phys. Rev. Lett.* **2019**, *122*, 074503.
(194) Samy, R. A.; Suthanthiraraj, P. P. A.; George, D.; Iqbal, R.; Sen, A. K. Elastocapillarity-based Transport of Liquids in Flexible Confinements and over Soft Substrates. *Microfluid. Nanofluid.* **2019**, *23*, 100.
(195) Bodas, D.; Khan-Malek, C. Hydrophilization and Hydrophobic Recovery of PDMS by Oxygen Plasma and Chemical Treatment - An SEM Investigation. *Sens. Actuators, B* **2007**, *123*, 368−373.
(196) Wong, W. S. Y.; Hauer, L.; Naga, A.; Kaltbeitzel, A.; Baumli, P.; Berger, R.; D'Acunzi, M.; Vollmer, D.; Butt, H. J. Adaptive Wetting of Polydimethylsiloxane. *Langmuir* **2020**, *36*, 7236−7245.
(197) Shamshiri, M.; Jafari, R.; Momen, G. Potential Use of Smart Coatings for Icephobic Applications: A Review. *Surf. Coat. Technol.* **2021**, *424*, 127656.
(198) Ge, L.; Wang, S.; Song, X.; Ge, S.; Yu, J. 3D Origami-based Multifunction-integrated Immunodevice: Low-cost and Multiplexed Sandwich Chemiluminescence Immunoassay on Microfluidic Paper-based Analytical Device. *Lab Chip* **2012**, *12*, 3150.
(199) Gong, M. M.; Sinton, D. Turning the Page: Advancing Paper-based Microfluidics for Broad Diagnostic Application. *Chem. Rev.* **2017**, *117*, 8447−8480.
(200) de Oliveira, R. A.; Camargo, F.; Pesquero, N. C.; Faria, R. C. A Simple Method to Produce 2D and 3D Microfluidic Paper-based Analytical Devices for Clinical Analysis. *Anal. Chim. Acta* **2017**, *957*, 40−6.
(201) Mates, J. E.; Schutzius, T. M.; Qin, J.; Waldroup, D. E.; Megaridis, C. M. The Fluid Diode: Tunable Unidirectional Flow through Porous Substrates. *ACS Appl. Mater. Interfaces* **2014**, *6*, 12837−12843.
(202) Punjiya, M.; Moon, C. H.; Matharu, Z.; Nejad, H. R.; Sonkusale, S. A Three-dimensional Electrochemical Paper-based Analytical Device for Low-cost Diagnostics. *Analyst* **2018**, *143*, 1059−1064.
(203) Yeo, J. C.; Kenry, K.; Lim, C. T. Emergence of Microfluidic Wearable Technologies. *Lab Chip* **2016**, *16*, 4082−4090.
(204) Shay, T.; Saha, T.; Dickey, M. D.; Velev, O. D. Principles of Long-term Fluids Handling in Paper-based Wearables with Capillary-evaporative Transport. *Biomicrofluidics* **2020**, *14*, 034112.
(205) Zhao, F. J.; Bonmarin, M.; Chen, Z. C.; Larson, M.; Fay, D.; Runnoe, D.; Heikenfeld, J. Ultra-simple Wearable Local Sweat Volume Monitoring Patch Based on Swellable Hydrogels. *Lab Chip* **2020**, *20*, 168−174.
(206) Sun, Q.; Wang, D.; Li, Y.; Zhang, J.; Ye, S.; Cui, J.; Chen, L.; Wang, Z.; Butt, H. J.; Vollmer, D.; Deng, X. Surface Charge Printing for Programmed Droplet Transport. *Nat. Mater.* **2019**, *18*, 936−941.
(207) Li, N.; Yu, C.; Dong, Z.; Jiang, L. Finger Directed Surface Charges for Local Droplet Motion. *Soft Matter* **2020**, *16*, 9176−9182.
(208) Liu, C.; Legchenkova, I.; Han, L.; Ge, W.; Lv, C.; Feng, S.; Bormashenko, E.; Liu, Y. Directional Droplet Transport Mediated by Circular Groove Arrays. Part I: Experimental Findings. *Langmuir* **2020**, *36*, 9608−9615.
(209) Schutzius, T. M.; Graeber, G.; Elsharkawy, M.; Oreluk, J.; Megaridis, C. M. Morphing and Vectoring Impacting Droplets by Means of Wettability-engineered Surfaces. *Sci. Rep.* **2015**, *4*, 7029.
(210) Tang, X.; Li, W.; Wang, L. Furcated Droplet Motility on Crystalline Surfaces. *Nat. Nanotechnol.* **2021**, *16*, 1106−1112.
(211) Stamatopoulos, C.; Milionis, A.; Ackerl, N.; Donati, M.; Leudet de la Vallée, P.; Rudolf von Rohr, P.; Poulikakos, D. Droplet Self-propulsion on Superhydrophobic Microtracks. *ACS Nano* **2020**, *14*, 12895−904.
(212) Chen, H.; Cogswell, J.; Anagnostopoulos, C.; Faghri, M. A Fluidic Diode, Valves, and a Sequential-loading Circuit Fabricated on Layered Paper. *Lab Chip* **2012**, *12*, 2909−2913.


https://doi.org/10.1021/acs.chemrev.2c00045
*Chem. Rev.* 2022, 122, 16752−16801

(213) Li, X.; Tian, J.; Shen, W. Progress in Patterned Paper Sizing for Fabrication of Paper-based Microfluidic Sensors. *Cellulose* **2010**, *17*, 649−659.
(214) Toley, B. J.; McKenzie, B.; Liang, T.; Buser, J. R.; Yager, P.; Fu, E. Tunable-delay Shunts for Paper Microfluidic Devices. *Anal. Chem.* **2013**, *85*, 11545−11552.
(215) Feng, S.; Zhu, P.; Zheng, H.; Zhan, H.; Chen, C.; Li, J.; Wang, L.; Yao, X.; Liu, Y.; Wang, Z. Three-dimensional capillary ratchet-induced liquid directional steering. *Science.* **2021**, *373*, 1344−1348.
(216) Wu, J.; Wang, N.; Wang, L.; Dong, H.; Zhao, Y.; Jiang, L. Unidirectional Water-penetration Composite Fibrous Film via Electrospinning. *Soft Matter* **2012**, *8*, 5996−5999.
(217) Widodo, M.; Handayani, A. F.; Sumaryadi, G. Tailoring Cotton Fabric with Wettability Gradient and Anisotropic Penetration of Liquid by Spray Coating. *J. Text. Inst.* **2020**, *111*, 972−984.
(218) Shou, D.; Fan, J. An All Hydrophilic Fluid Diode for Unidirectional Flow in Porous Systems. *Adv. Funct. Mater.* **2018**, *28*, 1800269.
(219) Lee, C. Y.; Chang, C. L.; Wang, Y. N.; Fu, L. M. Microfluidic Mixing: A Review. *Int. J. Mol. Sci.* **2011**, *12*, 3263−3287.
(220) Delaney, J. L.; Hogan, C. F.; Tian, J.; Shen, W. Electrogenerated Chemiluminescence Detection in Paper-based Microfluidic Sensors. *Anal. Chem.* **2011**, *83*, 1300−1306.
(221) Morrissette, J. M.; Mahapatra, P. S.; Ghosh, A.; Ganguly, R.; Megaridis, C. M. Rapid, Self-driven Liquid Mixing on Open-surface Microfluidic Platforms. *Sci. Rep.* **2017**, *7*, 1800.
(222) Bhagat, A. A. S.; Papautsky, I. Enhancing Particle Dispersion in a Passive Planar Micromixer using Rectangular Obstacles. *J. Micromech. Microeng.* **2008**, *18*, 085005.
(223) Stroock, A. D.; Dertinger, S. K.; Ajdari, A.; Mezíc, I.; Stone, H. A.; Whitesides, G. M. Chaotic Mixer for Microchannels. *Science* **2002**, *295*, 647−651.
(224) Xing, S.; Jiang, J.; Pan, T. Interfacial Microfluidic Transport on Micropatterned Superhydrophobic Textile. *Lab Chip* **2013**, *13*, 1937−1947.
(225) Ody, T.; Panth, M.; Sommers, A. D.; Eid, K. F. Controlling the Motion of Ferrofluid Droplets using Surface Tension Gradients and Magnetoviscous Pinning. *Langmuir* **2016**, *32*, 6967−6976.
(226) Sellier, M.; Nock, V.; Gaubert, C.; Verdier, C. Droplet Actuation Induced by Coalescence: Experimental Evidences and Phenomenological Modelling. *Eur. Phys. J. Spec. Top.* **2013**, *219*, 131−141.
(227) Kim, J. Spray Cooling Heat Transfer: The State of the Art. *Int. J. Heat Fluid Flow* **2007**, *28*, 753−767.
(228) Okubo, Y.; Ikemoto, K.; Koike, K.; Tsutsui, C.; Sakata, I.; Takei, O.; Adachi, A.; Sakai, T. DNA Introduction into Living Cells by Water Droplet Impact with an Electrospray Process. *Angew. Chem., Int. Ed.* **2008**, *47*, 1429−1431.
(229) Koukoravas, T. P.; Ghosh, A.; Mahapatra, P. S.; Ganguly, R.; Megaridis, C. M. Spatially-selective Cooling by Liquid Jet Impinging Orthogonally on a Wettability-patterned Surface. *Int. J. Heat Mass Transfer* **2016**, *95*, 142−52.
(230) Josserand, C.; Thoroddsen, S. T. Drop Impact on a Solid Surface. *Annu. Rev. Fluid Mech.* **2016**, *48*, 365−391.
(231) Liang, G.; Mudawar, I. Review of Drop Impact on Heated Walls. *Int. J. Heat Mass Transfer* **2017**, *106*, 103−126.
(232) Bayer, I. S.; Megaridis, C. M. Contact Angle Dynamics in Droplets Impacting on Flat Surfaces with Different Wetting Characteristics. *J. Fluid Mech.* **2006**, *558*, 415−449.
(233) Qi, W.; Weisensee, P. B. Dynamic Wetting and Heat Transfer during Droplet Impact on Bi-phobic Wettability-patterned Surfaces. *Phys. Fluids* **2020**, *32*, 067110.
(234) Quéré, D. Leidenfrost Dynamics. *Annu. Rev. Fluid Mech.* **2013**, *45*, 197−215.
(235) Sen, U.; Roy, T.; Ganguly, R.; Angeloni, L. A.; Schroeder, W. A.; Megaridis, C. M. Explosive Behavior during Binary-droplet Impact on Superheated Substrates. *Int. J. Heat Mass Transfer* **2020**, *154*, 119658.
(236) Wang, G.; McDonough, J. R.; Zivkovic, V.; Long, T.; Wang, S. From Thermal Energy to Kinetic Energy: Droplet Motion Triggered by the Leidenfrost Effect. *Adv. Mater. Interfaces* **2021**, *8*, 2001249.
(237) Tyagi, P. K.; Kumar, R.; Mondal, P. K. A Review of the State-of-the-art Nanofluid Spray and Jet Impingement Cooling. *Phys. Fluids* **2020**, *32*, 121301.
(238) Butterfield, D. J.; Iverson, B. D.; Maynes, D.; Crockett, J. Transient Heat Transfer of Impinging Jets on Superheated Wetting and Non-wetting Surfaces. *Int. J. Heat Mass Transfer* **2021**, *175*, 121056.
(239) Nikapitiya, N. Y. J. B.; Nahar, M. M.; Moon, H. Accurate, Consistent, and Fast Droplet Splitting and Dispensing in Electrowetting on Dielectric Digital Microfluidics. *Micro Nano Syst. Lett.* **2017**, *5*, 24.
(240) Ding, R.; Krikstolaityte, V.; Lisak, G. Inorganic Salt Modified Paper Substrates Utilized in Paper Based Microfluidic Sampling for Potentiometric Determination of Heavy Metals. *Sens. Actuators, B* **2019**, *290*, 347−356.
(241) Tai, H.; Duan, Z.; Wang, Y.; Wang, S.; Jiang, Y. Paper-based Sensors for Gas, Humidity, and Strain Detections: A Review. *ACS Appl. Mater. Interfaces* **2020**, *12*, 31037−31053.
(242) Xu, T.; Xu, L. P.; Zhang, X.; Wang, S. Bioinspired Superwettable Micropatterns for Biosensing. *Chem. Soc. Rev.* **2019**, *48*, 3153−3165.
(243) Bandodkar, A. J.; Jeang, W. J.; Ghaffari, R.; Rogers, J. A. Wearable Sensors for Biochemical Sweat Analysis. *Annu. Rev. Anal. Chem.* **2019**, *12*, 1−22.
(244) Ghaffari, R.; Rogers, J. A.; Ray, T. R. Recent Progress, Challenges, and Opportunities for Wearable Biochemical Sensors for Sweat Analysis. *Sens. Actuators, B* **2021**, *332*, 129447.
(245) Wu, T.; Xu, T.; Chen, Y.; Yang, Y.; Xu, L. P.; Zhang, X.; Wang, S. Renewable Superwettable Biochip for miRNA Detection. *Sens. Actuators, B* **2018**, *258*, 715−721.
(246) Chi, J.; Ma, B.; Dong, X.; Gao, B.; Elbaz, A.; Liu, H.; Gu, Z. A Bio-inspired Photonic Nitrocellulose Array for Ultrasensitive Assays of Single Nucleic Acids. *Analyst* **2018**, *143*, 4559−65.
(247) Xu, L. P.; Chen, Y.; Yang, G.; Shi, W.; Dai, B.; Li, G.; Cao, Y.; Wen, Y.; Zhang, X.; Wang, S. Ultratrace DNA Detection Based on the Condensing-enrichment Effect of Superwettable Microchips. *Adv. Mater.* **2015**, *27*, 6878−6884.
(248) Li, H.; Yang, Q.; Hou, J.; Li, Y.; Li, M.; Song, Y. Bioinspired Micropatterned Superhydrophilic Au-areoles for Surface-enhanced Raman scattering (SERS) Trace Detection. *Adv. Funct. Mater.* **2018**, *28*, 1800448.
(249) Choi, J.; Ghaffari, R.; Baker, L. B.; Rogers, J. A. Skin-interfaced Systems for Sweat Collection and Analytics. *Sci. Adv.* **2018**, *4*, eaar3921.
(250) Son, J.; Bae, G. Y.; Lee, S.; Lee, G.; Kim, S. W.; Kim, D.; Chung, S.; Cho, K. Cactus-spine-inspired Sweat-collecting Patch for Fast and Continuous Monitoring of Sweat. *Adv. Mater.* **2021**, *33*, 2102740.
(251) He, X.; Xu, T.; Gu, Z.; Gao, W.; Xu, L. P.; Pan, T.; Zhang, X. Flexible and Superwettable Bands as a Platform toward Sweat Sampling and Sensing. *Anal. Chem.* **2019**, *91*, 4296−4300.
(252) Koh, A.; Kang, D.; Xue, Y.; Lee, S.; Pielak, R. M.; Kim, J.; Hwang, T.; Min, S.; Banks, A.; Bastien, P.; et al. A Soft, Wearable Microfluidic Device for the Capture, Storage, and Colorimetric Sensing of Sweat. *Sci. Transl. Med.* **2016**, *8*, 366ra165.
(253) Curto, V. F.; Coyle, S.; Byrne, R.; Angelov, N.; Diamond, D.; Benito-Lopez, F. Concept and Development of an Autonomous Wearable Micro-fluidic Platform for Real Time pH Sweat Analysis. *Sens. Actuators, B* **2012**, *175*, 263−270.
(254) Chi, J.; Zhang, X.; Wang, Y.; Shao, C.; Shang, L.; Zhao, Y. Bio-inspired Wettability Patterns for Biomedical Applications. *Mater. Horiz.* **2021**, *8*, 124−44.
(255) Michael, I. J.; Kumar, S.; Oh, J. M.; Kim, D.; Kim, J.; Cho, Y. K. Surface-engineered Paper Hanging Drop Chip for 3D Spheroid Culture and Analysis. *ACS Appl. Mater. Interfaces* **2018**, *10*, 33839−33846.
(256) Shao, C.; Liu, Y.; Chi, J.; Chen, Z.; Wang, J.; Zhao, Y. Droplet Microarray on Patterned Butterfly Wing Surfaces for Cell Spheroid Culture. *Langmuir* **2019**, *35*, 3832−3839.
(257) Neto, A. I.; Correia, C. R.; Oliveira, M. B.; Rial-Hermida, M. I.; Alvarez-Lorenzo, C.; Reis, R. L.; Mano, J. F. A Novel Hanging Spherical

Drop System for the Generation of Cellular Spheroids and High Throughput Combinatorial Drug Screening. *Biomater. Sci.* **2015**, *3*, 581−585.
(258) Gupta, P.; Kar, S.; Kumar, A.; Tseng, F. G.; Pradhan, S.; Mahapatra, P. S.; Santra, T. S. Pulsed Laser Assisted High-throughput Intracellular Delivery in Hanging Drop Based Three Dimensional Cancer Spheroids. *Analyst* **2021**, *146*, 4756−4766.
(259) Lei, W.; Bruchmann, J.; Rüping, J. L.; Levkin, P. A.; Schwartz, T. Biofilm Bridges Forming Structural Networks on Patterned Lubricant-infused Surfaces. *Adv. Sci.* **2019**, *6*, 1900519.
(260) Yager, P.; Edwards, T.; Fu, E.; Helton, K.; Nelson, K.; Tam, M. R.; Weigl, B. H. Microfluidic Diagnostic Technologies for Global Public Health. *Nature* **2006**, *442*, 412−418.
(261) Novak, M. T.; Kotanen, C. N.; Carrara, S.; Guiseppi-Elie, A.; Moussy, F. G. Diagnostic Tools and Technologies for Infectious and Non-communicable Diseases in Low-and-middle-income Countries. *Health Technol.* **2013**, *3*, 271−281.
(262) Lu, Y.; Shi, W.; Jiang, L.; Qin, J.; Lin, B. Rapid Prototyping of Paper- based Microfluidics with Wax for Low-cost, Portable Bioassay. *Electrophoresis* **2009**, *30*, 1497−1500.
(263) Gervais, L.; de Rooij, N.; Delamarche, E. Microfluidic Chips for Point-of-care Immunodiagnostics. *Adv. Mater.* **2011**, *23*, H151−76.
(264) Rozand, C. Paper-based Analytical Devices for Point-of-care Infectious Disease Testing. *Eur. J. Clin. Microbiol. Infect. Dis.* **2014**, *33*, 147−156.
(265) Tang, R.; Yang, H.; Gong, Y.; You, M.; Liu, Z.; Choi, J. R.; Wen, T.; Qu, Z.; Mei, Q.; Xu, F. A Fully Disposable and Integrated Paper-based Device for Nucleic Acid Extraction. *Amplification and Detection, Lab Chip* **2017**, *17*, 1270−1279.
(266) Nilghaz, A.; Bagherbaigi, S.; Lam, C. L.; Mousavi, S. M.; Corcoles, E. P.; Wicaksono, D. H. Multiple Semi-quantitative Colorimetric Assays in Compact Embeddable Microfluidic Cloth-based Analytical Device ($\mu$CAD) for Effective Point-of-care Diagnostic. *Microfluid. Nanofluid.* **2015**, *19*, 317−333.
(267) Bhandari, P.; Narahari, T.; Dendukuri, D. Fab-chips: A Versatile, Fabric Based Platform for Low-cost, Rapid and Multiplexed Diagnostics. *Lab Chip* **2011**, *11*, 2493−2499.
(268) Fu, E.; Liang, T.; Houghtaling, J.; Ramachandran, S.; Ramsey, S. A.; Lutz, B.; Yager, P. Enhanced Sensitivity of Lateral Flow Tests using a Two-dimensional Paper Network Format. *Anal. Chem.* **2011**, *83*, 7941−6.
(269) Fu, E.; Lutz, B.; Kauffman, P.; Yager, P. Controlled Reagent Transport in Disposable 2D Paper Networks. *Lab Chip* **2010**, *10*, 918−920.
(270) Hossain, S. Z.; Brennan, J. D. $\beta$-Galactosidase-based Colorimetric Paper Sensor for Determination of Heavy Metals. *Anal. Chem.* **2011**, *83*, 8772−8778.
(271) Songjaroen, T.; Dungchai, W.; Chailapakul, O.; Henry, C. S.; Laiwattanapaisal, W. Blood Separation on Microfluidic Paper-based Analytical Devices. *Lab Chip* **2012**, *12*, 3392−3398.
(272) Bhakta, S. A.; Borba, R.; Taba, M.; Garcia, C. D.; Carrilho, E. Determination of Nitrite in Saliva using Microfluidic Paper-based Analytical Devices. *Anal. Chim. Acta* **2014**, *809*, 117−122.
(273) Walker, R. Nitrates, nitrites and N-nitrosocompounds: A Review of the Occurrence in Food and Diet and the Toxicological Implications. *Food Addit. Contam.* **1990**, *7*, 717−768.
(274) Kownacka, A. E.; Vegelyte, D.; Joosse, M.; Anton, N.; Toebes, B. J.; Lauko, J.; Buzzacchera, I.; Lipinska, K.; Wilson, D. A.; Geelhoed-Duijvestijn, N.; Wilson, C. J. Clinical Evidence for Use of a Noninvasive Biosensor for Tear Glucose as an Alternative to Painful Finger-prick for Diabetes Management Utilizing a Biopolymer Coating. *Biomacromolecules* **2018**, *19*, 4504−4511.
(275) Silva, T. G.; de Araujo, W. R.; Munoz, R. A.; Richter, E. M.; Santana, M. H.; Coltro, W. K.; Paixão, T. R. Simple and Sensitive Paper-based Device Coupling Electrochemical Sample Pretreatment and Colorimetric Detection. *Anal. Chem.* **2016**, *88*, 5145−5151.
(276) Narayanan, K.; Makino, S. Cooperation of an RNA Packaging Signal and a Viral Envelope Protein in Coronavirus RNA Packaging. *J. Virol.* **2001**, *75*, 9059−9067.
(277) Bhalla, N.; Pan, Y.; Yang, Z.; Payam, A. F. Opportunities and Challenges for Biosensors and Nanoscale Analytical Tools for Pandemics: COVID-19. *ACS Nano* **2020**, *14*, 7783−807.
(278) Mahapatra, P. S.; Chatterjee, S.; Tiwari, M. K.; Ganguly, R.; Megaridis, C. M. Surface Treatments to Enhance the Functionality of PPEs. *Trans. Indian Natl. Acad. Eng.* **2020**, *5*, 333−336.
(279) Sarkar, S.; Mukhopadhyay, A.; Sen, S.; Mondal, S.; Banerjee, A.; Mandal, P.; Ghosh, R.; Megaridis, C. M.; Ganguly, R. Leveraging Wettability Engineering to Develop Three-layer DIY Face Masks from Low-cost Materials. *Trans. Indian Natl. Acad. Eng.* **2020**, *5*, 393−398.
(280) Augustine, R.; Hasan, A.; Das, S.; Ahmed, R.; Mori, Y.; Notomi, T.; Kevadiya, B. D.; Thakor, A. S. Loop-mediated Isothermal Amplification (LAMP): A Rapid, Sensitive, Specific, and Cost-effective Point-of-care Test for Corona Viruses in the Context of COVID-19 Pandemic. *Biology* **2020**, *9*, 182.
(281) Shen, K. M.; Sabbavarapu, N. M.; Fu, C. Y.; Jan, J. T.; Wang, J. R.; Hung, S. C.; Lee, G. B. An Integrated Microfluidic System for Rapid Detection and Multiple Subtyping of Influenza A Viruses by using Glycan-coated Magnetic Beads and RT-PCR. *Lab Chip* **2019**, *19*, 1277−1286.
(282) Song, Q.; Sun, X.; Dai, Z.; Gao, Y.; Gong, X.; Zhou, B.; Wu, J.; Wen, W. Point-of-care Testing Detection Methods for COVID-19. *Lab Chip* **2021**, *21*, 1634−1660.
(283) Lin, Q.; Wen, D.; Wu, J.; Liu, L.; Wu, W.; Fang, X.; Kong, J. Microfluidic Immunoassays for Sensitive and Simultaneous Detection of IgG/IgM/Antigen of SARS-CoV-2 within 15 min. *Anal. Chem.* **2020**, *92*, 9454−9458.
(284) Chen, L.; Zhang, G.; Liu, L.; Li, Z. Emerging Biosensing Technologies for Improved Diagnostics of COVID-19 and Future Pandemics. *Talanta* **2021**, *225*, 121986.
(285) Seo, G.; Lee, G.; Kim, M. J.; Baek, S. H.; Choi, M.; Ku, K. B.; Lee, C. S.; Jun, S.; Park, D.; Kim, H. G.; Kim, S. J.; et al. Rapid Detection of COVID-19 Causative Virus (SARS-CoV-2) in Human Nasopharyngeal Swab Specimens using Field-effect Transistor-based Biosensor. *ACS Nano* **2020**, *14*, 5135−5142.
(286) Nguyen, P. Q.; Soenksen, L. R.; Donghia, N. M.; Angenent-Mari, N. M.; de Puig, H.; Huang, A.; Lee, R.; Slomovic, S.; Galbersanini, T.; Lansberry, G.; Sallum, H. M.; et al. Wearable Materials with Embedded Synthetic Biology Sensors for Biomolecule Detection. *Nat. Biotechnol.* **2021**, *39*, 1366−1374.
(287) Wang, Y.; Wang, Z.; Gupta, P.; Morrissey, J. J.; Naik, R. R.; Singamaneni, S. Enhancing the Stability of COVID-19 Serological Assay through Metal-organic Framework Encapsulation. *Adv. Healthcare Mater.* **2021**, *10*, 2100410.
(288) *Cepheid, GeneXpert Systems*; Cepheid, 2022; https://www.cepheid.com/en/systems/GeneXpert-Family-of-Systems/GeneXpert-System (accessed 2022-05-23).
(289) Soundiram, I.*GeneXpert Technology*; Cepheid, 2012; https://docplayer.net/amp/20801051-Genexpert-technology-indira-soundiram-2012.html (accessed 2022-05-23).
(290) Vivalytic VRI Test*The Innovative Solution for Rapid Diagnosis of Viral Respiratory Diseases*; Bosch Healthcare Solutions, 2022; https://www.bosch-vivalytic.com/en/product/vivalytic-tests/vri-multiplex-test (accessed 2022-05-23).
(291) Koukoravas, T. P.; Mahapatra, P. S.; Ganguly, R.; Megaridis, C. M. Wettability-confined Liquid-film Convective Cooling: Parameter Study. *Int. J. Heat Mass Transfer* **2018**, *126*, 667−676.
(292) Damoulakis, G.; Gukeh, M. J.; Koukoravas, T. P.; Megaridis, C. M. High-performance Planar Thermal Diode with Wickless Components. *J. Electron. Packag.* **2022**, *144*, 031004.
(293) Kirillova, A.; Ionov, L.; Roisman, I. V.; Synytska, A. Hybrid Hairy Janus Particles for Anti-icing and De-icing Surfaces: Synergism of Properties and Effects. *Chem. Mater.* **2016**, *28*, 6995−7005.
(294) Kwak, S. S.; Lin, S.; Lee, J. H.; Ryu, H.; Kim, T. Y.; Zhong, H.; Chen, H.; Kim, S. W. Triboelectrification-induced Large Electric Power Generation from a Single Moving Droplet on Graphene/Polytetrafluoroethylene. *ACS Nano* **2016**, *10*, 7297−302.


https://doi.org/10.1021/acs.chemrev.2c00045
*Chem. Rev.* 2022, 122, 16752−16801

(295) Joshi, S. N.; Dede, E. M.Two-Phase Heat Transfer Assemblies and Power Electronics Incorporating the Same. U.S. Patent 8,842,435, September 23, 2014).
(296) Thomas, T. M.; Chowdhury, I. U.; Dhivyaraja, K.; Mahapatra, P. S.; Pattamatta, A.; Tiwari, M. K. Droplet Dynamics on a Wettability Patterned Surface during Spray Impact. *Processes* **2021**, *9*, 555.
(297) Berejnov, V.; Djilali, N.; Sinton, D. Lab-on-chip Methodologies for the Study of Transport in Porous Media: Energy Applications. *Lab Chip* **2008**, *8*, 689−693.
(298) Yamada, Y.; Ikuta, T.; Nishiyama, T.; Takahashi, K.; Takata, Y. Droplet Nucleation on a Well-defined Hydrophilic-hydrophobic Surface of 10 nm Order Resolution. *Langmuir* **2014**, *30*, 14532−14537.
(299) Mahapatra, P. S.; Ghosh, A.; Ganguly, R.; Megaridis, C. M. Key Design and Operating Parameters for Enhancing Dropwise Condensation Through Wettability Patterning. *Int. J. Heat Mass Transfer* **2016**, *92*, 877−883.
(300) Wang, X.; Zeng, J.; Li, J.; Yu, X.; Wang, Z.; Zhang, Y. Beetle and Cactus-inspired Surface Endows Continuous and Directional Droplet Jumping for Efficient Water Harvesting. *J. Mater. Chem. A* **2021**, *9*, 1507−1516.
(301) Zhang, Y.; Meng, N.; Babar, A. A.; Wang, X.; Yu, J.; Ding, B. Lizard-skin-inspired Nanofibrous Capillary Network Combined with a Slippery Surface for Efficient Fog Collection. *ACS Appl. Mater. Interfaces* **2021**, *13*, 36587−36594.
(302) Li, J.; Ran, R.; Wang, H.; Wang, Y.; Chen, Y.; Niu, S.; Arratia, P. E.; Yang, S. Aerodynamics-assisted, Efficient and Scalable Kirigami Fog Collectors. *Nat. Commun.* **2021**, *12*, 5484.
(303) Jain, S.; Nehra, M.; Kumar, R.; Dilbaghi, N.; Hu, T.; Kumar, S.; Kaushik, A.; Li, C. Z. Internet of Medical Things (IoMT)-Integrated Biosensors for Point-of-care Testing of Infectious Diseases. *Biosens. Bioelectron.* **2021**, *179*, 113074.
(304) Chatterjee, R.; Beysens, D.; Anand, S. Delaying Ice and Frost Formation using Phase-switching Liquids. *Adv. Mater.* **2019**, *31*, 1807812.
(305) Sen, U.; Chatterjee, S.; Sinha Mahapatra, P.; Ganguly, R.; Dodge, R.; Yu, L.; Megaridis, C. M. Surface-wettability Patterning for Distributing High-Momentum Water Jets on Porous Polymeric Substrates. *ACS Appl. Mater. Interfaces* **2018**, *10*, 5038−5049.
(306) McCarthy, J.; Minsky, M. L.; Rochester, N.; Shannon, C. E. A Proposal for the Dartmouth Summer Research Project on Artificial Intelligence, August 31, 1955. *AI Magazine* **2006**, *27*, 12.
(307) Attia, P. M.; Grover, A.; Jin, N.; Severson, K. A.; Markov, T. M.; Liao, Y. H.; Chen, M. H.; Cheong, B.; Perkins, N.; Yang, Z.; Herring, P. K.; et al. Closed-loop Optimization of Fast-charging Protocols for Batteries with Machine Learning. *Nature* **2020**, *578*, 397−402.
(308) Uddin, M.; Wang, Y.; Woodbury-Smith, M. Artificial Intelligence for Precision Medicine in Neurodevelopmental Disorders. *npj Digital Med.* **2019**, *2*, 112.
(309) de Almeida, A. F.; Moreira, R.; Rodrigues, T. Synthetic Organic Chemistry Driven by Artificial Intelligence. *Nat. Rev. Chem.* **2019**, *3*, 589−604.
(310) McKinney, S. M.; Sieniek, M.; Godbole, V.; Godwin, J.; Antropova, N.; Ashrafian, H.; Back, T.; Chesus, M.; Corrado, G. S.; Darzi, A.; Etemadi, M.; et al. International Evaluation of an AI System for Breast Cancer Screening. *Nature* **2020**, *577*, 89−94.
(311) Mennel, L.; Symonowicz, J.; Wachter, S.; Polyushkin, D. K.; Molina-Mendoza, A. J.; Mueller, T. Ultrafast Machine Vision with 2D Material Neural Network Image Sensors. *Nature* **2020**, *579*, 62−6.
(312) Schmidt, J.; Marques, M. R.; Botti, S.; Marques, M. A. Recent Advances and Applications of Machine Learning in Solid-state Materials Science. *npj Comput. Mater.* **2019**, *5*, 83.
(313) Evans, J. D.; Coudert, F. X. Predicting the Mechanical Properties of Zeolite Frameworks by Machine Learning. *Chem. Mater.* **2017**, *29*, 7833−7839.
(314) Altay, O.; Gurgenc, T.; Ulas, M.; Özel, C. Prediction of Wear Loss Quantities of Ferro-alloy Coating using Different Machine Learning Algorithms. *Friction* **2020**, *8*, 107−14.
(315) Arisoy, Y. M.; Özel, T. Machine Learning Based Predictive Modeling of Machining Induced Microhardness and Grain Size in Ti-6Al-4V Alloy. *Mater. Manuf. Processes* **2015**, *30*, 425−433.
(316) Gukeh, M. J.; Moitra, S.; Ibrahim, A. N.; Derrible, S.; Megaridis, C. M. Machine Learning Prediction of $TiO_2$-coating Wettability Tuned via UV Exposure. *ACS Appl. Mater. Interfaces* **2021**, *13*, 46171.
(317) Isozaki, A.; Harmon, J.; Zhou, Y.; Li, S.; Nakagawa, Y.; Hayashi, M.; Mikami, H.; Lei, C.; Goda, K. AI on a Chip. *Lab Chip* **2020**, *20*, 3074−3090.
(318) Jordan, N. V.; Bardia, A.; Wittner, B. S.; Benes, C.; Ligorio, M.; Zheng, Y.; Yu, M.; Sundaresan, T. K.; Licausi, J. A.; Desai, R.; et al. HER2 Expression Identifies Dynamic Functional States within Circulating Breast Cancer Cells. *Nature* **2016**, *537*, 102−106.
(319) Nitta, N.; Sugimura, T.; Isozaki, A.; Mikami, H.; Hiraki, K.; Sakuma, S.; Iino, T.; Arai, F.; Endo, T.; Fujiwaki, Y.; Fukuzawa, H.; et al. Intelligent Image-activated Cell Sorting. *Cell* **2018**, *175*, 266−276.
(320) Kobayashi, H.; Lei, C.; Wu, Y.; Mao, A.; Jiang, Y.; Guo, B.; Ozeki, Y.; Goda, K. Label-free Detection of Cellular Drug Responses by High-throughput Bright-field Imaging and Machine Learning. *Sci. Rep.* **2017**, *7*, 12454.
(321) San-Miguel, A.; Kurshan, P. T.; Crane, M. M.; Zhao, Y.; McGrath, P. T.; Shen, K.; Lu, H. Deep Phenotyping Unveils Hidden Traits and Genetic Relations in Subtle Mutants. *Nat. Commun.* **2016**, *7*, 12990.
(322) Faust, K.; Xie, Q.; Han, D.; Goyle, K.; Volynskaya, Z.; Djuric, U.; Diamandis, P. Visualizing Histopathologic Deep Learning Classification and Anomaly Detection using Nonlinear Feature Space Dimensionality Reduction. *BMC Bioinf.* **2018**, *19*, 173.
(323) Appelboom, G.; Camacho, E.; Abraham, M. E.; Bruce, S. S.; Dumont, E. L.; Zacharia, B. E.; D'Amico, R.; Slomian, J.; Reginster, J. Y.; Bruyère, O.; Connolly, E. S. Smart wearable body sensors for patient self-assessment and monitoring. *Arch. Public Health* **2014**, *72*, 28.
(324) Kalasin, S.; Sangnuang, P.; Surareungchai, W. Intelligent Wearable Sensors Interconnected with Advanced Wound Dressing Bandages for Contactless Chronic Skin Monitoring: Artificial Intelligence for Predicting Tissue Regeneration. *Anal. Chem.* **2022**, *94*, 6842−6852.
(325) Wen, F.; Sun, Z.; He, T.; Shi, Q.; Zhu, M.; Zhang, Z.; Li, L.; Zhang, T.; Lee, C. Machine learning glove using self-powered conductive superhydrophobic triboelectric textile for gesture recognition in VR/AR applications. *Adv. Sci.* **2020**, *7*, 2000261.
(326) Li, L.; Bai, Y.; Li, L.; Wang, S.; Zhang, T. A superhydrophobic smart coating for flexible and wearable sensing electronics. *Adv. Mater.* **2017**, *29*, 1702517.
(327) Ma, L.; Wang, J.; He, J.; Yao, Y.; Zhu, X.; Peng, L.; Yang, J.; Liu, X.; Qu, M. Biotemplated Fabrication of a Multifunctional Superwettable Shape Memory Film for Wearable Sensing Electronics and Smart Liquid Droplet Manipulation. *ACS Appl. Mater. Interfaces* **2021**, *13*, 31285−31297.
(328) Cann, O.*Fourth Industrial Revolution; These Are the Top 10 Emerging Technologies of 2016*; World Economic Forum, 2016; https://www.weforum.org/agenda/2016/06/top-10-emerging-technologies-2016/, accessed 2022-05-23).
(329) Wu, Q.; Liu, J.; Wang, X.; Feng, L.; Wu, J.; Zhu, X.; Wen, W.; Gong, X. Organ-on-a-chip: Recent breakthroughs and future prospects. *Biomed. Eng. Online* **2020**, *19*, 9.
(330) Zhang, B.; Korolj, A.; Lai, B. F.; Radisic, M. Advances in organ-on-a-chip engineering. *Nat. Rev. Mater.* **2018**, *3*, 257−278.
(331) Li, Q.; Niu, K.; Wang, D.; Xuan, L.; Wang, X. Low-cost rapid prototyping and assembly of an open microfluidic device for a 3D vascularized organ-on-a-chip. *Lab Chip* **2022**, *22*, 2682−2694.


https://doi.org/10.1021/acs.chemrev.2c00045
*Chem. Rev.* 2022, 122, 16752−16801